UNIVERSIDAD DEL PAÍS VASCO / EUSKAL HERRIKO UNIBERTSITATEA

DOCTORAL THESIS

High-temperature infrared emissivity of materials for alternative energy applications

Author:
Iñigo GONZÁLEZ DE ARRIETA MARTÍNEZ

Supervisors:
Dr. Gabriel A. LÓPEZ
Dr. Raquel FUENTE

A thesis submitted in partial fulfillment of the requirements for the degree of Doctor of Philosophy in Physics in the University of the Basque Country (UPV/EHU)

May 2020

Abstract

The emissivity is a thermophysical property that relates the amount of thermal radiation emitted by a material to that radiated by a blackbody. It is a crucial property for both industrial and scientific applications, since it determines the overall heat transfer in high-temperature or high-vacuum conditions. This thesis is divided into two main sections: on the one hand, the development and improvement of emissivity measurement methods at the University of the Basque Country (UPV/EHU) and, on the other, the application of these methods to the characterization of materials of industrial interest in the alternative energy sector (solar thermal energy and nuclear fusion power). Firstly, an in-depth review of the unique HAIRL emissometer has been carried out, including both instrumental and methodological improvements, as well as a renewed analysis of its sources of error. Secondly, three types of materials have been studied: multi-layer selective solar absorbers for parabolic trough power plants, non-selective black coatings for solar tower plants, and a family of vanadium alloys for future nuclear fusion reactors. The overall objective of this work is to improve the knowledge about the radiation heat transfer properties of key materials for alternative energy processes.

Acknowledgements

Tal como imaginaba, esta sección es, sin duda, la más difícil de escribir de toda la tesis. Supone un tremendo esfuerzo sentarse a dedicar siquiera unas breves palabras a personas que han hecho tanto por mí y por este trabajo. Espero estar a la altura y no dejarme a nadie; si lo hago, por favor, no me lo tengáis demasiado en cuenta.

En primer lugar, quiero agradecer a mis directores, Gabriel y Raquel, todo el esfuerzo que han dedicado estos años para garantizar que esta tesis y este grupo salieran adelante. Tomaron la responsabilidad de reflotar un barco medio hundido y han dedicado un tiempo muy preciado a construir algo interesante en esta universidad. Me han apoyado siempre que lo he necesitado, soportando incluso mi poco sentido de la oportunidad gracias a esa política tan agradecida de puertas abiertas y disponibilidad total.

Alguien que se merece una mención aparte es Telmo. Su actitud proactiva y *no-bullshit* ante la vida me ha servido para aprender mucho, y a menudo su ayuda ha sido la clave para resolver los problemas que me he ido encontrando. También agradezco mucho sus consejos sobre todo tipo de cuestiones, tanto las científicas como las de otro tipo.

No me puedo olvidar del resto de miembros del Grupo de Propiedades Radiativas de Materiales, con los cuales he compartido (demasiadas) reuniones, mails a deshora y *txuletas* en el Pinu Barri: Josu (¡perdón por la chapa!), Irene y Joxemi. No me olvido de Noelia, quien también ha sido mi compi de prácticas. Gracias por tus ánimos, tus consejos y esa mala hostia tan bien puesta.

Al margen de mi grupo, también hay otras personas de la facultad a quienes agradecer mucho. Agradezco a Tomasz su predisposición a ayudarme durante los primeros años. También a Iñaki Orue por las molestias y su mano con las chapuzas. Por último, un sincero agradecimiento a Iñigo Egusquiza por sus consejos cuando todavía no era más que un pipiolo que se quería presentar a la escuela de verano del CERN con más ganas que juicio.

Por otro lado, debo agradecer al Gobierno Vasco su apoyo financiero mediante dos ayudas predoctorales (PRE_2018_1_0045 y PRE_2019_2_0191), así como el esfuerzo realizado por mi grupo para poder financiarme hasta que conseguí dichas becas.

I thank Christian Monte, Jörg Hollandt, and Elisabeth Eigel for welcoming me into PTB and providing funding and help throughout my stay. Those months were definitely the high point of the entire Ph.D., and I only regret doing it so late that I could not refocus part of this thesis along those lines. Living in Berlin has been a wonderful experience, and the research we have undertaken has been some of the most satisfactory I have ever taken part in. I met some nice people there, too. I wish all the best to Albert, Julian, Elena, David, Jonas, Tobias, Max, Philipp, Anna, Moritz, and all the others. I will be more proficient in German next time around, I promise!

I would also like to thank my co-authors and collaborators, whose work has been crucial to the development of this thesis. I am indebted to the people at CSIR Bengaluru for their partnership in solar selective coatings. In particular, I have good memories of Atasi during her visit to Bilbao. I thank Lizzie (congrats!) and Renkun at UC San Diego for their support and useful discussions via e-mail. I hope we will meet at some point. I also acknowledge the efforts made by the people at the Southwestern Institute of Physics at Chengdu. I really look forward to carrying on working with you all. Por último, gracias también a Leire del Campo, por su inestimable ayuda desde antes incluso de empezar esta tesis y por la confianza que ha depositado en mí.

Por supuesto, nada de esto habría sido posible sin amigos que me apoyaran, escucharan o simplemente hicieran pasar un buen rato cuando hacía falta. Quiero dar las gracias de corazón a Iker, Iván y Jorge, mis mejores amigos de la carrera y unas buenas personas en las que siempre podré confiar. A mis pichas de Outer Heaven: Javi, Ibai, Alex y mi hermano Álvaro. También a otros tantos buenos amigos: Vicente, Jon, Naroa, Laura, Daniela, Bruno, Marina... Por supuesto, no me olvido de la cuadrilla del café ($M^2 + O$), por tanta terapia y salseo a buen precio. A la comunidad de *fisikaris* de la torre, tanto presentes como pasados: Óscar, Mikel, Xabimen, Peio, Lafu, Haritz, Sheila, Jon Balma, Paul, Santi, José Fernando, Patri, Leire y Gerardo. He disfrutado mucho hablando con vosotros de absolutamente toda clase de peregrinos temas, incluso esos viernes por la noche todavía sentados delante del ordenador. A Mikel le debo un agradecimiento adicional por todas las manos que me ha echado estos años. También quiero dar las gracias a miembros pasados, presentes y futuros de Zimatek. Os deseo a todos lo mejor. Gracias

también a otras muchas personas que me he encontrado por el camino: Laura, Lucía, Jonmi, Patri, Andrés, David y muchos otros que me llevaría demasiado tiempo citar.

Una vez llegados a este punto, me gustaría dedicar unas líneas a la memoria de Raúl Pérez, el director que nunca tuve el placer de disfrutar. Sinceramente, un día creí que nunca llegaría a empezar esta tesis. No sólo lo hice, sino que la terminé dejando atrás unos proyectos y un grupo que nunca habría imaginado en 2016. Coincidimos menos de lo que me hubiera gustado, pero guardo un gran recuerdo de aquellos inicios.

Asimismo, quiero expresar mi más sincera gratitud a Manolo Tello. Él ha sido, sin duda alguna, el motor detrás de los inicios de mi carrera científica. A él y a su incansable ilusión y buen humor le debo mi entrada al mundo académico por esta puerta tan poco convencional y *sexy* de la emisividad, con todo lo bueno que me ha traído. A día de hoy, todavía no sé qué me pasó por la cabeza para meterme en esto, pero no lamento ni un momento mi decisión. Gracias por confiar en mí.

Finalmente, quiero dar las gracias a mi familia, por su cariño y por haberme dado el apoyo, las herramientas y el entorno necesario para poder desarrollar esta interminable formación; y a Mai, pues sin ella nada de esto habría sido lo mismo.

Contents

List of Figures

List of Tables

List of Abbreviations

AM1.5	**A**ir **M**ass **1.5** solar irradiance standard
ANSI	**A**merican **N**ational **S**tandards **I**nstitute
APM	**A**dvanced **P**owder **M**etallurgy
ARMCO	**A**merican **R**olling **M**ill **CO**mpany
ASTM	**A**merican **S**ociety for **T**esting and **M**aterials
BIPM	**B**ureau **I**nternational des **P**oids et **M**esures
CCO$_4$	**C**u**C**r$_2$**O**$_4$
CCMO$_4$	**C**u$_{0.5}$**C**r$_{1.1}$**M**n$_{1.4}$**O**$_4$
CFMO$_4$	**C**u**F**e**M**n**O**$_4$
CGS	**C**entimeter-**G**ram-**S**econd system of units
CSP	**C**oncentrated **S**olar **P**ower
DC	**D**irect **C**urrent
DEMO	**DEMO**nstration Power Station
DLaTGS	**D**euterated **L-a**lanine-doped **T**riglycine **S**ulfate
EBM	**E**lectron-**B**eam **M**elting
EBSD	**E**lectron-**B**ack**S**catter **D**iffraction
FIR	**F**ar **I**nfra**R**ed
FTIR	**F**ourier-**T**ransform **I**nfra**R**ed
GUM	**G**uide to the Expression of **U**ncertainty in **M**easurement
HAIRL	**H**igh-**A**ccuracy **I**nfra**R**ed emissometer at **L**eioa
HT	**H**eat **T**reatment
ITER	**I**nternational **T**hermonuclear **E**xperimental **R**eactor
IUPAP	**I**nternational **U**nion of **P**ure and **A**pplied **P**hysics
JCGM	**J**oint **C**ommittee for **G**uides in **M**etrology
JET	**J**oint **E**uropean **T**orus
JIS	**J**apanese **I**ndustrial **S**tandards
LO	**L**ongitudinal **O**ptical phonon
MA	**M**echanical **A**lloying
MIR	**M**id **I**nfra**R**ed
NIR	**N**ear **I**nfra**R**ed

PDF	**P**robability **D**ensity **F**unction
PID	**P**roportional-**I**ntegral-**D**erivative controller
PTB	**P**hysikalisch-**T**echnische **B**undesanstalt
RF	**R**adio **F**requency
SEM	**S**canning **E**lectron **M**icroscopy
SS	**S**tainless **S**teel
TC	**T**hermo**C**ouple
TEM	**T**ransmission **E**lectron **M**icroscopy
TO	**T**ransverse **O**ptical phonon
UV	**U**ltra**V**iolet
VIS	**VIS**ible
WWWA	**W**/**W**AlN/**W**AlON/**A**l_2O_3
XPS	**X**-ray **P**hotoelectron **S**pectroscopy
XRD	**X**-**R**ay **D**iffraction
ZPD	**Z**ero-**P**ath **D**ifference

List of Symbols

a	optical path difference	dimensionless
A	surface area	m^2
C	solar concentration factor	dimensionless
C_1	first radiation constant	W μm^4 m^{-2} sr^{-1}
C_2	second radiation constant	μm K
E	irradiance	W m^{-2}
f	probability density function	
F_{i-j}	radiation configuration factor	dimensionless
$F_{a\rightarrow b}$	blackbody radiation fraction	dimensionless
$g(\vec{\xi})$	joint PDF with $\vec{\xi}$ parameters	
I	interferogram	V
I	radiant intensity	W sr^{-1}
k	coverage factor	dimensionless
l	sampling length of the profilometer	μm
L	radiance	W m^{-2} sr^{-1}
M	radiant exitance	W m^{-2}
M	number of Monte Carlo trials	
N	refractive index	dimensionless (complex)
n	real part of the refractive index	dimensionless
Q	ratio of measured signals	dimensionless
r	complex reflection coefficient	dimensionless (complex)
r	correlation coefficient	dimensionless
R_a	average roughness	μm
R_q	root-mean-square roughness	μm
R_z	average height of a roughness profile	μm
S	Fourier-transformed signal	V
s	surface specularity	dimensionless
s	standard deviation	
T	temperature	K

u	uncertainty	
x	length of the profile	μm
Z	roughness profile height	μm
α	absorptivity	dimensionless
ϵ	dielectric function	dimensionless (complex)
ε	emissivity/emittance	dimensionless
η	conversion efficiency	dimensionless
θ	polar angle	rad/$^\circ$
λ	wavelength	μm
ϕ	azimuthal angle	rad
Φ	radiant flux	W
φ	interferogram phase	rad
ρ	electrical resistivity	Ω cm
ρ	reflectivity/reflectance	dimensionless
σ	wavenumber	cm^{-1}
σ	conductivity	cm^{-1}
σ	Stefan-Boltzmann constant	W m^{-2} K^{-4}
τ	transmittance	dimensionless
ω	angular frequency	rad s^{-1}
Ω	solid angle	sr
$_{AM1.5}$	standard solar spectrum	
$_{bb1}$	high-temperature blackbody source	
$_{bb2}$	low-temperature blackbody source	
$_{c}$	combined	
$_{N}$	total normal	
$_{p}$	p (parallel) polarization	
$_{T}$	total directional	
$_{H}$	total hemispherical	
$_{S}$	solar	
$_{s}$	sample	
$_{s}$	s (perpendicular) polarization	
$_{sub}$	substrate	
$_{sur}$	surrounding chamber	
$_{t}$	thermal	
$_{0}$	DC	
$_{0}$	environment	
$_{\infty}$	high-frequency	

"People think of education as something that they can finish."

Isaac Asimov

Chapter 1

Introduction and objectives

Thermal radiation is one of the three modes of heat transfer, along with conduction and convection. It is the dominant mode in high-temperature and high-vacuum conditions, which makes its control a crucial step in the development of numerous industrial applications. It also bears significant physical relevance due to its connection to the early history of quantum physics through the celebrated blackbody radiation law.

Planck's formulation and later interpretation of the blackbody radiation law paved the way to Einstein's pioneer work on light *quanta* in 1905 and the subsequent quantum revolution. The interaction between radiation and matter formed the core of the old quantum theory in the 1910s and '20s (Ter Haar, 1967). However, infrared technology lagged significantly behind these theoretical milestones for decades. That would start to change in the interwar years once the great powers realized the potential of infrared detectors for night vision. In the years after the Second World War, infrared technology became one of the many fields of battle in the arms race between the USA and the USSR (Rogalski, 2012).

For half a century, the military and aerospace sectors encompassed most of the applications of thermal radiation, and most data on radiative properties of materials was kept in private reports of NASA and other government agencies. Interest in this topic faded during the '70s and '80s, before picking up steam again somewhere around 1990, with the development of new high-temperature ceramics and an increasing use of heat-transfer modelling to simulate industrial processes (Modest, 2013, Chapter 3). Nowadays, a second Golden Age of thermal radiation research can be said to be underway, with major theoretical advances in near-field thermal radiation and metamaterials with exotic emissive properties, as well as an ever-expanding range of

applications. Contemporary studies in thermal radiation are no longer an exclusive terrain of the military, with civilian applications growing every year. New prospects include, among others, the study of heat transfer in energy applications and advanced manufacturing techniques. Indeed, the current need for ever-increasing amounts of carbon-free energy motivates a global multidisciplinary task of a kind the world has never seen. This drives the development of a wide range of alternative energy solutions, as none of them can, by itself, offer a sufficiently fast response to the impending climate crisis.

To this end, the main objectives of this work are to improve the experimental procedures for direct emissivity measurements at UPV/EHU and to use these measurement capabilities for accurate characterization of materials for use in alternative energy applications (concentrated solar power and nuclear fusion). The global aim of this work is to improve the efficiency of materials for carbon-free energy harvesting technologies by improving the current knowledge of their optical properties and radiative heat transfer capabilities.

Following this brief introduction, the necessary theoretical background concerning optical properties and radiometry is introduced in Chapter 2, with more specific concepts being discussed in Appendices A to C to aid readership. Afterwards, Chapter 3 focuses on the description of the experimental device available at UPV/EHU for direct emissivity measurements, as well as the methodological aspects of the thesis. After an overview of the main instrumental features and the measurement method, most of the Chapter is devoted to introducing the updates carried out during this Ph.D. project.

Concerning the application of these experimental capabilities for the characterization of materials, Chapters 4 and 5 will deal with systematic studies of three different sets of new materials for alternative energy applications. In the case of Chapter 4, the materials concerned are used as solar energy absorber coatings for two different solar thermal energy applications. Both tungsten-based metal-dielectric coatings and copper-based spinel black paints have been studied, the former meant for vacuum applications (parabolic troughs) and the latter for solar tower power in air. On the other hand, Chapter 5 changes topic from solar thermal energy to nuclear fusion power, and is concerned with the development of new vanadium-base alloys for prototype reactors (ITER, DEMO), as well as the role microstructure plays in the thermal radiative properties of these alloys.

To conclude, Chapter 6 summarizes the methods and experimental results obtained, discusses their implications, and concludes this work with proposals for future lines of research.

Chapter 2

Theoretical background

2.1 Radiometric magnitudes

Radiometry is the field of study that covers electromagnetic radiation measurements. The most fundamental quantity in this field is radiant flux/power Φ and its spatial and spectral distribution. In this work, we will follow the IUPAP convention for describing the basic distributions (Cohen and Giacomo, 1987), which are shown in Table 2.1. The parameters relevant to radiation-matter interaction, relevant for the characterization of optical sources and materials, are defined following Howell, Mengüç, and Siegel, 2010. This Section includes a brief overview of the most important radiometric quantities and the relations among them.

TABLE 2.1: Basic radiometric magnitudes derived from the SI. Adapted from Pedrotti and Pedrotti, 1993, following the IUPAP (Cohen and Giacomo, 1987).

Term	Symbol (units)	Defining equation
Radiant flux	Φ (W)	$-$
Radiant exitance	M (W m^{-2})	$M = d\Phi/dA$
Irradiance	E (W m^{-2})	$E = d\Phi/dA$
Radiant intensity	I (W sr^{-1})	$I = d\Phi/d\Omega$
Radiance	L (W sr^{-1} m^{-2})	$L = dI/(dA\cos\theta)$

The four fundamental magnitudes to describe the spatial distribution of radiant flux are the exitance M, irradiance E, intensity I, and radiance L. Their spectral generalizations can be obtained by taking their amounts per unit spectral bandwidth (i.e., spectral radiance $L(\lambda)$ with units W sr^{-1} m^{-2}

μm^{-1}).[1] Confusion often arises in diverse subfields of physics when discussing these variables and their definitions. **Radiant exitance** M and **irradiance** E both describe the amount of radiation interacting with a surface, but differ in the direction in which the radiation is propagating: radiant exitance concerns radiation exiting a surface, while irradiance refers to the case of radiation incident upon the surface. The latter term is often incorrectly labelled I (e.g., in the solar energy field), which corresponds properly to **radiant intensity**, a property which describes the angular distribution of radiation without consideration of the size of the source. In the case of a planar source (the case at hand in this work), Lambert's cosine law states that the radiant intensity of a surface with angle-independent properties decreases with the polar angle of observation θ (Pedrotti and Pedrotti, 1993):

$$I(\theta) = I(0)\cos\theta. \tag{2.1}$$

Materials which obey this law are called diffuse or Lambertian. It is precisely this behavior which motivates the introduction of a cosine term in the definition of **radiance** L. This is a crucial property in radiometry, as it is an angularly invariant property for diffuse emitters or reflectors:

$$L(\theta) = \frac{I(\theta)}{dA\cos\theta} = \frac{I(0)}{dA} \equiv L(0). \tag{2.2}$$

Thus, the radiative properties of materials are generally best defined based on radiance quotients to account for directional properties, regardless of their diffuseness. The most important diffuse material is the ideal blackbody, whose main properties are reviewed below.

2.1.1 Radiative properties of blackbodies

A blackbody is an ideal material which absorbs all radiation which is incident upon it and emits the largest possible amount of radiation allowed by thermodynamics. The most fundamental law in thermal radiation is Planck's law, which gives the spectral distribution of radiances of an ideal blackbody source:

[1] Following the convention in the infrared radiometry field, μm will be used as the unit wavelength. Similarly, wavenumbers will be given in the standard spectroscopic unit of cm^{-1} ($\sigma = 10^4/\lambda$).

$$L_{bb}(\lambda, T) = \frac{2C_1}{\lambda^5(\exp(C_2/\lambda T) - 1)}, \tag{2.3}$$

where $C_1 = 0.59552{\cdot}10^8$ W μm^4 m^{-2} and $C_2 = 14388\,\mu$m K in the conventional units of infrared radiometry (Howell, Mengüç, and Siegel, 2010).

Blackbodies are diffuse radiators (i.e., they obey Equation 2.1), and so their emitted radiances do not change with angle. All other materials feature directionally dependent properties to a certain extent, a feature which will be discussed later. Thus, the spectral exitance of a blackbody source, which is obtained by integrating over all directions, is only π times its spectral radiance:

$$M_{bb}(\lambda, T) = \int_\Omega L_{bb}(\lambda, T) \cos\theta d\Omega = \pi L_{bb}(\lambda, T), \tag{2.4}$$

where $d\Omega = \sin\theta d\theta d\phi$ is the differential solid angle.

Similarly, the spectral radiance can be generalized to account for all emitted wavelengths (Howell, Mengüç, and Siegel, 2010):

$$L_{bb}(T) = \int_0^\infty L_{bb}(\lambda, T) d\lambda = \frac{2C_1\pi^4}{15C_2^4} T^4 \equiv \frac{\sigma}{\pi} T^4, \tag{2.5}$$

where $\sigma = 5.67 \cdot 10^{-8}$ W m^{-2} K^{-4} is the Stefan-Boltzmann constant.

Finally, the total exitance emitted by a blackbody is given by the well-known Stefan-Boltzmann law:

$$M_{bb}(T) = \sigma T^4. \tag{2.6}$$

2.1.2 Radiative properties of materials

The optical and thermal radiative properties of real materials are much more complex and diverse than those of an ideal blackbody source. This means that a significant number of additional magnitudes must be defined to deal with the creation and propagation of electromagnetic radiation in these materials. Scattering of radiation is not considered in this work, so all radiation is either emitted, absorbed, reflected, or transmitted. Thus, dimensionless magnitudes corresponding to these four basic processes must

be defined: emissivity/emittance (ε), absorptivity/absorptance (α), reflectivity/reflectance (ρ), and transmittance (τ). The use of the suffixes *-ivity* or *-ance* is not standardized. One criterion reserves the names ending in *-ivity* to ideal surfaces and theoretical results, and *-ance* to real materials (Modest, 2013). However, the criterion followed in this work is the one introduced by Howell, Mengüç, and Siegel, 2010, which uses the *-ivity* ending to refer to radiative properties of opaque materials (that is, surface-dependent properties), and the *-ance* one to refer to extensive radiative properties, in which the size of the material is relevant. Thus, in this work, layered and semi-transparent materials will be described with the *-ance* ending, whereas opaque materials will be described using the *-ivity* suffix. As the amount of transmitted radiation must depend on the thickness of the material, a surface-specific magnitude for transmission (transmissivity) is not considered in this work.

The definitions of the following thermal radiative properties have been adapted from Howell, Mengüç, and Siegel, 2010, Chapter 2. Dependences on the azimuthal angle ϕ have been neglected for simplicity.

Directional spectral emissivity

Ratio of the spectral radiance emitted by a surface element dA at temperature T per unit time within a spectral region $d\lambda$ and a solid angle element $d\Omega$ to that emitted by a blackbody in the same conditions (Equation 2.3):

$$\varepsilon(\lambda, \theta, T) = \frac{L(\lambda, \theta, T)}{L_{bb}(\lambda, T)}. \tag{2.7}$$

Directional total emissivity

Ratio of the radiance emitted by a surface into a given direction θ to that emitted by a blackbody:

$$\varepsilon_T(\theta, T) = \frac{\pi}{\sigma T^4} \int_0^\infty \varepsilon(\lambda, \theta, T) L_{bb}(\lambda, T) d\lambda. \tag{2.8}$$

In the particular case of the normal direction ($\theta = 0$), this parameter is often named **total normal emissivity** and labelled $\varepsilon_N(T)$.

Total hemispherical emissivity

Ratio of the exitance emitted by a surface relative to that emitted by a blackbody at the same temperature. It can be calculated as the ratio of spectral radiances when integrated over all wavelengths and directions:

$$\begin{aligned}\varepsilon_H(T) &= \frac{\int_\Omega \int_0^\infty \varepsilon(\lambda,\theta,T) L_{bb}(\lambda,T)\cos\theta d\lambda\, d\Omega}{\sigma T^4} \\ &= 2\int_0^{\pi/2} \varepsilon_T(\theta,T) L_{bb}(\lambda,T)\cos\theta\sin\theta d\theta.\end{aligned} \tag{2.9}$$

Absorptivity parameters can be defined in a similar way. The equality of the directional spectral emissivity and absorptivity (Kirchhoff's law) follows from basic thermodynamic relations and holds for all bodies at or near thermodynamic equilibrium (Howell, Mengüç, and Siegel, 2010). This equality is very useful to unify absorption and emission phenomena. However, it must be noted that this equality does not hold for the total magnitudes, because the radiation sources used for weighting the integrals differ.

Directional spectral absorptivity

Ratio of spectral radiance absorbed by a surface to that incident upon it from a particular solid angle element $d\Omega$. This is equal to the directional spectral emissivity by Kirchhoff's law:

$$\alpha(\lambda,\theta,T) = \frac{L_{abs}(\lambda,\theta,T)}{L_i(\lambda,\theta)} \equiv \varepsilon(\lambda,\theta,T). \tag{2.10}$$

Directional total absorptivity

Ratio of the radiance absorbed by a surface to that incident upon it from a given direction θ :

$$\alpha(\theta,T) = \frac{\int_0^\infty \alpha(\lambda,\theta) L_i(\lambda) d\lambda}{\int_0^\infty L_i(\lambda) d\lambda}. \tag{2.11}$$

When the incident radiation spectrum is the standard AM1.5 solar irradiance $E_{\text{AM1.5}}$ (ASTM, 2012), the total absorptivity is called solar absorptivity (α_S). The temperature dependence of this quantity is often neglected in

many applications, as it is often exclusively measured at room temperature. In this work, only the direct irradiance spectra of the standard (with total irradiance $E_{\text{AM1.5}} = 900.1$ W m^{-2}) will be considered for solar thermal energy applications; thus, the entire irradiance spectrum is located only in the $\theta = 0$ direction, and the total absorptivity is given by:

$$\alpha_S = \frac{\int_0^\infty \alpha(\lambda, 0^\circ) E_{\text{AM1.5}}(\lambda) d\lambda}{E_{\text{AM1.5}}}. \tag{2.12}$$

Nevertheless, for simplicity, all future references in this work to a total solar irradiance will be approximated to $E \sim 1000$ W m^{-2}, as is customary for estimations of irradiance in the solar thermal energy field.

Finally, in the case of the reflectivities and transmittances, definitions must take into account both the geometry of incidence and that of reflection/transmission. Thus, there are more parameters to be defined, although only those relevant for the present work will be introduced. For simplicity, no special mention will be given to spectral quantities or temperature dependence, which are both easily generalizable.

Bi-directional reflectivity

Ratio of the spectral radiance reflected by a surface in a given direction θ_r to the radiance incident upon it from the direction given by θ_i:

$$\rho(\theta_i, \theta_r) = \frac{L_r(\theta_r)}{L_i(\theta_i)}. \tag{2.13}$$

By Helmholtz's reciprocity principle (Howell, Mengüç, and Siegel, 2010), the incident and reflected rays can be inverted without affecting the geometry of reflection:

$$\rho(\theta_i, \theta_r) \equiv \rho(\theta_r, \theta_i, T). \tag{2.14}$$

Directional-hemispherical reflectivity

Ratio of the spectral radiance reflected by a surface in a given direction to the total irradiance incident upon it. By extension of Helmholtz's reciprocity relation, the directional-hemispherical and hemispherical-directional reflectivities must be identical:

$$\rho(\theta) \equiv \frac{L_r(\theta)}{E} = \frac{M_r}{L_i(\theta)}. \tag{2.15}$$

Bi-directional transmittance

Ratio of the radiance transmitted by the bulk material in a given direction to the radiance incident upon it from the direction given by θ_i:

$$\tau(\theta_i, \theta_r) = \frac{L_t(\lambda, \theta_t)}{L_i(\lambda, \theta_i)}. \tag{2.16}$$

Directional-hemispherical transmittance

Ratio of the radiance transmitted by the bulk material in a given direction to the irradiance incident upon it, equal to the hemispherical-directional transmittance:

$$\tau(\theta) = \frac{L_t(\theta_t)}{E} = \frac{M_t}{L_i(\theta)}. \tag{2.17}$$

By combining Kirchhoff's law and the principle of conservation of energy, the relationship between all these variables can be formulated. In particular, the following relation between spectral directional properties can be formulated:

$$\alpha(\lambda, \theta) + \rho(\lambda, \theta, T) + \tau(\lambda, \theta, T) = 1. \tag{2.18}$$

Then, using Kirchhoff's law (Equation 2.10) and assuming an opaque material, it can be proved that the directional spectral emissivity and the directional-hemispherical reflectivity are related by the following convenient expression:

$$\varepsilon(\lambda, \theta, T) = 1 - \rho(\lambda, \theta, T). \tag{2.19}$$

In the case of specular materials, it is possible to relate the directional spectral emissivity directly to the specular reflectivity $\rho(\theta_i = \theta, \theta_r = \theta)$, which is

given by Fresnel's equations (discussed below in Section 2.2.1). This is a particularly strong advantage for the interpretation of the optical properties of the surface, and, as such, the following Subsection deals with the distinction between specular and diffuse surfaces.

2.1.3 Diffuse and specular surfaces: roughness effects

Surface roughness plays a key role in determining the optical properties of materials due to a variety of mechanisms. The JIS B0601-2001 standard is used in this work to define the relevant roughness parameters to characterize the surfaces studied in this work (JIS, 2001). According to this standard, the roughness profile of the surface is measured along a linear profile with a mechanical profilometer for a number n of sampling segments of length l. The most common roughness parameters concern the basic statistical properties of the roughness height distributions, such as the average R_a and root-mean-square R_q. These parameters are evaluated only along the first sampling length:

$$R_a = \frac{1}{l}\int_0^l |Z(x)|dx. \tag{2.20}$$

$$R_q = \sqrt{\frac{1}{l}\int_0^l Z^2(x)dx}. \tag{2.21}$$

However, surface properties are often dependent on inhomogeneities much larger than the average, for which statistical parameter such as the distribution of peak-to-valley heights are commonly considered. This can be accomplished by evaluating the average maximum height of the profile, for which the total peak-to-valley height of each sampling length i is evaluated and averaged:

$$R_z = \frac{1}{n}\sum_{i=1}^{n}[\max Z_i(x) + |\min Z_i(x)|]. \tag{2.22}$$

There are two particular cases of reflecting surfaces: diffuse (Lambertian) and specular. Real materials fall between these two categories. Nevertheless,

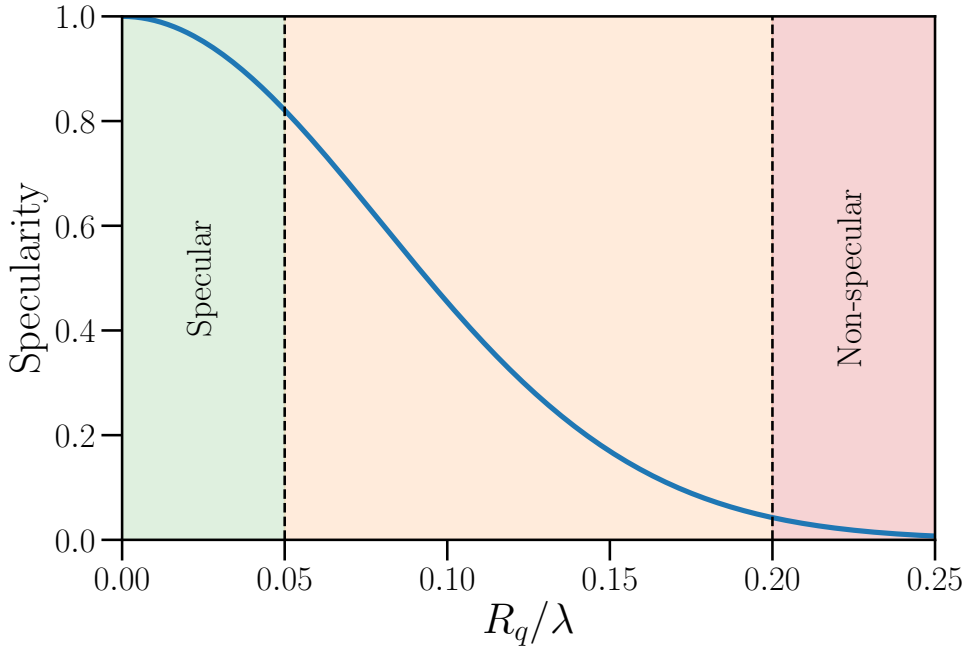

FIGURE 2.1: Illustration of the specularity index as defined by Stagg and Charalampopoulos, 1991 (Equation 2.23). Arbitrary limits to the specular, hybrid, and non-specular regions have also been drawn.

it is important to take into account the specularity of the material when relating the emissive and reflective properties. Stagg and Charalampopoulos, 1991 define the specularity of a surface whose roughness profile is approximately described by a Gaussian distribution as:

$$s = \exp\left(\frac{-8\pi^2 R_q^2}{\lambda^2}\right). \tag{2.23}$$

The specularity of a Gaussian surface is shown in Figure 2.1 as a function of the R_q/λ ratio, where it can be seen that only surfaces with root-mean-square roughness values well below an order of magnitude lower than the wavelength can be accurately characterized as specular. A commonly cited limit of $R_q/\lambda = 0.2$ for a surface to be considered specular can be found in

the literature (Wen and Mudawar, 2006). However, it can be seen from Figure 2.1 that this limit only separates the non-specular region from a hybrid regime with partial specularity. Thus, a more restricted limit of $R_q/\lambda = 0.05$ is suggested for evaluation of the potential specularity of a given surface.

Other criteria have been suggested, often referring to more complex parameters than those characterizing the roughness height distribution. Often, average parameters such as R_a and R_q do not correlate well with observed effects for surfaces with non-Gaussian roughness profiles (a key assumption for the derivation of Equation 2.23). In these cases, the distribution of irregularity slopes is often the most useful parameter for describing the roughness profile (Yang and Buckius, 1995). This can be combined with metrics describing the roughness height extremes (e.g., $R_z < 1$ μm) to provide accurate correlations between surface properties and the optical response of materials (Nakar and Feuermann, 2016). Further discussion of these considerations falls outside the scope of this work.

2.2 Optical properties of materials

2.2.1 Dielectric functions and Fresnel's relations

The theory of optical properties of materials is a rich and constantly expanding field. Even though this thesis concerns mostly experimental results with direct applications, it is worth spending some time delving into some basic optical theory in order to fully understand the results shown. Therefore, this Section includes a swift revision of the most basic optical concepts required for the interpretation of emissivity results.[2]

The most fundamental parameter in materials optics is the dielectric tensor $\overline{\overline{\epsilon}}$, which relates the electric field $\vec{E}$ and the electric displacement field $\vec{D}$ inside an optically linear material:

$$\vec{D}(\omega) = \overline{\overline{\epsilon}}(\omega)\vec{E}(\omega). \tag{2.24}$$

Similarly, the response current field $\vec{J}$ induced in a material by the same electric field $\vec{E}$ is given by the electrical conductivity tensor $\overline{\overline{\sigma}}$:

$$\vec{J}(\omega) = \overline{\overline{\sigma}}(\omega)\vec{E}(\omega). \tag{2.25}$$

[2]The entire Section 2.2 will use Gaussian CGS units for simplicity of the resulting equations, unless explicitly noted.

Assuming a cubic or isotropic material, all the quantities above can be described by scalars. The relation between the (complex) scalar dielectric function and electrical conductivity is given by Maxwell's equations (Dressel and Grüner, 2002):

$$\epsilon(\omega) = 1 + \frac{4\pi}{\omega} i\sigma(\omega). \tag{2.26}$$

Thus, it can be seen that the complex electrical and dielectric responses of a solid are essentially the same. Both of these quantities can be further related to more conventional optical parameters, such as the (complex) refractive index:

$$N(\omega) = n(\omega) + ik(\omega) = \sqrt{\epsilon(\omega)}. \tag{2.27}$$

From these basic magnitudes, some observables can be formulated using Maxwell's equations and setting boundary conditions in the interfaces. The reflection factors of a specular surface ($s \to 1$ in Equation 2.23) can be obtained from Fresnel's relations, as a function of the angle of incidence θ_i and the complex refractive index N (Dressel and Grüner, 2002):

$$r_s \equiv r_\perp = \frac{E_{rs}}{E_{is}} = \frac{\cos\theta_i - (N^2 - \sin^2\theta_i)^{1/2}}{\cos\theta_i + (N^2 - \sin^2\theta_i)^{1/2}}. \tag{2.28}$$

$$r_p \equiv r_\parallel = \frac{E_{rp}}{E_{ip}} = \frac{N^2\cos\theta_i - (N^2 - \sin^2\theta_i)^{1/2}}{N^2\cos\theta_i + (N^2 - \sin^2\theta_i)^{1/2}}. \tag{2.29}$$

These factors correspond to ratios between electric field amplitudes for both light polarizations. The reflectivities are obtained by taking their squares:

$$\rho_s = |r_s|^2. \tag{2.30}$$

$$\rho_p = |r_p|^2. \tag{2.31}$$

The unpolarized reflectivity is given by the average of the two components:

$$\rho = \frac{\rho_s + \rho_p}{2}. \tag{2.32}$$

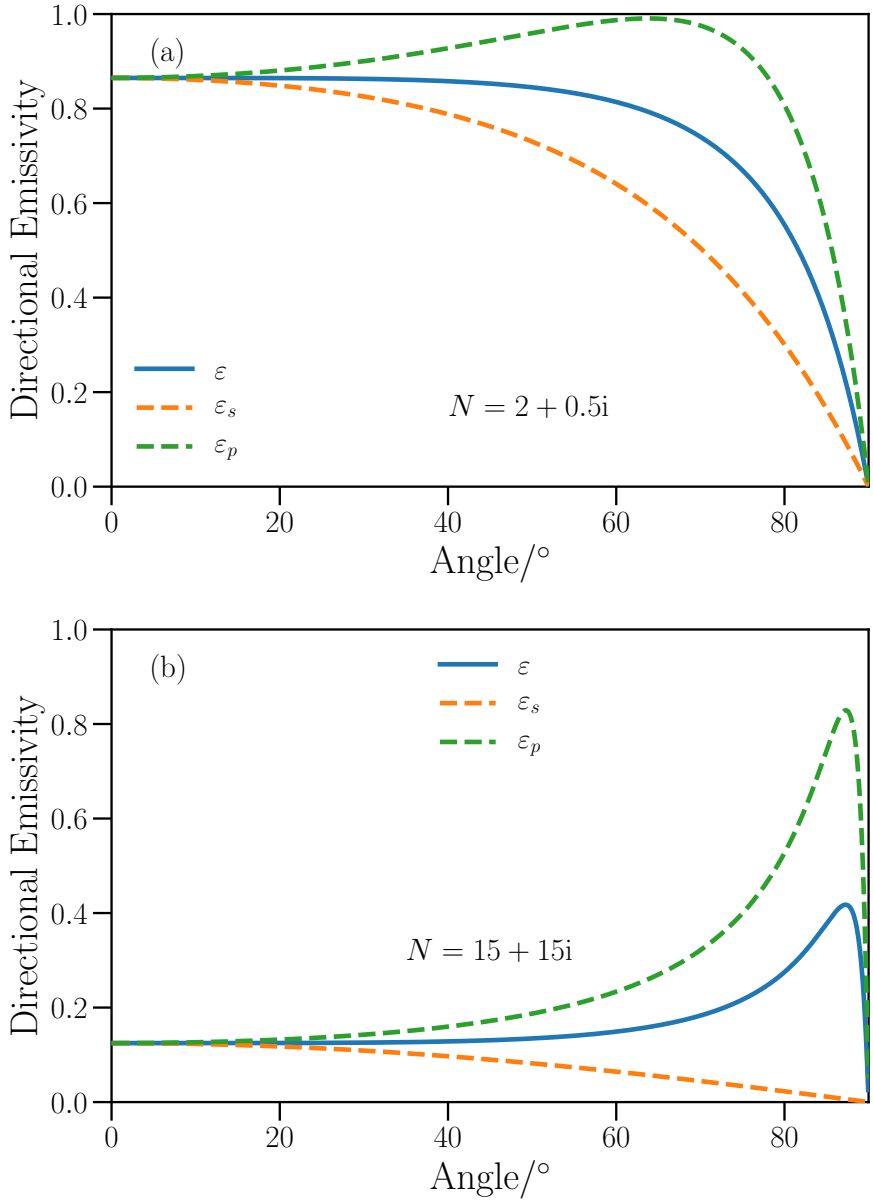

FIGURE 2.2: Directional spectral emissivities for two model materials with refractive index values typical of (a) dielectric materials and (b) metals.

Together, Equations 2.28 to 2.32 allow calculating the bi-directional spectral reflectivity of an ideal surface, which equals 1 minus the directional spectral emissivity for an opaque material. The typical directional emissivities of metallic materials (large $|N|$) and dielectric materials (small $|N|$) are plotted in Figure 2.2, together with their polarized components. Non-ideal surfaces require taking into account the diffusion of light by the surface roughness (Stagg and Charalampopoulos, 1991). In that case, the relation between both parameters breaks down.

In the particular case of normally incident radiation, the normal spectral reflectivity is given by:

$$\rho(\theta = 0) = \left|\frac{1-N}{1+N}\right|^2 = \frac{(1-n)^2 + k^2}{(1+n)^2 + k^2}. \tag{2.33}$$

This is the equation most commonly used to relate the standard optical properties with the microscopic models of matter, which usually predict response functions that can be translated into dielectric functions.

2.2.2 The Drude-Lorentz model

Many phenomenological models have been proposed throughout the years for optical modelling of materials. The most basic framework for qualitatively describing these properties is still the centenary Drude-Lorentz model, a simplified theory based on the assumption that optical materials behave as ensembles of classical electric oscillators. In the most basic case (conductors), the electrons of the materials have no restoring force and behave as a viscous fluid. This leads to the most basic model for describing the optical properties of a metal, the Drude model (Dressel and Grüner, 2002):

$$\sigma(\omega) = \frac{\sigma_0}{1 - i\omega\tau} \implies \epsilon(\omega) = \epsilon_\infty - \frac{4\pi\sigma_0/\tau}{\omega^2 - i\omega/\tau} \equiv \epsilon_\infty - \frac{\omega_p^2}{\omega^2 - i\omega\gamma}, \tag{2.34}$$

where σ_0 is the DC conductivity, ϵ_∞ is a sum of all the additional dielectric responses which do not contribute to the conductivity, $\omega_p = (4\pi\sigma_0/\tau)^{1/2}$ is the plasma frequency, τ is the electron relaxation time, and $\gamma = 1/\tau$ is the electron relaxation frequency or scattering rate.

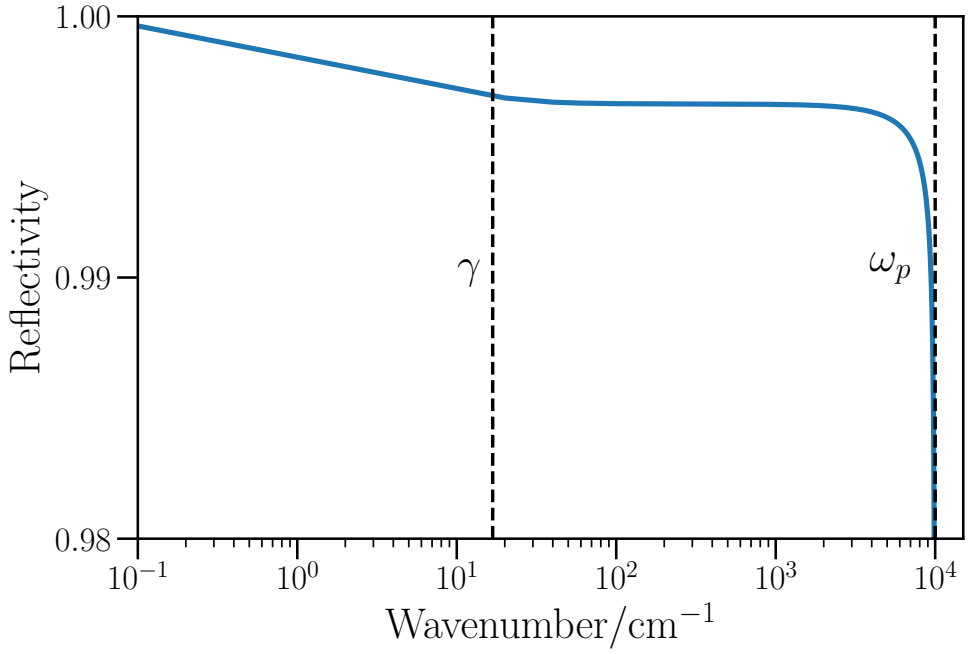

FIGURE 2.3: Reflectivity of a model metal ($\epsilon_\infty = 1$, $\omega_p/2\pi c = 10^4$ cm^{-1}, $\gamma/2\pi c = 16.8$ cm^{-1}).

This typical metallic behavior is illustrated in Figure 2.3 using data from Dressel and Grüner, 2002. The values correspond to an ideal metal with parameters which are representative of good conductors at low temperatures. Three different regions can be discerned, separated by the representative frequencies γ and ω_p.

In the case of materials whose optically active components do have a restoring force (i.e., harmonic vibrations of lattice ions), the Lorentz model is obtained by solving the equation of motion of a charged damped harmonic oscillator:

$$\epsilon(\omega) = \epsilon_\infty + \frac{\omega_p^2}{\omega_{TO}^2 - \omega^2 + i\gamma\omega}. \tag{2.35}$$

The restoring frequency ω_{TO} corresponds to the transverse normal mode of the material. In real dielectrics, these normal modes correspond with

the quantizations of the crystal lattice vibrations. These modes are known as phonons and can be classified into transverse or longitudinal, as well as acoustic or optical (Kittel, 1996). As their name suggests, only optical modes can couple to electromagnetic radiation, which is the reason why their frequencies are labelled ω_{TO} in Equation 2.35. It is easy to see that transverse phonons correspond to the poles of the dielectric function. In a similar way, longitudinal phonons can be defined as the frequencies for which the dielectric function becomes zero in the absence of damping (Kittel, 1996):

$$\epsilon(\omega) = \epsilon_\infty + [\epsilon_0 - \epsilon_\infty]\frac{\omega_{TO}^2}{\omega_{TO}^2 - \omega^2} \equiv \epsilon_\infty\left(\frac{\omega_{LO}^2 - \omega^2}{\omega_{TO}^2 - \omega^2}\right). \tag{2.36}$$

2.2.3 Extended optical models

A more useful form of the Lorentz oscillator formula can be derived by factorizing it into poles (longitudinal modes) and zeros (transverse ones). If each of these are described using complex number, in order to account for lifetime broadening, we obtain (Berreman and Unterwald, 1968):

$$\epsilon(\omega) = \epsilon_\infty\frac{\omega_{LO}^2 - \omega^2 + i\gamma_{LO}\omega}{\omega_{TO}^2 - \omega^2 + i\gamma_{TO}\omega}. \tag{2.37}$$

This equation is sometimes called the four-parameter Lorentz model, and it is more flexible than the standard three-parameter model, as it allows for distinct scattering rates for both phonons. An additional advantage of the four-parameter model is that it can be used to describe the response of a conducting material ($\Omega_T = 0$) in which the scattering rates are significantly different at DC and infrared frequencies. This is typical of weakly conducting materials, where the concentration of charge carriers is not high enough to screen their Coulomb interactions (Gervais, 2002). Thus, their Drude-like scattering rate experiences a strong frequency dependence, which can be described by a generalized Drude-Lorentz model (Gervais, 2002):

$$\epsilon(\omega) = \epsilon_\infty\left[\frac{\omega_{LO}^2 - \omega^2 + i\gamma_{LO}\omega}{\omega_{TO}^2 - \omega^2 + i\gamma_{TO}\omega} - \frac{\Omega_p^2 - i(\gamma_p - \gamma_0)\omega}{\omega^2 - i\gamma_0\omega}\right]. \tag{2.38}$$

where γ_0 is the scattering rate of charge carriers at DC, γ_p the scattering rate at the plasma frequency, and the renormalized plasma frequency is related to that of the standard Drude model (Equation 2.34) by $\Omega_p = \omega_p/\sqrt{\epsilon_\infty}$.

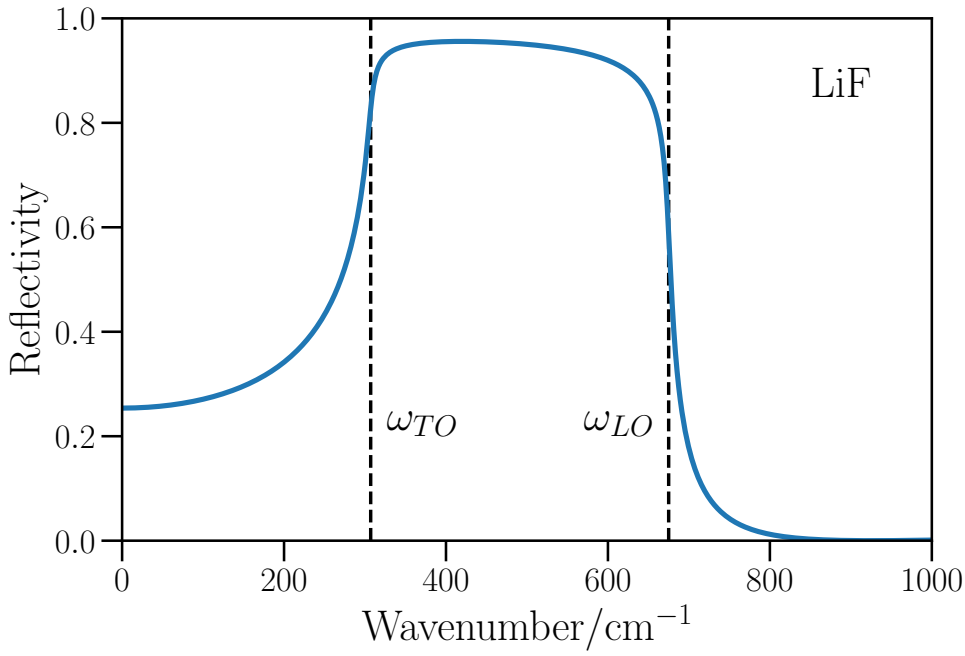

FIGURE 2.4: LiF theoretical reflectance reproduced using phonon frequency data reported in Kittel, 1996, and assuming $\gamma_{TO}/2\pi c = \gamma_{LO}/2\pi c = 10$ cm^{-1}.

2.2.4 Electrical and optical properties

Real materials hardly ever follow simple Drude-Lorentz behaviors. However, this framework is still useful to qualitatively understand the main optical properties of materials. Furthermore, it allows obtaining simplified expressions which are useful for estimating thermal radiative properties from more easily measured magnitudes. In particular, the relation between the electrical properties of conducting materials and their optical properties can be exploited for deriving useful relationships. Some common relations for the analysis of thermal radiative properties of metals can be found in Sievers, 1978. For example, in the $\omega\tau \ll 1$ regime, it is possible to define a simplified value for the emissivity of a metal which only depends on its DC electrical properties. This equation is known as the Hagen-Rubens relation (Sievers, 1978):

$$\varepsilon(\lambda, T) = \frac{2}{\omega_p \tau}(2\omega\tau)^{1/2}. \tag{2.39}$$

This equation predicts a square-root dependence of the spectral emissivity, which is observed in real metals, such as those studied in Chapter 5. It is also often expressed explicitly as a function of the electrical resistivity:

$$\varepsilon(\lambda, T) = 36.5\left(\frac{\rho}{\lambda}\right)^{1/2}. \tag{2.40}$$

where ρ is the electrical resistivity in Ω cm.

In the opposite extreme ($\omega\tau \gg 1$), we obtain the Mott-Zener result (Sievers, 1978):

$$\varepsilon(\lambda, T) = \frac{2}{\omega_p \tau}. \tag{2.41}$$

This relation, which predicts a wavelength-independent spectral emissivity, is not applicable to the materials studied in this work, as it relies on the assumption of a very large electrical conductivity (large relaxation time τ between collisions). Nevertheless, it can be useful to describe noble metals and other good electrical conductors. These two approximations correspond to the regimes that can be observed in Figure 2.3, where the low-frequency reflectivity decreases with frequency and the high-frequency response remains flat up to the point of transparency at the plasma frequency.

Finally, one of the most useful relations which can be obtained from the Hagen-Rubens approximation is its its generalization for the total hemispherical emissivity. This relation was first derived by Davisson and Weeks, but the version quoted here includes the corrections introduced by Parker and Abbott (Sievers, 1978):

$$\varepsilon_H(T) = 0.766(\rho T)^{1/2} - [0.309 - 0.0889\ln(\rho T)](\rho T) - 0.0175(\rho T)^{3/2}, \tag{2.42}$$

where ρ is given in Ω cm.

As electrical resistivities of metallic materials often increase linearly with temperature, Equation 2.42 predicts an approximately linear, if slightly concave downwards, temperature dependence for the total hemispherical emissivity of most electrically conducting materials.

The relations above apply only to certain approximated versions of the optical behavior of metals. A general expression for the Drude model is given by Ordal et al., 1985:

$$\sigma = \frac{1}{2\pi c}\frac{\omega_p^2}{4\pi\gamma}, \tag{2.43}$$

where the electrical conductivity σ is given in the customary spectroscopic units of cm^{-1}.

This effective optical conductivity can be traced back to more conventional units by the following relation:

$$\sigma[\mathrm{cm}^{-1}] = \frac{9 \cdot 10^{11}}{2\pi c(\rho[\Omega cm])}. \tag{2.44}$$

This general relation allows for indirect estimates of the effective optical conductivity. Nevertheless, it does not necessarily correspond exactly to an independent measurement of the DC electrical resistivity, as many materials do not follow a simple Drude formula and its optical response may be more complex, as is typical of transition metals (Ordal et al., 1985).

Chapter 3

Emissivity measurement methods and uncertainty budget

3.1 Introduction

The infrared emissivity is an essential thermophysical property for a number of scientific and industrial applications, and thus great efforts have been devoted to developing robust measurement methods and protocols. However, this property has been notoriously difficult to characterize, as it depends not only on the intrinsic properties of the material but also on extrinsic parameters concerning its surface state, thickness and microstructure. Despite the apparent simplicity suggested by Equation 2.7, this property remains poorly studied to this day.

The lack of well-established experimental procedures and reference materials complicates the comparison of data among different research groups. Intercomparisons are key to establish reliable uncertainty budgets and procedures, as well as to check the accuracy of the claimed results and reveal the presence of systematic errors (Pavese, 2009). However, only a few attempts at such intercomparisons have been made to date (Le Baron et al., 2019; Cárdenas-García and Monte, 2014; Redgrove and Battuello, 1995; Hanssen et al., 2016; Filtz and Hameury, 2000). Moreover, no available international standard covers methods common to a wide range of research groups, with only the most simple instruments and methods being standardized by international organizations. These shortcomings are specially troublesome in thermophysics, as even standardized techniques can be subject to the adverse effects of temperature on measurement standards (Rudtsch et al., 2005). Taking

all of the above into consideration, the 2015 European Roadmap of Thermophysical Properties identified the need to develop improved uncertainty budgets and reference materials as key goals for the thermophysical community (Filtz et al., 2015).

There are many experimental devices capable of emissivity measurements, which vary in their methodology, calibration procedures, temperature measurement method, and heating system, among others. A comprehensive review up to 2015 can be found in Honner and Honnerová, 2015, while newer instruments have been surveyed in González de Arrieta et al., 2020. The University of the Basque Country (UPV/EHU) has contributed to the development of emissivity measurement facilities with the HAIRL emissometer (High Accuracy InfraRed, Leioa), built from original designs (del Campo et al., 2006b), as well as several references on the development of emissivity measurements (Pérez-Sáez, Campo, and Tello, 2008; González-Fernández et al., 2010; del Campo et al., 2010; Echániz, Pérez-Sáez, and Tello, 2017). As part of the more recent efforts at improving the metrological quality of this device, it has recently taken part in a Round Robin test for intercomparison of emissivity measuring devices (Le Baron et al., 2019). However, some of its features required a significant update in order to be able to cope with new challenges. For example, emissivity measurements for near-room-temperature applications, such as solar cells, biomaterials, textiles or polymers, require a particularly careful estimation of the uncertainty budget (Zhang et al., 2017; Ishii and Ono, 2001). Furthermore, low-emitting materials (such as noble metals) have also been known to require more sensitive treatment of the uncertainty in order to bridge together the often conflicting results from different emissivity measurements setups (Woods et al., 2014; Hameury et al., 2018).

The standard practice for calculating uncertainty budgets is to follow the *Guide to the Expression of Uncertainty in Measurement* (GUM, JCGM, 2008a). A previous uncertainty budget for the HAIRL device is available in the literature (del Campo et al., 2010). However, important advances have been made ever since. Several sources of uncertainty have been calculated in a more rigorous way, while sources of systematic errors have also been identified. Originally, only a metallic material (commercial-purity ARMCO iron) was considered, whereas a more general treatment of the uncertainty would be desirable to deal with other materials. This iron standard was previously used as a reference material by this laboratory (del Campo et al., 2006a), but its limitations have been noticed in recent years when aiming for more reliable high-temperature measurements. In addition to metals, measurements

on ceramics are also of great technological importance, but they were not discussed in the previous uncertainty budget. Their high emissivities also allow them to be measured at temperatures lower than those possible for metals in this setup ($300 - 373$ K). Finally, no discussion was given in del Campo et al., 2010 in the case of directional or total emissivity measurements and their uncertainties.

This Chapter introduces the HAIRL emissometer and its updated technical specifications, and reviews recent improvements to the measurement methodology and the revised uncertainty budget. This new budget is derived following the guidelines stated in the GUM and has been computed for representative materials covering a range of temperatures and emissivities. Calculations of integrated total emissivities and their uncertainty propagation using a Monte Carlo method (JCGM, 2008b), are also derived. The obtained results have been compared to literature data, and results corresponding to a tentative comparison with the Physikalisch-Technische Bundesanstalt (PTB) are also included.

3.2 Experimental device

The experimental device used in these measurements is the HAIRL emissometer, which has been in use for more than 14 years (del Campo et al., 2006b). It is based on a T-form geometrical configuration described schematically in Figure 3.1. It consists of a Fourier-transform infrared spectrometer (FTIR), a vacuum sample chamber, a commercial blackbody source (Isotech Pegasus R) and an optical entrance box that allows switching between the blackbody source and the sample chamber by a rotating plane mirror. The updated technical parameters are listed in Table 3.1. Note that some of these ranges may not be applicable for all measurements. The spectral resolution is given in wavenumber units by convention ($\sigma = 10^4/\lambda$).

The spectrometer is a Bruker IFS 66v/S vacuum model. Its optical system consists of conventional KBr optics, a Ge/KBr beamsplitter, and a thermal DLaTGS detector. The interferometer has the optical entrance system attached directly to its external port and share the same vacuum system. The optical entrance contains a plane switching mirror to select between the radiance coming from the sample chamber and that coming from the high-temperature blackbody source side, as well as two parabolic mirrors to redirect these radiances to the focal point of the FTIR. The low-temperature blackbody source

Parameter	Range
Wavelength (λ, μm)	$1.43 - 25$
Viewing angle (θ, $^\circ$)	$0 - 80$
Temperature (T, K)	$300 - 1273$
Pressure (P, hPa)	$10^3 - 5 \cdot 10^{-5}$
Resolution ($\Delta\sigma$, cm^{-1})	8, 16
Numerical aperture (NA)	0.062

TABLE 3.1: List of updated standard parameters for emissivity measurements in the HAIRL device.

is located inside the optical box, in the form of a steel shutter that has been coated with Nextel 811-21 black paint. Relatively low spectral resolutions of $\Delta\sigma = 8 - 16$ cm^{-1} and a relatively high numerical aperture of 0.062 (corresponding to an emission semi-angle of 3.58°) have been chosen so as to maximize the signal-to-noise ratio of the instrument (Griffiths and De Haseth, 1986, Chapter 7). Details on the fundamentals of this technique and the data analysis can be found in Appendix A.

The sample chamber consists of a double-wall stainless steel structure, coated with Nextel 811-21 black paint to avoid multiple reflections. A cooling system allows controlling the temperature by running water inside the double wall. The sample holder is located on top of a rotating axis to allow for directional measurements. The vacuum system, which previously consisted on a simple rotary pump (base pressure 10^{-3} hPa), has been upgraded to a rotary-backed turbomolecular pump (10^{-5} hPa). This allows measuring metals at higher temperatures due to the reduced risk of oxidation. A Zr foil can be used as an oxygen getter for measurements on highly reacting materials, such as titanium or vanadium alloys (Echániz et al., 2019). Not all measurements shown in this thesis were performed when this vacuum setup was available, which will be noted in the following Sections.

The sample heating system consists of a resistive wire located in the back of the sample, which heats it directly by radiation. This method improves the heating power when compared to a previous conduction-based method (del Campo et al., 2006b), which has allowed for higher measurement temperatures. It also potentially avoids radial thermal gradients across the base plate surface. The standard heating wire is made of Kanthal® APM, a dispersion-strengthened FeCrAl alloy which can reach temperatures up to 1523 K in air;

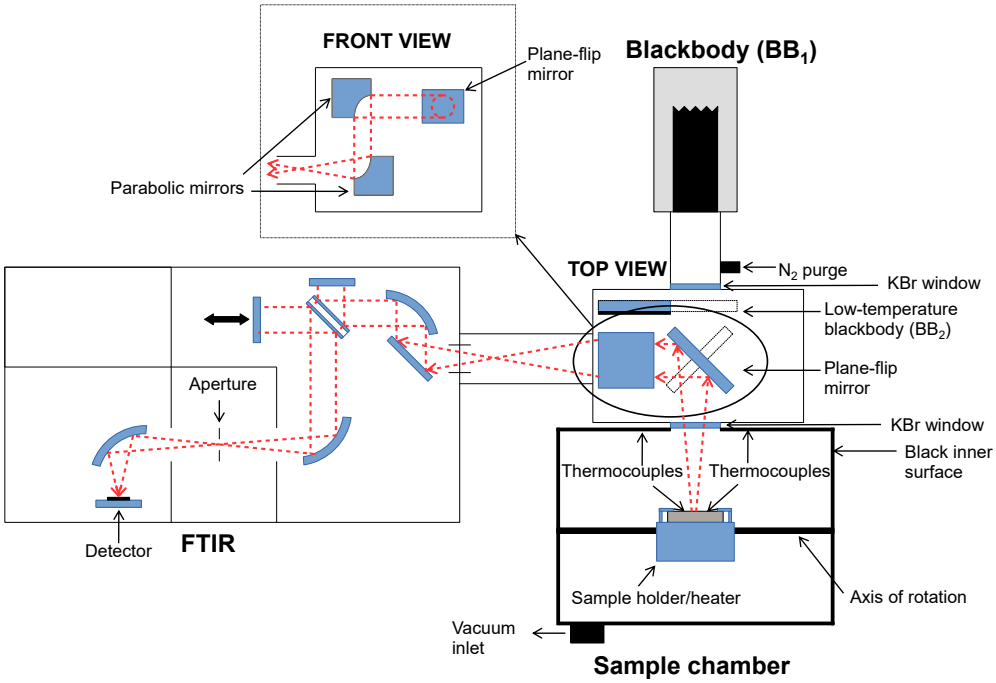

FIGURE 3.1: Schematic view of the HAIRL emissometer.

whereas high-temperature vacuum measurements can be made using a sintered quality Ta heating wire from Plansee (99.95% purity), which allows sample surface temperatures in the $1173 - 1273$ K range (González de Arrieta et al., 2016). This new upper temperature limit is substantially higher than the original 1050 K value reported in del Campo et al., 2006b.

Typical sample sizes are disks of $\varnothing 60$ mm or rectangular samples of 40×20 mm^2 in a sample holder of $\varnothing 60$ mm. Typical thicknesses range from 0.5 mm to 3 mm, with thicker samples experiencing an excessive axial temperature gradient due to the back-heating configuration. Surface temperature is measured, when possible, by two Type K thermocouples,[1] which are spot-welded to the surface 5 mm away from the center. Each wire is spot-welded independently onto the surface (intrinsic method) to minimize systematic mounting errors or contact spots away from the surface (Keltner and Beck, 1983). The wire

[1]Composition of the legs: Ni-10Cr vs. Ni-2Al-2Mn-1Si (mass%).

diameter is 0.2 mm, in order not to excessively disturb the temperature distribution by heat conduction. Alternatively, the thermocouples can be mounted by drilling holes through the material and making mechanical contact at the surface. This method can be described as an intrinsic method with contact resistance (Keltner and Beck, 1983). Differences between the two mounting methods will be discussed in Section 3.4.2. For ceramic materials, which cannot be welded, an alternative radiometric temperature measurement method is performed, which will be discussed in Section 3.4.3.

The high-temperature blackbody employed is a commercial high-emissivity tubular furnace (Isotech Pegasus R) with a diameter of $\varnothing 20$ mm, a depth of 65 mm, and an emissivity that is certified to be at least 0.995. It is made of graphite and features a diffuse surface and a bottom formed of 120° cones to deflect light away from the aperture. Its temperature is controlled by a PID controller and measured with a calibrated Type R thermocouple[2] embedded into the bottom of the tube below the textured surface. This radiance reference can be purged with N_2 gas. In contrast, the low-temperature reference is a steel disk painted with Nextel 811-21 black paint, acting as a graybody. Its temperature is measured by a single Type K thermocouple.

3.3 Measurement and calibration method

3.3.1 Previous approach

Direct methods for emissivity measurement and their systematic errors are reviewed in Pérez-Sáez, Campo, and Tello, 2008. The main problem in these measurements is how to separate the emission of the sample from the unavoidable reflections of radiation emitted or reflected by the surroundings. The most general method takes all radiance sources and reflections into account using complicated radiative configuration factors F_{i-j} (Howell, Mengüç, and Siegel, 2010), but it is in general quite complicated to implement. One way to greatly simplify this calculation is the *blacksur* approximation, which has been deemed the most accurate of the simplified direct radiometric methods (Pérez-Sáez, Campo, and Tello, 2008). This method models the sample chamber as a blackbody environment with a much larger area than both the IR window and the sample. Thus, the radiation transfer can be simplified

[2]Composition of the legs: Pt-13Rh vs. Pt (mass %).

without incurring in large systematic errors. The assumption of a large enclosure simplifies the calculation of the configuration factors ($F_{s-sur} = 1$) and the assumption of a very black surface allows neglecting the effects of multiple reflections between the chamber and sample. Therefore, the spectral radiance coming out of the chamber window can be described by a simple combination of the self-emitted sample radiation and the enclosure blackbody radiation reflected on the sample:

$$L^* = \varepsilon L_s + \rho L_{sur} = \varepsilon L_s + (1 - \varepsilon) L_{sur}, \tag{3.1}$$

where L^* is the effective directional spectral radiance, ε is the directional spectral emissivity of the sample, $\rho = 1 - \varepsilon$ is its directional-hemispherical reflectivity, L_s is the blackbody spectral radiance emitted at the sample temperature, and L_{sur} is the blackbody spectral radiance emitted at the surroundings temperature.[3]

For linear detectors like DLaTGS, the following relation between the measured signal and the radiance coming from the sample can be defined:

$$S_s = R A_s F_{s-det} L^* + S_0, \tag{3.2}$$

where S_s is the measured signal coming from the sample chamber, R stands for the response function of the FTIR, A_s for the sample emission area, F_{s-det} for the radiation configuration factor between the measured spot and the detector, and S_0 for the background signal inside the spectrometer.

A calibration procedure is required to translate interferometrically measured signals into real radiances. This procedure is performed by the modified two-temperature method, in which two blackbody sources at widely different temperatures are measured to calculate the linear response of the instrument. This method has been discussed in the literature and compared satisfactorily to the more common multi-temperature and two-temperature approaches (González-Fernández et al., 2010). It is a modified version of the standard two-temperature approach in which reference emissivity values lower than the ideal value of 1 are considered. In this calibration method, two independent sources of blackbody radiation (a high-temperature source bb_1 and a room temperature one bb_2) are used, which allows for a much faster calibration than by using the same source at two different temperatures. Potential calibration errors are minimized by measuring the two blackbody sources at

[3]For convenience of notation, blackbody radiances as described by Equation 2.3 will be referred to in this Chapter only by the subscript of their associated temperature: $L_{bb}(T_i) \equiv L_i$.

temperatures as far apart as possible ($\Delta T \sim 800$ K) and keeping one of them near room temperature in order to properly account for the contribution of the background radiation S_0 (González-Fernández et al., 2010).

The system of equations required for calibration is thus:

$$S_{bbi} = RA_{bbi}F_{bbi-det}\varepsilon_{bbi}L_{bbi} + S_0 \qquad i = 1, 2. \tag{3.3}$$

Since both radiance references are located along the same optical path, $A_{bb1}F_{bb1-det} = A_{bb2}F_{bb2-det}$ was assumed previously. If the observed areas and configuration factors corresponding to the sample and reference measurements also coincide, then the definition of the R factor can incorporate them through $RA_sF_{s-det} = RA_{bb1}F_{bb1-det} \equiv R^*$. Finally, the previously employed measurement equation for the *blacksur* method is obtained by combining Equations 3.1 to 3.3 (del Campo et al., 2010):

$$\varepsilon = \frac{S_s - S_0 - R^*L_{sur}}{R^*(L_s - L_{sur})}. \tag{3.4}$$

On a final note, another source of systematic errors was identified in Echániz, Pérez-Sáez, and Tello, 2017. When measuring directional emissivities at normal incidence in reflecting materials, parasitic signals different from S_0 may arise and need to be filtered out. These correspond to multiple reflections of detector and sample emissions along the optical path that increase significantly the effective measured signal. Therefore, in order for Equation 3.4 to be applicable, measurements need to be taken at off-normal emission angles. To that end, measurements reported as normal emissivities in this work correspond properly to directional measurements at a relatively low incidence angle of $10°$.

3.3.2 New approach

Equation 3.4 has been recently modified in order to account for additional measurement parameters and to improve its reliability. Firstly, the possibility of an anisotropic response in the configuration factors of both sides of the optical entrance is taken into consideration by introducing an anisotropic response function $a(\lambda)$. This is assumed to stem from non-ideal optical surfaces (Chamberlain, 1979, Chapter 8), and results in the configuration factors for the sample and the references not being equal ($F_{s-det} = aF_{bb-det}$, where a is a measurable optical path difference factor). Secondly, the emissivities of

the blackbodies were not considered explicitly in the previous equation and their uncertainties were neglected. Moreover, the emissivity of the commercial high-temperature blackbody was assumed equal to 1. Thirdly, the calibration parameters R and S_0 are correlated because they are the solutions of a system of two equations (Equation 3.3). Therefore, their uncertainties cannot be considered separately, so it is more effective not to include them in the measurement equation. By considering explicitly the reference data (FTIR signals and emissivities) in Equation 3.4, a more reliable expression for the *blacksur* measurement method is obtained:

$$\varepsilon = \frac{\frac{(S_s/a - S_{bb1})\cdot(\varepsilon_{bb1}L_{bb1} - \varepsilon_{bb2}L_{bb2})}{S_{bb1} - S_{bb2}} + \varepsilon_{bb1}L_{bb1} - L_{sur}}{L_s - L_{sur}}. \tag{3.5}$$

This measurement equation can be simplified by defining a ratio quantity Q that includes all optical measurements:

$$Q = \frac{S_s/a - S_{bb1}}{S_{bb1} - S_{bb2}}. \tag{3.6}$$

The ratio parameter Q now includes all signal measurements on one single function. It must be noted that all measured signals S_i are signed functions, which can be positive or negative depending on whether net radiation reaches or leaves the detector. In particular, it is well established that the S_{bb2} contribution is negative at room temperature, as the detector ($T_{det} \sim 313$ K) emits more radiation when aiming at this colder blackbody reference source ($T_{bb2} \sim 293$ K) than the one that it receives from it (González-Fernández et al., 2010). Thus, for sample temperatures and wavelengths for which S_s is comparable in magnitude to the signal emitted by the detector, the influence of the latter may lead to negative S_s values.

The final measurement equation is:

$$\varepsilon = \frac{Q \cdot (\varepsilon_{bb1}L_{bb1} - \varepsilon_{bb2}L_{bb2}) + \varepsilon_{bb1}L_{bb1} - L_{sur}}{L_s - L_{sur}}. \tag{3.7}$$

This equation is similar to the one used by Monte and Hollandt, 2010 and Adibekyan et al., 2015. This formulation allows for separation of the sources of uncertainty into three uncorrelated sets of parameters: signals (Q), temperatures (T_s, T_{sur}, T_{bb1}, T_{bb2}), and reference source emissivities (ε_{bb1}, ε_{bb2}). It should be reminded, however, that there is a correlation between the measured emissivity values at different wavelengths, as they all rely on common

parameters (such as the temperatures). This will be important in the calculation of total emissivities in Section 3.6.

3.4 Sources of uncertainty in spectral measurements

The uncertainty budget of the *blacksur* method implemented in the HAIRL device was first introduced in del Campo et al., 2010 and will be revised in this section, according to the revised Equation 3.7, and the new estimations of uncertainty for the base input magnitudes. It is based on the linearized GUM framework (JCGM, 2008a), considering only first-order uncorrelated terms.[4] A summary of the findings of this Section can be found in Table 3.2, along with the type and probability density function of each source and subsource. Two types of uncertainty components are considered in this framework: Type A stands for components evaluated by statistical methods, whereas Type B stands for components evaluated using other methods (JCGM, 2012). Within the context of this work, Type B uncertainties arise from quotes of either calibration reports or literature data.

Regarding the probability distributions of the data, three cases will be considered. Type A uncertainties are described by a Gaussian distribution, with the standard deviation of the mean of n measurements (JCGM, 2008a):

$$u_G(x) = \frac{s}{\sqrt{n}} = \sqrt{\frac{\sum(x_i - \overline{x})^2}{n(n-1)}}. \tag{3.8}$$

However, Equation 3.8 is only valid in this form in the limit of a large number of measurements ($n \to \infty$), which corresponds to a Gaussian distribution according to the Central Limit Theorem (JCGM, 2008a). This a good approximation for many measurements contained in this work, but not for measurements with few datapoints (e.g., $n \sim 5$). These measurements are described in GUM using Student's t-distribution. The usual procedure consists of quantifying the effective degrees of freedom of the measurement and computing a corrected coverage factor k (JCGM, 2008a). However, it is also possible to define an enlarged standard uncertainty for quantities described by t-distributions by following Section 6.4.9 of JCGM, 2008b and neglecting the calculation of effective degrees of freedom:

[4] As will be noted in Section 3.4.3, reference and sample temperatures can be correlated when measuring radiance temperatures by the Christiansen method. The analysis of such case is out of the scope of this thesis.

TABLE 3.2: Uncertainty sources for emissivity measurements and their respective subsources, along with their types and probability distributions.

Source of uncertainty	Symbol	Type	Distribution
1) Signal ratio	Q		
Sample signal repeatability	S_s	A	Gaussian
High-T blackbody signal repeatability	S_{bb1}	A	Gaussian
Low-T blackbody signal repeatability	S_{bb2}	A	Gaussian
FTIR non-linearity		A	Not significant
Size-of-source effect		B	Not significant
FTIR drift		B	Not significant
Polarization sensitivity		A	Not significant
Optical path difference	a	A	Gaussian
2) Sample surface temperature	T_s		
Metals			
Repeatability and inhomogeneity		A	t-distribution
Thermocouple (K) accuracy		B	Rectangular
Ceramics		B	Rectangular
3) Surroundings temperature	T_{sur}		
Repeatability and inhomogeneity		A	t-distribution
Thermocouple (K) accuracy		B	Rectangular
Emissivity of the surroundings	ε_{sur}	B	Not significant
4) Blackbody reference sources			
High-T blackbody temperature	T_{bb1}		
Repeatability		A	Gaussian
Inhomogeneity		B	Gaussian
Thermocouple (R) accuracy		B	Gaussian
Low-T blackbody temperature	T_{bb2}		
Repeatability		A	Gaussian
Thermocouple (K) accuracy		B	Rectangular
High-T blackbody emissivity	ε_{bb1}	B	Rectangular
Nextel 811-21 emissivity	ε_{bb2}	B	Gaussian

$$u_t(x) = \left(\frac{n-1}{n-3}\right)^{1/2} \frac{s}{\sqrt{n}}. \tag{3.9}$$

Finally, in the case of the Type B uncertainties, the information available often only quotes limit values of the uncertainties, with no usual standard uncertainty value. In these cases, a rectangular (uniform) distribution must be used. In this case, all values within a range $\pm a$ from the mean are equally probable, which leads to the following standard uncertainty (JCGM, 2008a):

$$u_R(x) = \frac{a}{\sqrt{3}}. \tag{3.10}$$

In order to determine the combined standard uncertainty arising from the combination of these sources of uncertainty, the sensitivity factors need to be obtained by partial derivation of Equation 3.7:

$$\frac{\partial \varepsilon}{\partial Q} = \frac{\varepsilon_{bb1} L_{bb1} - \varepsilon_{bb2} L_{bb2}}{L_s - L_{sur}}. \tag{3.11}$$

$$\frac{\partial \varepsilon}{\partial L_s} = \frac{L_{sur} - \varepsilon_{bb1} L_{bb1} - Q \cdot (\varepsilon_{bb1} L_{bb1} - \varepsilon_{bb2} L_{bb2})}{(L_s - L_{sur})^2}. \tag{3.12}$$

$$\frac{\partial \varepsilon}{\partial L_{bb1}} = \frac{\varepsilon_{bb1}(1+Q)}{L_s - L_{sur}}. \tag{3.13}$$

$$\frac{\partial \varepsilon}{\partial L_{bb2}} = -\frac{\varepsilon_{bb2} Q}{L_s - L_{sur}}. \tag{3.14}$$

$$\frac{\partial \varepsilon}{\partial L_{sur}} = \frac{\varepsilon_{bb1} L_{bb1} + Q(\varepsilon_{bb1} L_{bb1} - \varepsilon_{bb2} L_{bb2}) - L_s}{(L_s - L_{sur})^2}. \tag{3.15}$$

$$\frac{\partial \varepsilon}{\partial \varepsilon_{bb1}} = \frac{L_{bb1}(1+Q)}{L_s - L_{sur}}. \tag{3.16}$$

$$\frac{\partial \varepsilon}{\partial \varepsilon_{bb2}} = -\frac{Q L_{bb2}}{L_s - L_{sur}}. \tag{3.17}$$

It should also be borne in mind that, in the case of the L_i radiances, the real uncertainties correspond to the temperature measurements T_i, and so it is necessary to introduce derivatives of Planck's law:

$$\frac{\partial L_i}{\partial T_i} = \frac{2 C_1 C_2 e^{C_2/\lambda T_i}}{\lambda^6 T_i^2 (e^{C_2/\lambda T_i} - 1)^2} = \frac{L_i}{\lambda T_i^2} \frac{C_2 e^{C_2/\lambda T_i}}{(e^{C_2/\lambda T_i} - 1)}. \tag{3.18}$$

Therefore, the final expression for the combined standard uncertainty u_c is:

$$u_c^2(\varepsilon) = \left(\frac{\partial \varepsilon}{\partial Q}\right)^2 u^2(Q) + \sum_{i=1}^{4} \left(\frac{\partial \varepsilon}{\partial L_i}\frac{\partial L_i}{\partial T_i}\right)^2 u^2(T_i) + \sum_{i=1}^{2} \left(\frac{\partial \varepsilon}{\partial \varepsilon_{bbi}}\right)^2 u^2(\varepsilon_{bbi}). \quad (3.19)$$

3.4.1 Signal ratio measurement

Repeatability in the measurement of the FTIR signals is one of the most fundamental uncertainty sources in emissivity measurements, particularly for low-emitting samples or at low temperatures and short wavelengths (where the signal-to-noise ratio is the lowest). Repeatabilities of the three signals (sample and two blackbodies), as well as the uncertainty in the optical path difference a, are evaluated as Type A uncertainties described by uncorrelated Gaussian distributions:

$$u^2(Q) = \sum_{i=1}^{3} \left(\frac{\partial Q}{\partial S_i}\right)^2 u^2(S_i) + \left(\frac{\partial Q}{\partial a}\right)^2 u^2(a). \quad (3.20)$$

The optical path difference factor a is routinely checked, especially during interferometer maintenance procedures, by measuring the radiance emitted by an infrared source located at each side of the optical entrance. The result of the latest calibration and the associated standard uncertainty are shown in Figure 3.2. The standard uncertainty is calculated as a Type A uncertainty for each side of the entrance (sample and blackbody). The uncertainty was larger at both ends of the spectrum due to lower radiances at such wavelengths.

As this calibration procedure needs to be done in air for practical reasons, the resulting spectra shows signs of absorption bands by atmospheric water and CO_2 around 6 and 15 μm. Data around 4 μm have been interpolated to avoid the strongest CO_2 absorption mode. Because of these spectral features, the factor which is used in the calculations has been smoothed by fitting it to a simple functional form, in order not to introduce these spurious spectral bands in the resulting measurements. The equation used is quadratic in wavenumber:

$$a = \frac{S_R}{S_L} = m_1 + \frac{m_2}{\lambda^2}, \quad (3.21)$$

where S_R and S_L stand for the measured calibration signals from the right (sample) and left (blackbody) compartments.

The optical paths followed by both sides of the interferometer diverge increasingly with decreasing wavelength. Such spectral dependence is coherent with the presence of non-ideal surfaces, such as the optical entrance box in our setup (Chamberlain, 1979, Chapter 8). The fitted curve and the standard uncertainty of the measurement are introduced into Equation 3.20. Practical reasons do not allow for very frequent recalibrations of this parameter, but the drift with time is sufficiently slow so as to be negligible in this uncertainty budget.

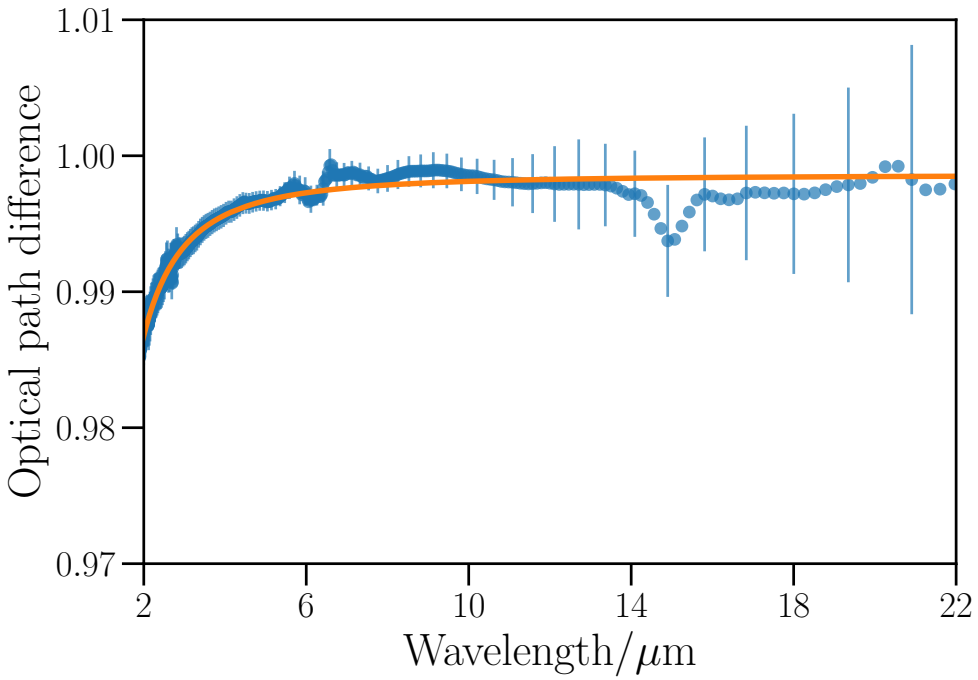

FIGURE 3.2: Experimentally determined optical path difference factor (a) and fitting. Error bars correspond to the standard uncertainty ($k = 1$).

Other sources can contribute to the radiance factor uncertainty. All interferometers are polarization-dependent to a degree, mainly because of the polarization sensitivity of beamsplitters (Shaw, 2002). Mirrors also inflict a non-negligible polarization to radiation reflected at high angles. This can be

a significant concern in the case of the HAIRL instrument, which has an optical entrance with three additional mirrors with 45° angles of incidence. Thus, a possible polarization sensitivity was suspected and needed to be quantified. The ratio of polarized signals of the high-temperature blackbody signal at 1083 K is reported in Figure 3.3. Strong deviations from unity are observed, with the p-polarized radiation being attenuated below 10 μm and the opposite behavior taking place at longer wavelengths. This polarization effect does not influence measurements performed near the normal direction, as the polarized components of the emissivity only split for relatively large emission angles (Figure 2.2). Figure 3.4 shows the effect of polarization in high-angle directional spectral emissivity measurements of mirror-polished Cu at 473 K, where directly measured data are compared to that obtained from the average of s- and $p-$polarized measurements. It can be seen that most angular emissivity measurements up to 70° show little signs of polarized effects for most wavelengths. This point will be studied in more depth in the near future.

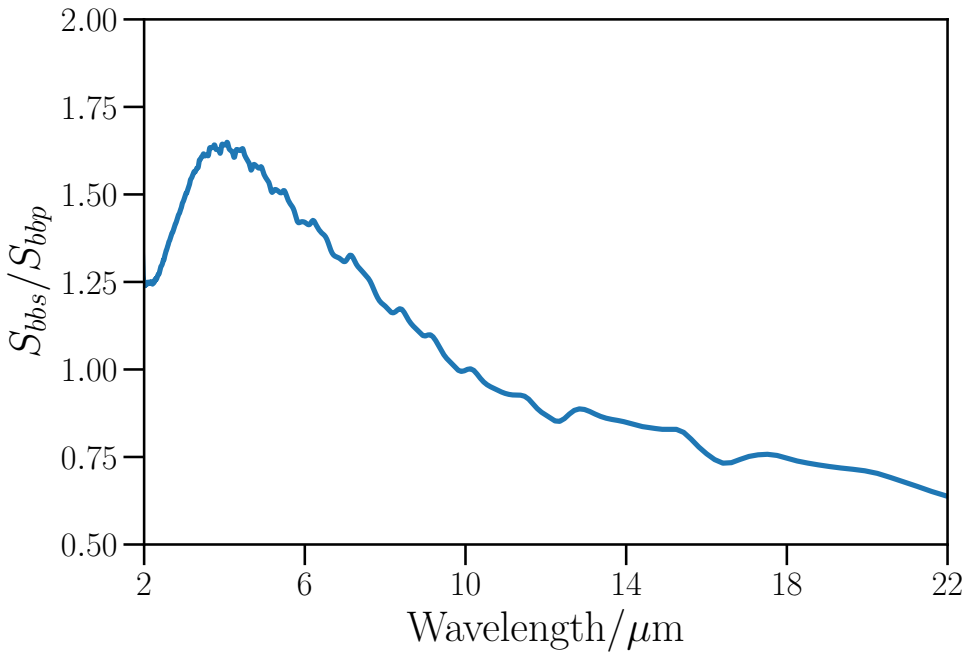

FIGURE 3.3: Ratio of polarized blackbody signal measurements at 1083 K.

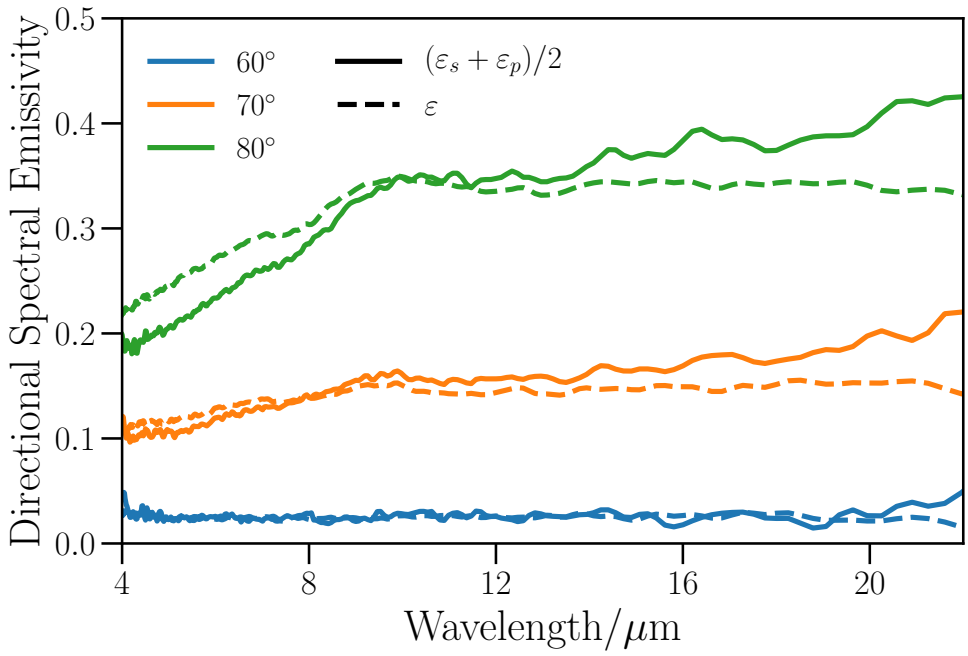

FIGURE 3.4: Comparison of directional spectral emissivity measurements on polished Cu at 473 K performed with a polarizer (continuous lines) and without (dashed lines). Shaded regions correspond to expanded uncertainties ($k = 2$).

Other potential uncertainty sources have also been neglected. Nonlinearity of the FTIR spectrometer with a thermal DLaTGS detector has been checked by a multi-temperature calibration procedure (Zhang et al., 2017) and found to be indistinguisable from the standard uncertainty of the procedure. In the case of the size-of-source effect, the size of the blackbody aperture is $\varnothing 20$ mm and that of the usual samples is greater than $\varnothing 20$ mm, while the sample spot size corresponding to the standard aperture size of $\varnothing 5$ mm is estimated as $\varnothing 3.6$ mm. It has been shown by other researchers that this effect can generally be neglected in emissivity measurements if both radiation sources are much larger than the measuring spot size (Ishii and Ono, 2001; Cárdenas-García, 2014). Finally, interferometer drift is minimized by controlling the room temperature within a 1 K/h and 2 K/day variation range, as required by the manufacturer. Variations in room temperature have

been tested in a previous study, where the only significant drifts in calibration parameters taking place at temperature deviations much larger than the specified ones (González-Fernández et al., 2010). This insensitivity is attributed to the reduced heat transfer taking place inside a vacuum interferometer.

3.4.2 Sample surface temperature measurement (metals)

When considering the standard uncertainty of the temperature measurements in this experimental setting, two cases will be discussed: contact measurements with thermocouples for metals (this Section) and non-contact pyrometric measurements using the Christiansen wavelength for ceramics (Section 3.4.3). The former was first introduced in a different manner in the previous uncertainty budget (del Campo et al., 2010), whereas the latter has not yet been examined in this laboratory.

There are two main sources of uncertainty when measuring temperatures with thermocouples. The first one, of Type A, concerns the temporal and spatial thermal inhomogeneity, as measured directly with the Type K thermocouples. The second source, of Type B, corresponds to the intrinsic accuracy of these sensors.

The first source is estimated based on the readings of two thermocouples located symmetrically across the measuring spot. Start and end temperatures are recorded for each sensor, leading to four temperature datapoints per measurement. Thus, the inhomogeneities may be described by the standard uncertainty associated to Student's t-distribution (Equation 3.9) with $n = 4$. Spatial and temporal inhomogeneities are treated equally, as experience shows them to be correlated.

Regarding the second source, the accuracy of a standard Type K thermocouple is given by the ANSI C96.1 standard as a limit of error of 0.75% of the temperature in °C or 2.2 K, whichever is greater (Nakos, 2004). In the past uncertainty budget published by this group, these values were introduced into the budget as the standard uncertainty of a Gaussian distribution (del Campo et al., 2010). However, the limits of error correspond to the extremes of the allowed uncertainty for a thermocouple conforming to the required composition (Nakos, 2004). Therefore, the standard uncertainty of this measurement does not correspond to these limits, but must be estimated from them. Some authors have considered these limits of error as equivalent to a the 99.7% confidence interval for a Gaussian distribution with a coverage factor of $k = 3$ (Nakos, 2004). In this work, a rectangular distribution function

(Equation 3.10) has been considered to be more appropriate, as recommended by the GUM when only an upper and a lower bound are available (JCGM, 2008a). By assuming this distribution, the standard uncertainty related with this source becomes $1/\sqrt{3}$ of either limit of error, whichever is greater:

$$u(T_{\mathrm{TC}}) = \frac{1}{\sqrt{3}} \cdot \begin{cases} 0.0075(T - 273.15) \\ 2.2\ \mathrm{K} \end{cases} . \tag{3.22}$$

Therefore, the resulting uncertainty is formulated by combining the two sources of uncertainty, assuming that the accuracies of both thermocouples are correlated (as they come from the same batch of material). It is thus given by:

$$u^2(T) = u^2(T_{\mathrm{TC}}) + \left(\frac{n-1}{n-3}\right)\frac{s^2(T_i)}{n}. \tag{3.23}$$

It should be borne in mind that Type K thermocouples are susceptible to several potential sources of systematic errors arising from magnetic short-range ordering, thermal hysteresis and selective oxidation of the Chromel leg (Mangano and Coggiola, 1993). These issues can lead to faulty surface temperature measurements beyond the limits allowed by Equation 3.23. Therefore, an upgrade to Type N thermocouples,[5] with similar but more stable composition and properties, is projected for the near future to avoid these potential systematic errors.

As a final note, the equivalence of both methods for mounting thermocouples mentioned in Section 3.2 has been tested for an ARMCO iron sample in an Ar atmosphere for the usual stabilization time (20 minutes). The differences between the intrinsic welded and intrinsic pressed methods can be seen in Figure 3.5. Both curves agree within less than the standard uncertainty for most temperatures, with the temperature values of the pressed method remaining consistently below those corresponding to the welded case. Nevertheless, no clear evolution of this systematic error can be seen with increasing temperature. Furthermore, the magnitude of this effect is expected to be reduced in vacuum due to the absence of convection effects. The presence of a systematic error arises from an imperfect thermal contact in the mechanically pressed method. Both methods should lead to the same temperatures in the infinite-time limit (Keltner and Beck, 1983), but the stabilization time of thermocouples increases with less optimal thermal contact. As this error is

[5] Composition of the legs: Ni-14.2Cr-1.4Si vs. Ni-4.4Si-0.1Mg (mass%).

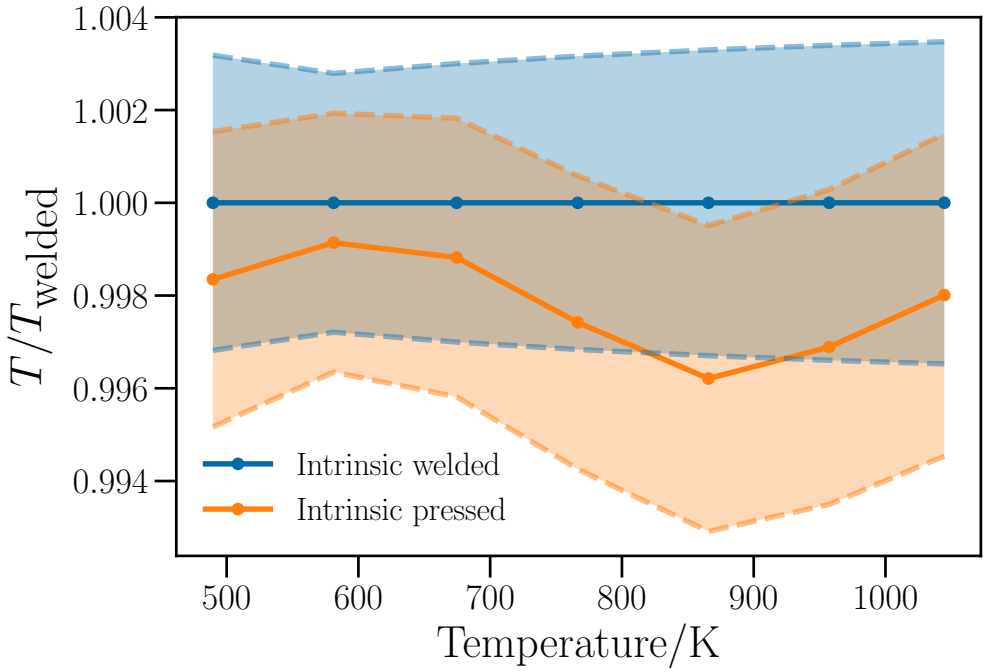

FIGURE 3.5: Study of the systematic error in temperature measurement of an ARMCO iron disk in Ar by thermocouples drilled and pressed into the sample, compared to those spot-welded onto the surface. Shaded areas and lines correspond to relative standard uncertainties ($k = 1$).

is difficult to estimate for each material and application, it is not considered in the final uncertainty budget. It should be noted that uncertainties arising from these thermocouple mounting errors have been considered as the main source of uncertainty in high-temperature transient measurements (Nakos, 2004). Thus, this point will be further explored in future studies concerning higher temperatures (1273 K or beyond).

3.4.3 Sample surface temperature measurement (ceramics)

Temperature measurements in ceramic materials are difficult to accomplish with contact temperature sensors because of their low thermal and electrical conductivities. Therefore, a non-contact temperature measurement

method is desired, although the effect of the emissivity complicates this procedures. Fortunately, some ionic compounds have a well-defined wavelength at which the emissivity is close to 1 and is only very weakly dependent on temperature (as seen in Figure 2.4). This wavelength is known as the Christiansen point and has been used as a reliable method for measuring the surface temperatures of heteropolar ceramic materials (Rousseau et al., 2005). Temperature measurements using the Christiansen wavelength are very useful because they are performed at the same time as the sample radiance measurements and largely avoid systematic errors due to thermal gradients, since the temperature is directly measured on the measuring spot itself. However, no widely recognized estimation of its uncertainty is available at the moment.

An error of 10 K in the determination of the melting point of single-crystal α-Al_2O_3 has been determined in a similar setup during emissivity measurements, which allows an estimation of $u(T_{Chris}) \sim 0.5\%$ at very high temperatures above 2000 K (De Sousa Meneses et al., 2015). Similar relative uncertainties have been reported as extremal values for FTIR-based temperature measurements (Dufour, Rowell, and Steele, 1998), as well as in comparisons between the Christiansen wavelength method and a more complete one based on thermal flux balances and knowledge of the thermophysical properties of polycrystalline α-Al_2O_3 (Zhang et al., 2018a). It should be noted that model-based temperature measurement methods can in fact be less accurate than radiometric ones under certain circumstances, as they strongly depend on the accuracy of numerous input parameters (Hanssen et al., 2007).Therefore, the relative standard uncertainty in the sample surface temperature associated with the Christiansen method is evaluated in this work as a Type B uncertainty modelled by a rectangular distribution with an upper bound of 0.5%.

It should be noted that the assumption of uncorrelated temperatures may not hold in the case of the Christiansen method, as this radiant temperature measurement is correlated with the temperatures of the blackbodies. In this uncertainty budget, this influence has been neglected and a more conservative approach has been followed, but this topic remains to be explored in the future. Nevertheless, the Christiansen wavelength is revealed as an alternative to more complex measurement methods, with the added advantage of measuring the local temperature of the central spot, without effects introduced by radial gradients. Comparisons to more complex thermal-flux based methods have not been performed in this laboratory because the heating system does not allow a straightforward heat conduction modelling.

3.4.4 Surroundings temperature measurement

The treatment of the uncertainties arising from the chamber walls emission is similar to that of the sample temperature. It is treated as a room-temperature blackbody source ($\varepsilon = 1$), with its temperature measured by Type K thermocouples in two spots in the chamber walls which are symmetric with respect to the optical path of the measurement. As the temperature is less than 300 K (due to the water cooling system), the standard uncertainty of the thermocouples (Equation 3.22) is taken as $2.2/\sqrt{3}$ K. The inhomogeneity of the enclosure temperature is calculated as that of the sample temperature; i.e., as a Type A uncertainty corresponding to measurements of two thermocouples at two different times. Student's t-distribution for small number of observations is again formulated, resulting in the same expression as Equation 3.23.

Due to the use of a water cooling system, the average enclosure temperature is $\simeq 285$ K, instead of 298 K (the value assumed in del Campo et al., 2010). The effect of the reduction in enclosure temperature is negligible for high sample temperatures, but makes precise measurements possible below 330 K. This is due to the fact that the greatest limitation of the *blacksur* method is that the emissivity diverges when the temperature of the sample and the surroundings are very close (see the denominator in Equation 3.4). Finally, another possible source of uncertainty for this radiance is the assumption that the sample surroundings behave as a blackbody, whereas the emissivity of the coating employed has been measured to be closer to 0.97 (Adibekyan et al., 2017). However, it has been proved that the *blacksur* method differs less than 0.05% from the most accurate method (multi-reflections) when the emissivity of the chamber walls is greater than 0.95, provided that the sample chamber area is much larger than the spot size (Pérez-Sáez, Campo, and Tello, 2008). We therefore neglect the influence of this source of uncertainty.

3.4.5 Blackbody reference sources

The measurement method requires radiance measurements of a high-temperature blackbody and a room-temperature Nextel 811-21 coating. The uncertainty of the measured signals has already been taken into account in the calculation of the Q ratio. The emissivities of the sources are $\varepsilon_{bb1} > 0.995$ for the conventional blackbody source (as specified by the manufacturer), and a spectral average of $\varepsilon_{bb2} = 0.97$ (with a standard uncertainty of 0.01) for the Nextel 811-21 coating, as calculated from literature data (Adibekyan et al.,

2017). Not having any additional information on the uncertainty of the emissivity of the high-temperature blackbody, we consider only the uncertainty given by the calibration certificate (issued by the manufacturer and traceable to metrological-level calibrations performed at the National Physical Laboratory in the UK), modelled as a rectangular probability density function (PDF) with limits $0.995 < \varepsilon_{bb1} < 1$. Both uncertainties were neglected in the previous uncertainty budget (del Campo et al., 2010), but will be considered in this updated version. In the case of the temperatures of the reference sources, their standard uncertainties arise from the accuracy of the sensors and, in the case of the high-temperature blackbody source, a 0.3 K inhomogeneity in the aperture temperature distribution. The sensor accuracies are 1 K (calibration certificate: expanded uncertainty of 2 K, $k = 2$) for the high-temperature blackbody (measured with a Type R thermocouple), and $2.2/\sqrt{3}$ K for the low-temperature blackbody (Type K thermocouple, Equation 3.22).

Finally, it should be noted that all two-temperature methods are susceptible of systematic errors. As noted in Section 3.3.1, two-temperature methods have been claimed to incur in significant errors in the determination of the internal radiation sources due to small errors in the reference signal measurements, which can be crucial for certain measurements with low signals (Zhang et al., 2017). However, in the case of this instrument, its calibration accuracy has been checked to be satisfactory provided that one of the sources remains close to room temperature and the other one is heated up to a temperature at least 800 K higher to minimize the uncertainty (González-Fernández et al., 2010). This contrasts with the approach followed by other authors, who choose blackbody references which have the most similar radiation temperature to the sample (Adibekyan et al., 2015). In both cases, two-temperature methods are considered to be suitable given a linear detector, such as DLaTGS, and sufficiently good control of the blackbody temperatures and the spectrometer drift, which in this setup is controlled by monitoring the temperature of the room, and was found to have significant influence only in extreme cases (González-Fernández et al., 2010)

3.5 Application to representative materials

3.5.1 Combined standard uncertainty of Ni and sapphire

The uncertainty budget described above for spectral emissivity measurements is applied in this subsection to two materials, a metal and a ceramic.

Nickel was chosen as the metallic example based on previous positive experience with this material (González de Arrieta et al., 2019). A sputtering target synthesized using the Mond process with a diameter of 50 mm and a thickness of 3.2 mm was used. Its nominal purity was $> 99.99\%$, with 15 ppm Fe and 10 ppm S as the main impurities (mass%). It was mechanically polished with Al_2O_3 powder and its surface roughness parameters were measured with a mechanical profilometer (Mitutoyo SJ-201) as $R_a = 0.03$ μm, $R_q = 0.04$ μm, and $R_z = 0.16$ μm. Its spectral emissivity is shown in Figure 3.6a as a function of temperature. The wavelength and temperature dependences of the uncertainties can be more easily appreciated as relative uncertainties in Figure 3.6b. It can be seen that the uncertainty is very large at 473 K for all wavelengths, and quickly drops with temperature. Regarding its wavelength dependence, it tends to increase with wavelength for all temperatures, except at the shortest wavelengths and lowest temperatures, where it can also reach large values. It is interesting to note that the previous uncertainty budget reported generally greater uncertainties at shorter rather than larger wavelengths (del Campo et al., 2010).

In the case of ceramic materials, a 0.43 mm-thick single crystal of Al_2O_3 has been chosen. It is oriented perpendicular to the c optical axis with a 0.2° misorientation angle. It was epi-polished on one side to a roughness of $R_a < 0.3$ nm. It was synthesized by the Czochralski method, with a purity of $> 99.99\%$. The temperature was measured assuming an emissivity of 1 at the Christiansen wavelength, as checked using specular reflectance measurements ($\varepsilon(\lambda_{Chris}) = 0.999 \pm 0.001$). Due to its semi-transparency at shorter wavelengths, it was measured using a low-emissivity iron substrate in order to reduce the spurious radiation from the highly-emitting heating wire in the back. A method for compensating this effect is described in Jeon et al., 2010:

$$\varepsilon^* = \varepsilon + \tau\varepsilon_{sub} + \varepsilon(1-\varepsilon_{sub})\tau \implies \varepsilon = \frac{\varepsilon^* - \tau\varepsilon_{sub}}{1+(1-\varepsilon_{sub})\tau}, \tag{3.24}$$

where ε^* is the apparent emissivity without semitransparency corrections, τ is the normal-normal transmittance of the sample, and ε_{sub} is the normal emissivity of the substrate.

Thus, two additional sources need to be included in the uncertainty calculations and all partial derivatives evaluated in Section 3.4 need to be weighted by an additional factor of $(1+(1-\varepsilon_{sub})\tau)^{-1}$. The transmittance is evaluated as a Type B uncertainty from extreme values taken from literature data (Lee et al., 2011), whereas the emissivity of the ARMCO iron substrate and

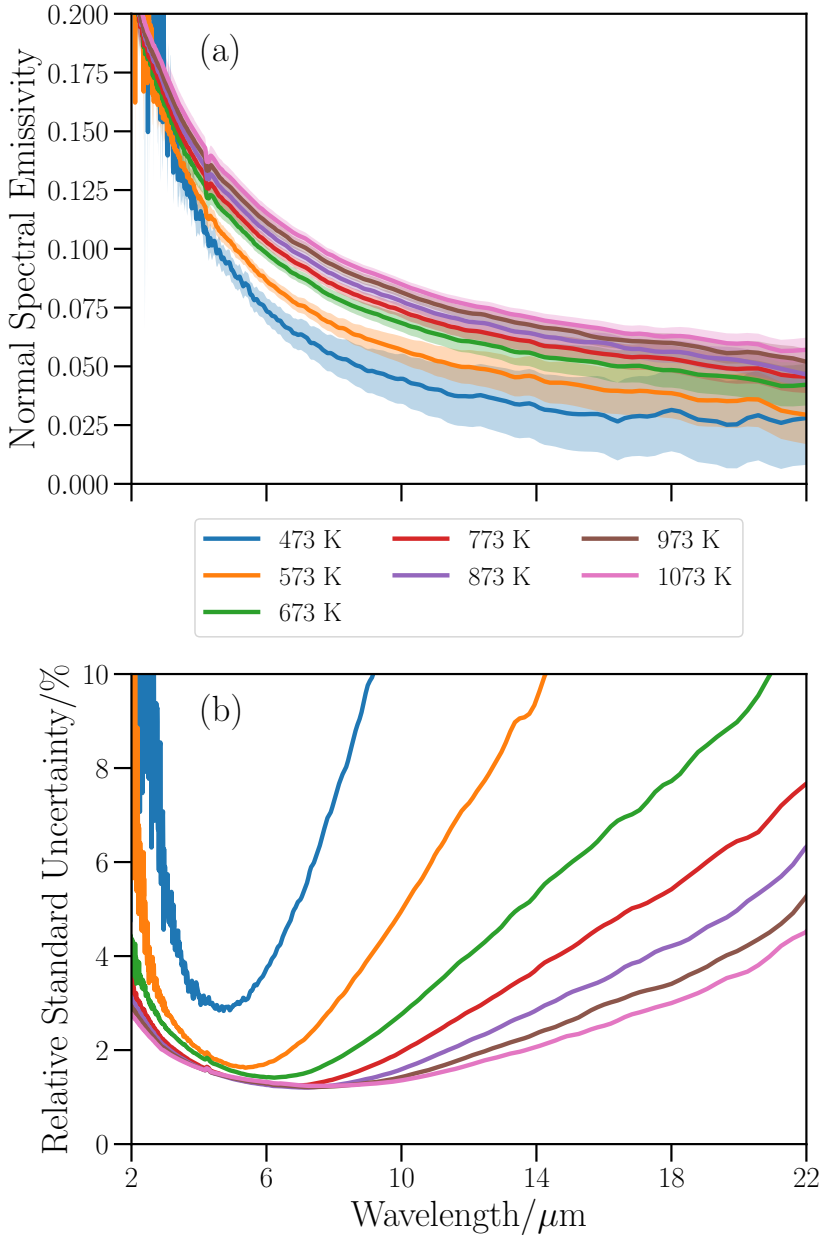

FIGURE 3.6: (a) Normal spectral emissivity of Ni as a function of temperature. Shaded regions correspond to expanded uncertainties ($k = 2$). (b) Relative standard uncertainties ($k = 1$) of the normal spectral emissivity measurements of Ni.

its combined standard uncertainty have been evaluated using independently measured data.

The emissivity measurements of sapphire and their relative standard uncertainties can be seen in Figure 3.7. It is clear that the relative uncertainties at higher temperatures are much lower than those of nickel, mainly due to the higher emissivity values (except in the semi-transparent range below 7 μm). This shows that, for most of the mid-infrared range, the lowest relative standard uncertainties achievable using the HAIRL device are around 1%. Nevertheless, the relative uncertainty at low temperatures is significant, particularly in the low-emissivity regions at long wavelengths. These results on sapphire demonstrate the capability of the apparatus to measure the emissivity of ceramic materials, as well as to deal accurate emissivity values at relatively low temperatures, even for low emissivity values below 0.2. Full implementation of the method suggested in Jeon et al., 2010 (the two-substrate method) would reduce significantly the uncertainty due to the transmittance of the material, which needed to be modelled in this case.

As can be seen in Figure 3.7b, the relative standard uncertainty for ceramic materials is low for most wavelengths. This stems from the greater signal-to-noise ratio of these high-emissivity spectral regions, as well as the reduced contamination from low-temperature radiances (surroundings, detector). Nevertheless, these measurements could be performed down to 373 K, almost 200 K less than the lowest temperature considered in the previous uncertainty budget (del Campo et al., 2010). Emissivity measurements at such low temperatures are easier for high-emitting ceramics than for metals. Even lower temperatures could be explored if the temperature of the vacuum chamber and the sample are sufficiently different. This is the main drawback of the *blacksur* method, which has a divergence in the denominator (Equation 3.4) when those two temperatures become equal (Pérez-Sáez, Campo, and Tello, 2008).

Finally, the relative contributions of each uncertainty source for both materials to the variance (u_c^2 from Equation 3.19) are shown in Figures 3.8 and 3.9. Examples of numerical uncertainty budgets at particular wavelengths and temperatures are also shown in Tables 3.3 and 3.4. Some commonalities in the relative weights of the sources can be appreciated. For example, for both materials there is a general increase with temperature of the relative importance of the uncertainties corresponding to the sample temperature (T_s) and the high-temperature source temperature and emissivity uncertainties (T_{bb1}, ε_{bb1}), whereas those corresponding to the low-temperature source (T_{bb2}, ε_{bb2})

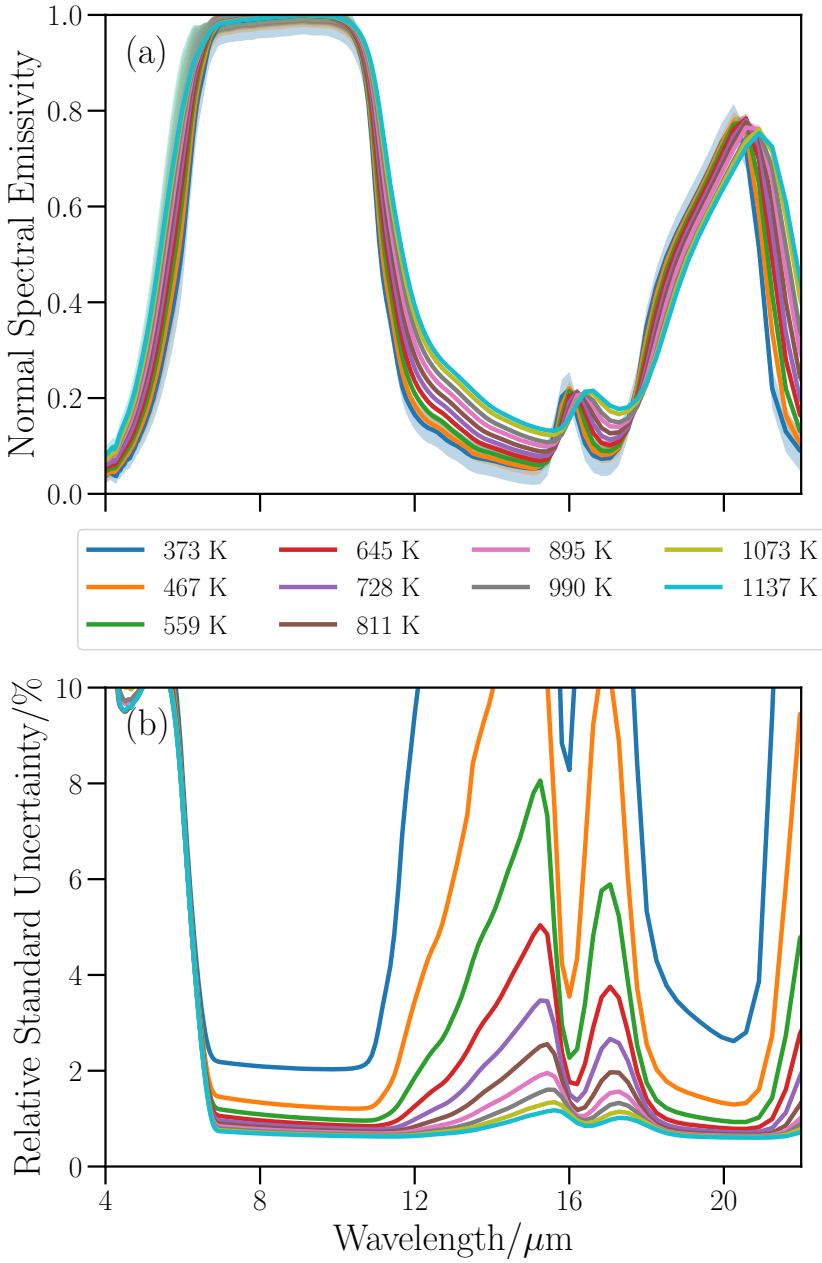

FIGURE 3.7: (a) Normal spectral emissivity of sapphire (single-crystal Al_2O_3) as a function of temperature. Shaded regions correspond to expanded uncertainties ($k = 2$). (b) Relative standard uncertainties ($k = 1$) of the normal spectral emissivity measurements of sapphire Al_2O_3.

and the surroundings temperature (T_{sur}) decrease. This is expected, as these latter sources of uncertainty correspond to low-temperature radiance sources, the influence of which is greatly reduced when the emission from the sample is increased at higher temperatures. Nevertheless, some influence of them can still be observed at long wavelengths for the highest temperatures, especially for Ni.

Some differences in the relative weights for each material can also be distinguished. The weight corresponding to the radiance uncertainty (Q) is greater for Ni, due to the low signal reaching the detector from this low-emissivity sample. This contribution becomes important at higher temperatures (where most of the others are significantly reduced), or at short wavelengths and low temperatures (where the emitted radiation has a very low signal-to-noise ratio). On the contrary, this uncertainty is larger for sapphire at longer wavelengths. Finally, in the case of semi-transparent regions, the uncertainty due to the transmittance (τ) is the dominant term, with the one corresponding to the emissivity of the substrate (ε_{sub}) being almost negligible in comparison. Overall, these Figures show similar trends as the ones shown for the previous uncertainty budget (del Campo et al., 2010), but with more accurate results and a more extensive review of uncertainty sourcess.

TABLE 3.3: Uncertainty budget for Ni at 673 K and 5 μm.

Source of uncertainty	Type	Value (%)
Sample signal repeatability	A	0.07
High-T blackbody signal repeatability	A	0.08
Low-T blackbody signal repeatability	A	2.24
Optical path anisotropy	A	0.08
Sample temperature		0.27
Surroundings temperature		0.43
High-T blackbody temperature		0.10
Low-T blackbody temperature		0.44
High-T blackbody emissivity	B	0.29
Nextel 811-21 emissivity	B	1.03
Relative combined standard uncertainty		1.55
Relative expanded uncertainty ($k = 2$)		3.10

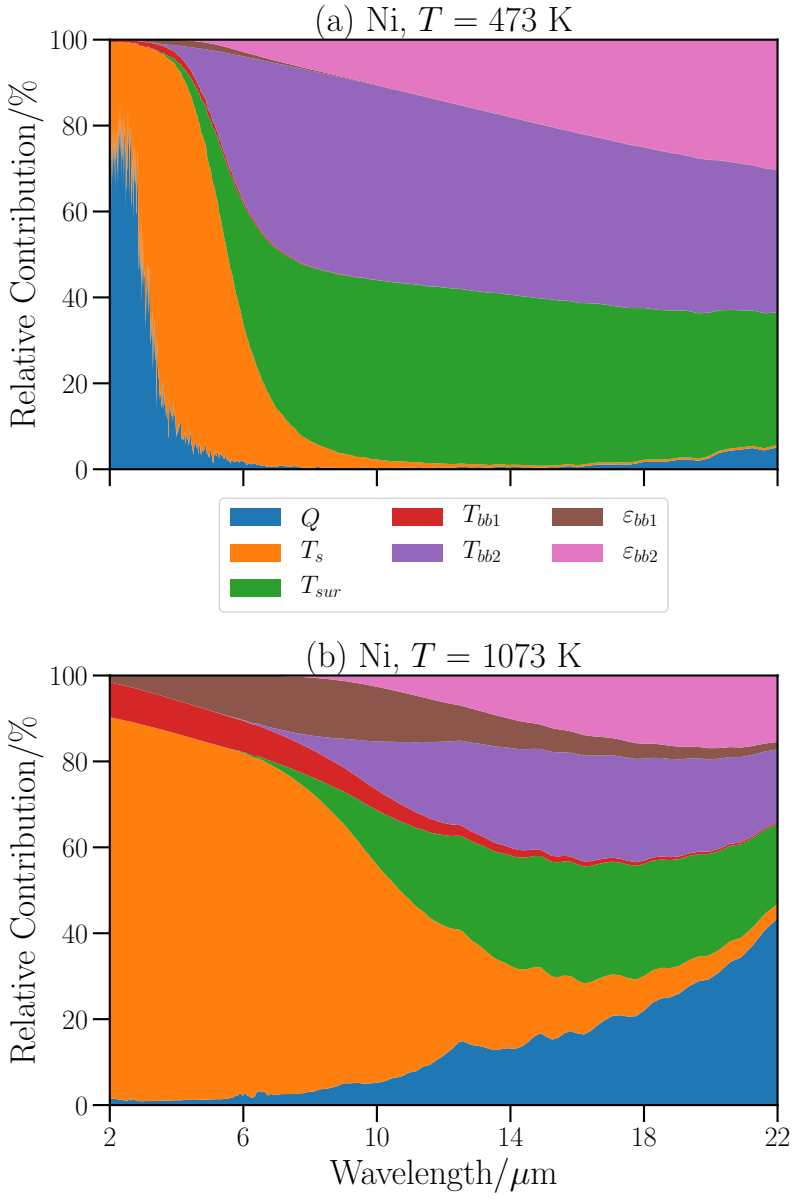

FIGURE 3.8: Relative contribution of each term of Equation 3.19 to the total variance for Ni at the lowest (a) and highest (b) temperatures measured.

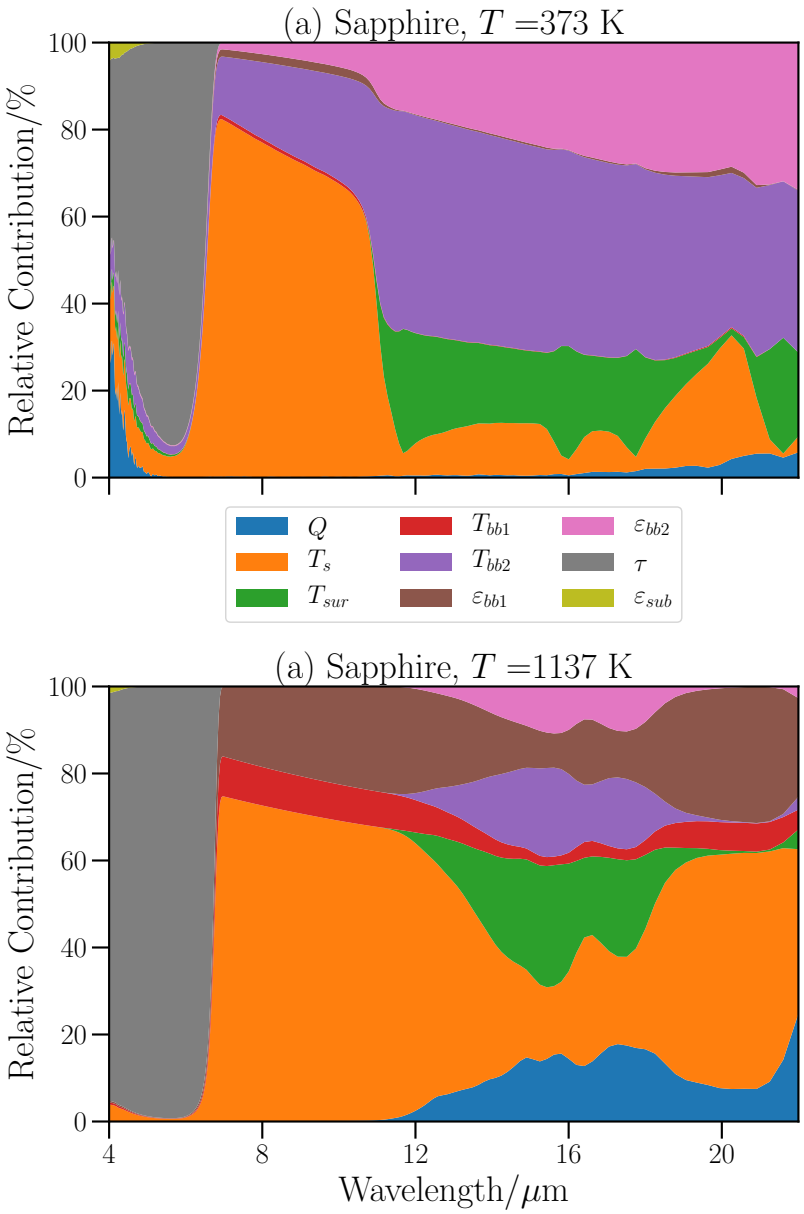

FIGURE 3.9: Relative contribution of each term of Equation 3.19 to the total variance for sapphire in the $4 - 22$ μm range at the lowest (a) and highest (b) temperatures measured.

TABLE 3.4: Uncertainty budget for α-Al_2O_3 at 373 K and 8 μm.

Source of uncertainty	Type	Value (%)
Sample signal repeatability	A	0.36
High-T blackbody signal repeatability	A	0.08
Low-T blackbody signal repeatability	A	0.40
Optical path anisotropy	A	0.10
Sample temperature (Christiansen)		0.29
Surroundings temperature		0.43
High-T blackbody temperature		0.10
Low-T blackbody temperature		0.44
High-T blackbody emissivity	B	0.29
Nextel 811-21 emissivity	B	1.03
Relative combined standard uncertainty		2.09
Relative expanded uncertainty ($k = 2$)		4.18

3.5.2 Comparison with literature data

Comparison of the obtained results to those of other laboratories is an essential step in validating any measurement method. Three steps have been undertaken in this Section in order to check the validity of the applied methods and the calculated uncertainties. Firstly, a comparison of the Ni measurements to literature data is shown in Figure 3.10. Secondly, the accuracy of the measurement method for sapphire is evaluated in Figure 3.11 by comparison to a similar method for measurement of semi-transparent materials (Lee et al., 2011). Finally, preliminary results of a collaboration with the Physikalisch-Technische Bundesanstalt (PTB) are shown in Figure 3.12 for polished Cu.

In terms of its radiative properties, nickel is one of the most studied pure metals. This stems from its abundance, corrosion resistance, and relatively high melting point. An additional advantage over titanium and iron is that it features no structural phase transition at high temperatures, whereas iron experiences large grain growth and irreversible surface roughening in the austenite phase (Makino et al., 1980). Some partial reviews of available data can be found in Teodorescu, 2007 and Howell, Mengüç, and Siegel, 2010. Thus, this material is an ideal candidate for a comparison with literature results. Some data in the $300 - 1100$ K range are shown in Figure 3.10, together

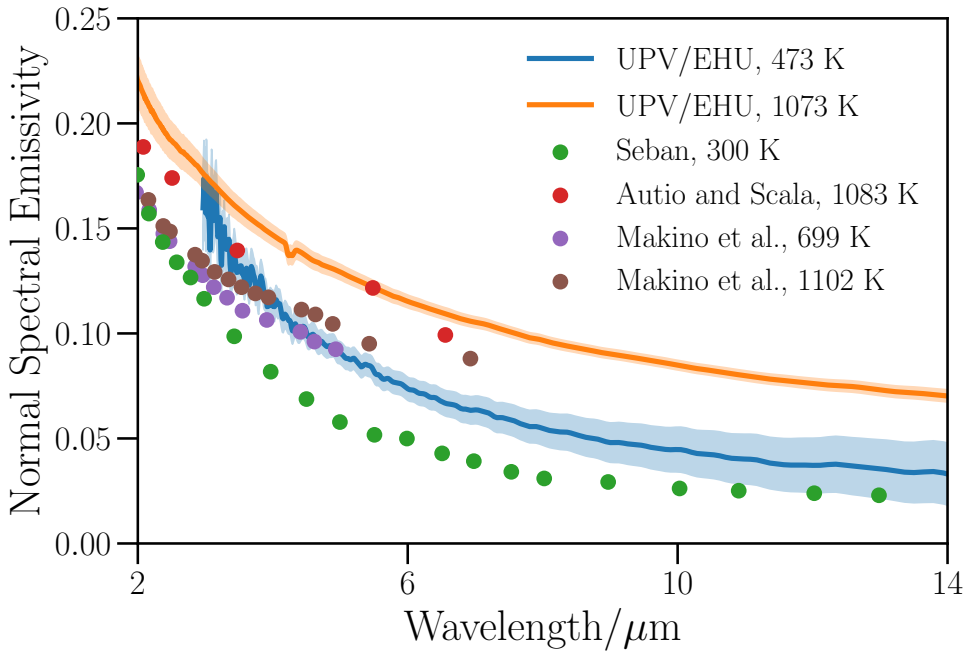

FIGURE 3.10: Comparison of measured emissivity values of Ni to literature data (Seban, 1965; Autio and Scala, 1966; Makino, Kawasaki, and Kunitomo, 1982). Shaded regions correspond to expanded uncertainties ($k = 2$).

with the results reported in this work at the lowest and highest temperatures. Overall, the six data sets feature a similar spectral tendency, with the HAIRL measurements sitting within the range of reasonable values, although the short-wavelength values lie on the high side when compared to the values reported in Makino, Kawasaki, and Kunitomo, 1982. The origin of the discrepancy does not seem to originate from the instrument, but the sample itself. This hypothesis is supported by the significant spread of values in the literature, evidenced in the comparisons made by Teodorescu, 2007 and Howell, Mengüç, and Siegel, 2010. As this sample was subsequently oxidized to study the evolution of emissivity with oxide layer thickness (González de Arrieta et al., 2019), no subsequent analysis of the surface could be made for a more in-depth study. Further efforts with fresh samples are scheduled to try to determine recommended values for the use of this metal as a candidate

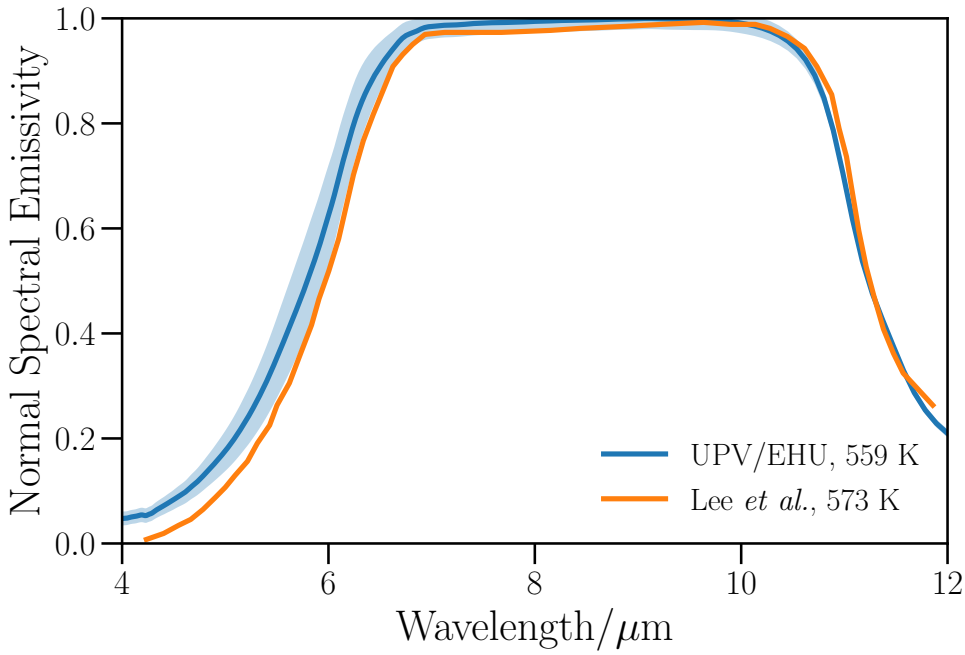

FIGURE 3.11: Normal spectral emittance of sapphire Al_2O_3 at 559 K, compared to literature data at 573 K (Lee et al., 2011). Shaded regions correspond to expanded uncertainties ($k = 2$).

reference material for emissivity measurements in vacuum.

Secondly, a comparison to sapphire literature data from Lee et al., 2011 has been made in Figure 3.11. Both measurement methods employ back-heating systems, and as such the emission from the substrate has to be compensated. There is quantitative agreement between the curves in certain wavelength ranges, although some discrepancies may be noted. In particular, the short-wavelength limit of the data measured with the HAIRL emissometer is higher than the one reported in the reference. This corresponds to the fully transparent region of this material, and so the emissivity should tend to zero in both cases. A possible explanation may be due to a mismatch between the temperatures of the sample and the substrate, as the heat-transfer calculation behind Equation 3.24 implicitly assumes an isothermal multi-layer system. Thermal gradients inside the sample itself must also be considered.

Finally, the accuracy of this setup has also checked in a comparison with

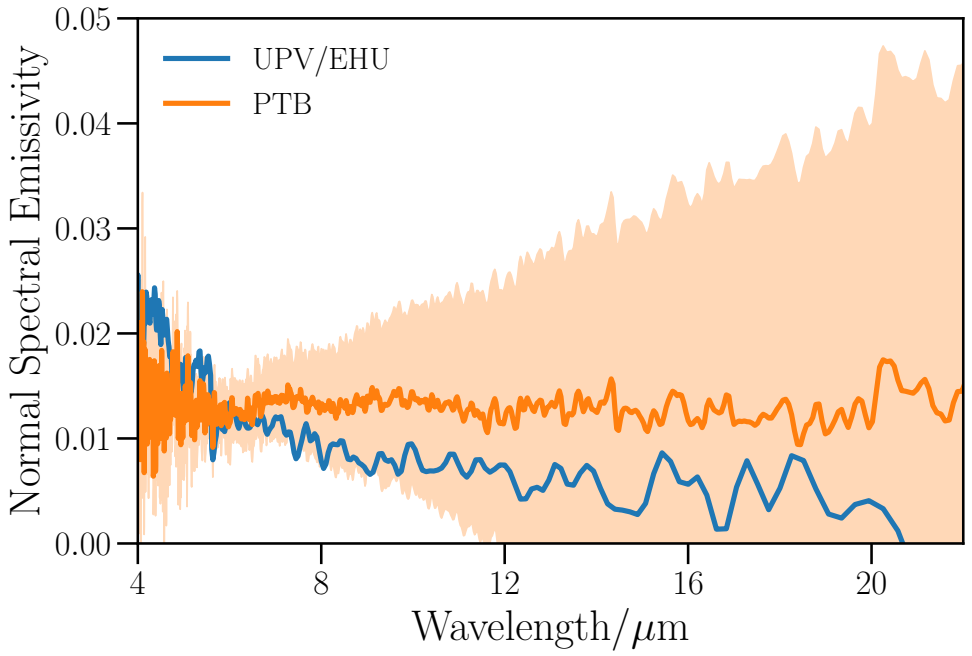

FIGURE 3.12: Comparison of normal emissivity values of two polished Cu samples at 473 K at UPV/EHU and PTB. Shaded regions correspond to expanded uncertainties ($k = 2$).

PTB Berlin. Normal spectral emissivity measurements on two different samples of polished Cu at 473 K are shown in Figure 3.12, where a good agreement can be seen between both curves. Further work with this material is being carried out at the moment.

3.6 Calculation and propagation of uncertainties for integrated quantities

3.6.1 Integration of spectral data

The sections above have dealt with measurements of the spectral directional emissivity. This parameter depends not only on temperature, but also

on wavelength and emission angle; whereas, for most heat transfer applications, details on such dependences are often irrelevant. It is for this reason that integrated quantities, such as the total normal or total hemispherical emissivities (Equations 2.8 and 2.9), are often more useful for engineering applications. The procedure introduced in this Section for the calculation of these integrated magnitudes is similar to the one followed by other authors for calculation based on radiometric methods (Adibekyan et al., 2015; Balat-Pichelin et al., 2017), and has been validated as a viable alternative to the conventional calorimetric methods to calculate the total hemispherical emissivity (Monchau et al., 2018). Radiometric methods rely on a more complex approach to the calculation of this property, but they can be measured in the same instrument as the spectral emissivity, which constitutes a great practical advantage.

A common problem of radiometric methods is the difficulty of measuring the entire spectral range in which thermal radiation may be emitted (i.e., from the far-infrared to the visible range). A method for calculating the total normal emissivity of metallic materials from directional spectral measurements in a restricted spectral range was introduced in Setién-Fernández et al., 2013. This method involved calculating the total normal emissivity through a numerical integration of the available spectral data and two possible extrapolations, an overestimation and an underestimation (Figure 3.13). Therefore, the best estimate was found to be the average of the values obtained using each of the two extrapolation procedures, with the expanded uncertainty being half the difference between them. Based on the general knowledge that the wavelength dependence of the emissivity of metals is monotonically decreasing throughout the infrared range (Howell, Mengüç, and Siegel, 2010), this extrapolation procedures assumes that the possible values are contained within the last measured data point at each end and the physical limit of the emissivity (either 0 or 1). This method approaches the correct value of the total emissivity given a sufficiently wide spectral range without requiring actual information of the emissivity in the extrapolated region. This can be regarded as an application of the principle of maximum entropy, as described in the GUM (JCGM, 2008a).

The maximum-entropy probability distribution for extrapolations of the spectral emissivity to the full electromagnetic spectrum when the available data is restricted to a spectral range $[\lambda_1, \lambda_2]$, and the emissivity is known to be monotonically decreasing with wavelength, is given by:

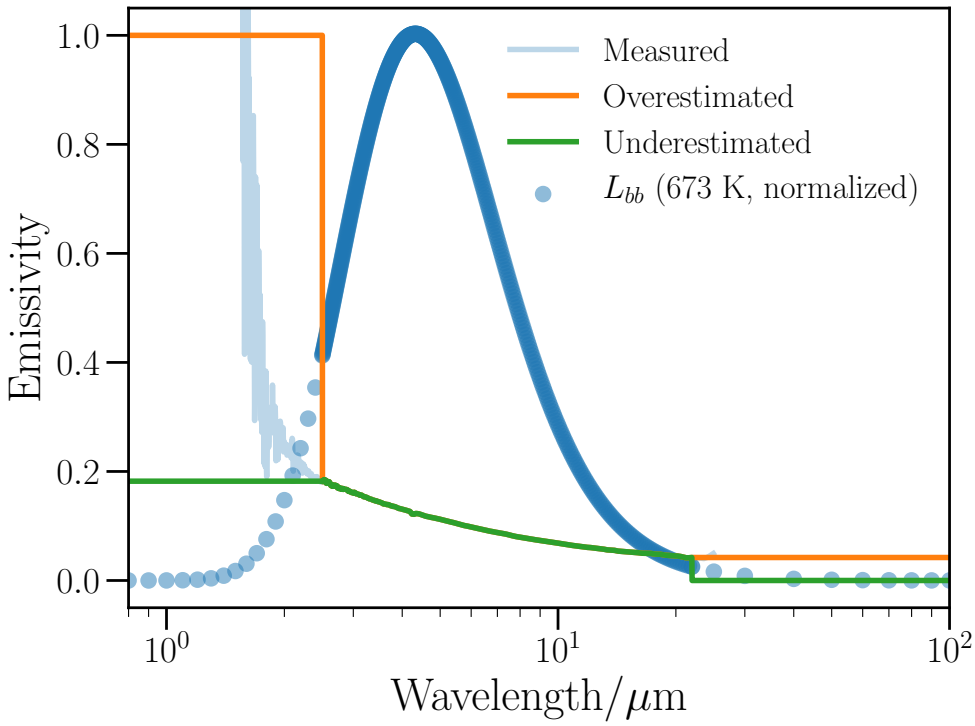

FIGURE 3.13: Graphic representation of the extrapolation procedure for Ni using normal spectral data from Fig 3.6. Emissivity curves are shown as solid lines, corresponding to measured data (shaded blue), the overestimated limits (solid orange) and the underestimated ones (solid green). A normalized blackbody radiation spectrum (blue dots) is shown to illustrate the relative weight of each spectral region.

$$\varepsilon_T(T) = \frac{\pi}{\sigma T^4}\left[\int_0^{\lambda_1} \varepsilon_1 L(\lambda)d\lambda + \int_{\lambda_1}^{\lambda_2} \varepsilon(\lambda)L(\lambda)d\lambda + \int_{\lambda_2}^{\infty} \varepsilon_2 L(\lambda)d\lambda\right], \quad (3.25)$$

where ε_i are random variables described by uniform probability density functions (PDFs) for each side of the spectrum. In the particular case of metals, this becomes:

$$f(\varepsilon_i) = \begin{cases} U(\varepsilon_{max}, 1) \text{ for } \varepsilon_1 \\ U(0, \varepsilon_{min}) \text{ for } \varepsilon_2 \end{cases}, \quad (3.26)$$

where $U(a, b)$ stands for the uniform distribution.

The final equation then becomes:

$$\varepsilon_T(T) = \varepsilon_1 F_{0\to\lambda_1}(T) + \varepsilon_2 F_{\lambda_2\to\infty}(T) + \frac{\pi}{\sigma T^4}\int_{\lambda_1}^{\lambda_2} \varepsilon(\lambda)L(\lambda)d\lambda, \quad (3.27)$$

where ε_1 and ε_2 are uniform PDFs given by Equation 3.26, λ_1 and λ_2 are the shortest and the longest wavelength of the experimental spectral interval, and $F_{a\to b}(T)$ stands for the fraction of the total radiance emitted by a blackbody in the $a-b$ wavelength range at temperature T. This function has been computed by numerical integration of the expressions found in Howell, Mengüç, and Siegel, 2010. An illustration of this method is shown in Figure 3.13 for normal spectral data of Ni at 673 K.

Equation 3.25 and Equation 3.27 are based on the least-informative PDF given the only information that the emissivity in the chosen material is monotonic (as recommended by GUM in the case of insufficient information). This is guaranteed in the particular case of metals due to the Drude law (Equation 2.34) being qualitatively valid for most wavelengths up to the visible range (Howell, Mengüç, and Siegel, 2010), but can be easily generalizable to any material with a known monotonic emissivity. Other types of extrapolations, such as assuming a constant emissivity value, have been used for the same purpose (Monchau et al., 2018). It must be noted that the approach followed in this work is conservative and might lead to larger uncertainty values, and other extrapolation procedures are possible for each case. In any case, since the weight of the Planck function decreases exponentially away from the maximum, the assumptions used in the extrapolation procedure are

only required to hold for the spectral range in which the Planck function is non-negligible.

In the case of angular integration to obtain the total hemispherical emissivity (Equation 2.9), the extrapolations are much simpler. The emissivity values at the extremes are given by the electromagnetic theory as $\varepsilon(0°) \simeq \varepsilon(10°)$ and $\varepsilon(90°) = 0$ (Howell, Mengüç, and Siegel, 2010). This makes the calculation of the total hemispherical emissivity a simple generalization of the total normal one and with an uncertainty almost equal to those of the individual total directional emissivities.

3.6.2 Propagation of uncertainties by a Monte Carlo method

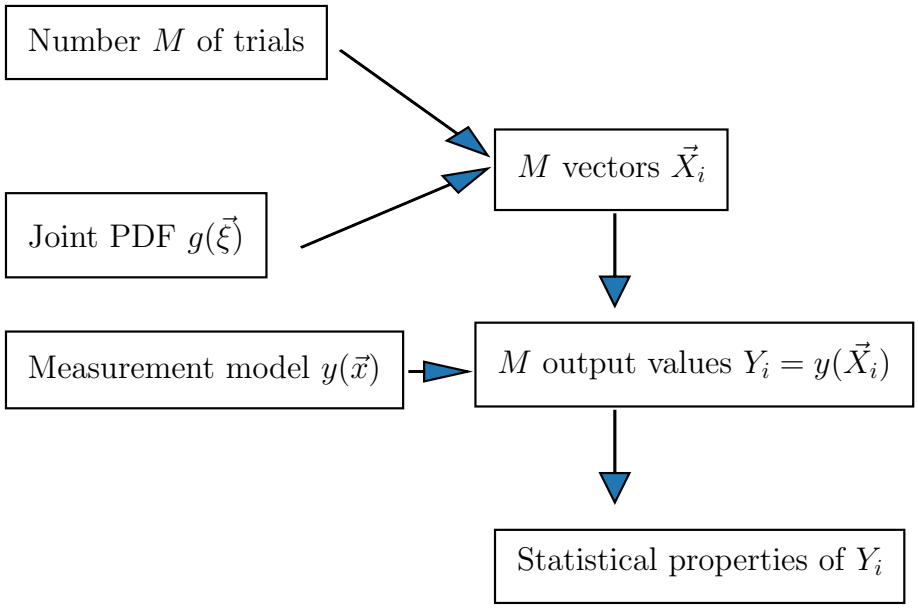

FIGURE 3.14: Schematic diagram of the main steps of the propagation of uncertainties using a Monte Carlo method.

The complexity of Equation 3.27 makes the standard approach of propagation of uncertainties from spectral to total data difficult, due to the presence of numerical integration and non-linear functions. Therefore, the standard

linearized approach to calculate the uncertainties is discouraged by the Supplement 1 to the GUM (JCGM, 2008b), which instead recommends performing numerical uncertainty propagations using Monte Carlo methods. Monte Carlo algorithms rely on pseudo-random number generators to perform numerical samplings of functions without any analytical calculations. They are thus very applicable in uncertainty calculations, given that the input parameters already have well-defined probability density functions (PDFs, Table 3.2). Those methods work by sampling M vectors of random input data $\vec{X}_i$ generated using the known joint PDF $g(\vec{\xi})$ (with $\vec{\xi}$ being the vector of parameters), computing each resulting values Y_i from the measurement model $y(\vec{x})$, and then calculating their statistical properties, as shown in Figure 3.14.

A Monte Carlo method has been applied in this work following the guidelines of the JCGM, 2008b. The propagation of uncertainties using Monte Carlo methods is common for complex models involving numerical integrals in the field of radiometry (Esward et al., 2007; Cordero et al., 2007). This approach is more general and less biased than the conventional method because it propagates the entire distribution functions describing each of the variables. The Monte Carlo method of propagation of uncertainties requires defining the input PDFs for each of the variables that feature in Equation 3.27 (ε_1, ε_2, and each of the $\varepsilon(\lambda_i)$ datapoints). In this approach, the uncertainty in the measured sample surface temperature is not considered as an input in the calculation, but as an external parameter. The extrapolated emissivities are defined as rectangular PDFs (following Equation 3.26), whereas the discrete spectral emissivity data points are drawn from a multivariate Gaussian distribution and assumed to be perfectly correlated ($r = 1$). Quantification of the actual correlation is complicated, but assuming a perfect correlation gives the highest possible uncertainty, whereas assuming no correlation gives an unrealistically low uncertainty value. Therefore, $r = 1$ for all $\varepsilon(\lambda_i)$ is regarded as a conservative but realistic estimate. This approach is similar to that followed by Monte and Hollandt, 2010 for the same type of calculation, but without a Monte Carlo approach. They calculated the difference between the maximum possible value within the standard uncertainty and the best estimate of the total emissivity, and assigned it as the standard uncertainty of this parameter. That estimation relied implicitly on an assumption of perfect correlation between all data points, as is done explicitly here. In any case, a Monte Carlo analysis is deemed more robust because of the complexity of Equation 3.27.

A Monte Carlo method has been implemented in serial mode in Python 3.7. Standard functions from the NumPy (v1.16.4) and SciPy (v1.3.0) libraries

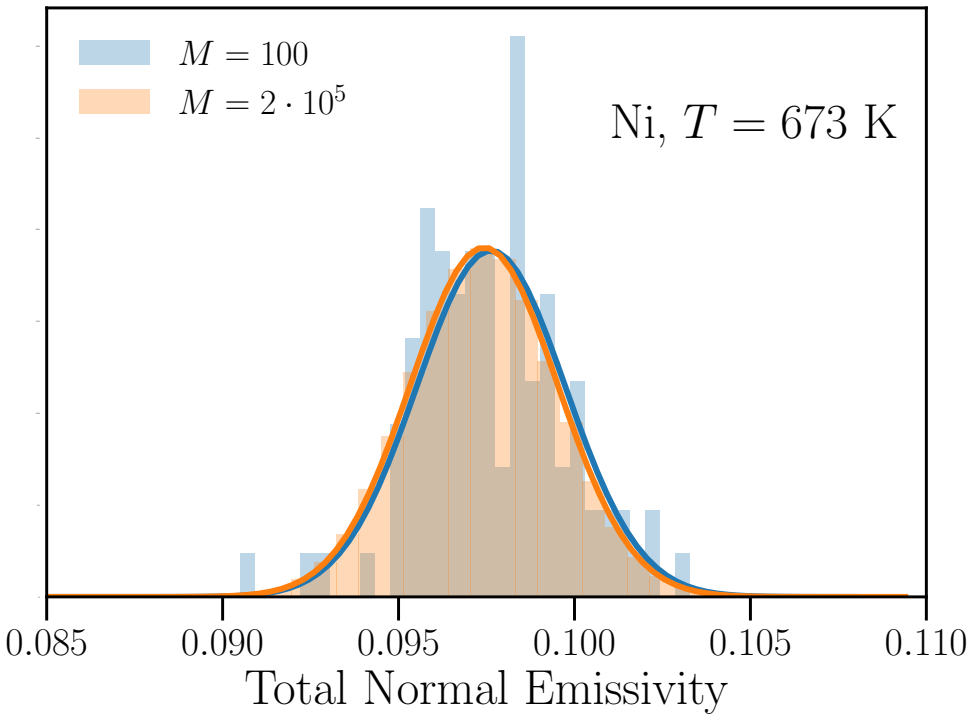

FIGURE 3.15: Calculation of the total normal emissivity of Ni at 673 K and propagation of its uncertainty by a Monte Carlo method using two different numbers of trials ($M = 100$ and $M = 2 \cdot 10^5$). Solid lines correspond to Gaussian fittings to the histograms.

TABLE 3.5: Uncertainty sources for the calculation of the total emissivities and their distributions.

Source	Symbol	Distribution
Measured emissivities	$\varepsilon(\lambda_i)$	Multivariate Gaussian ($r = 1$)
Extrapolated emissivities	$\varepsilon_1, \varepsilon_2$	Rectangular

have been used. The pseudo-random generator used has been the standard Mersenne Twister `MT19937` algorithm (Matsumoto and Nishimura, 1998). Two different sets of pseudo-random numbers with $M = 100$ and $M = 2 \cdot 10^5$ trials have been calculated from an initialization state (seed) created using a hardware-based random number generator (Linux's `/dev/random` method). This guarantees obtaining a sufficiently random starting seed so that the common pitfalls of the Mersenne Twister for low-entropy seeds (e.g., 0) are avoided. Different seed values have also been tried to check the independence of the results from biases caused by bad initialization states. The latter number of trials has been selected as appropriate for a 95% confidence interval (coverage factor $k = 2$), according to the recommendations of JCGM, 2008b, whereas the former has been used as a check to verify that the statistical properties of the result are stable and do not evolve significantly with the number of trials.

The resulting PDFs from the calculations are shown in Figure 3.15 for one temperature, together with Gaussian fittings to the data. It can be seen that both means and standard deviations agree satisfactorily, even though the histograms are very different. The results of these calculations for all temperatures are shown in Figure 3.16. Literature data from Makino, Kawasaki, and Kunitomo, 1982, calculated from spectral measurements performed with a similar radiometric method, are shown for comparison. No uncertainties are reported for these measurements, so a proper comparison cannot be made. Nevertheless, a clear offset between both data sets can be observed, even if they show very similar temperature dependences and compare rather favourably in a semi-quantitative manner. This offset correlates with the observed differences between spectral measurements reviewed in Figure 3.10, where the results reported in this work show higher emissivity values in the short-wavelength spectral range. Further work needs to be done to clarify this point and advance on the development of reliable metallic reference materials. Finally, two additional comments can be made about the results. Firstly, the temperature dependence of the total normal emissivity uncertainty is

not monotonic, with the uncertainty at the highest temperatures being larger than those of the medium temperatures. This can be explained because of the larger amount of thermal radiation being emitted at shorter wavelengths, which have to be estimated by extrapolation with a larger uncertainty. Secondly, the temperature dependence of the total normal emissivity shows a change of slope around the Curie temperature ($\sim$ 627 K), where the material ceases to be ferromagnetic (González de Arrieta et al., 2019).

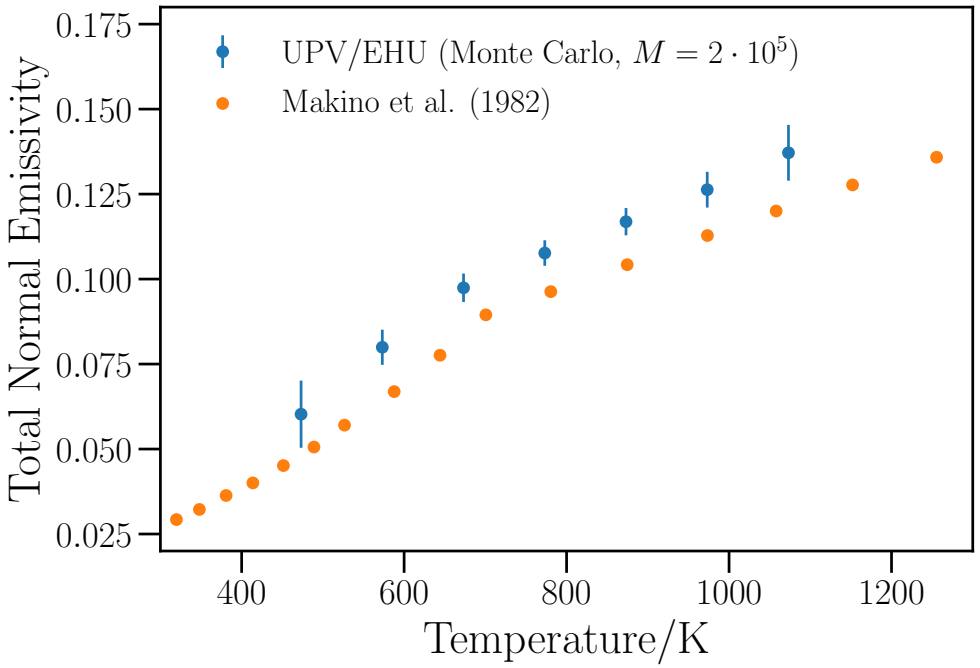

FIGURE 3.16: Total normal emissivity and its standard uncertainty ($k = 2$) of Ni calculated using the Monte Carlo method for $M = 2 \cdot 10^5$. Literature data from Makino, Kawasaki, and Kunitomo, 1982 are shown for comparison.

Finally, in order to illustrate this approach also for the integration of directional data, results corresponding to V-4Cr-4Ti alloys have been used. These alloys are regarded as candidate structural materials for nuclear fusion reactors, and their thermal radiative properties will be discussed in more detail in Chapter 5. Directional spectral data are integrated to yield the total directional emissivities and the total hemispherical one. Figure 3.17 shows the total

directional emissivities with their uncertainties and the calculated total hemispherical emissivity at 673 K. A multivariate Gaussian distribution with complete correlation ($r = 1$) has been assumed again as a conservative estimate. This assumption leads to an absolute uncertainty of the total hemispherical emissivity which is only marginally larger than those of each total directional measurement. This has also been observed in other radiometric methods for the determination of the total hemispherical emissivity from numerical integration of directional data (Adibekyan et al., 2015).

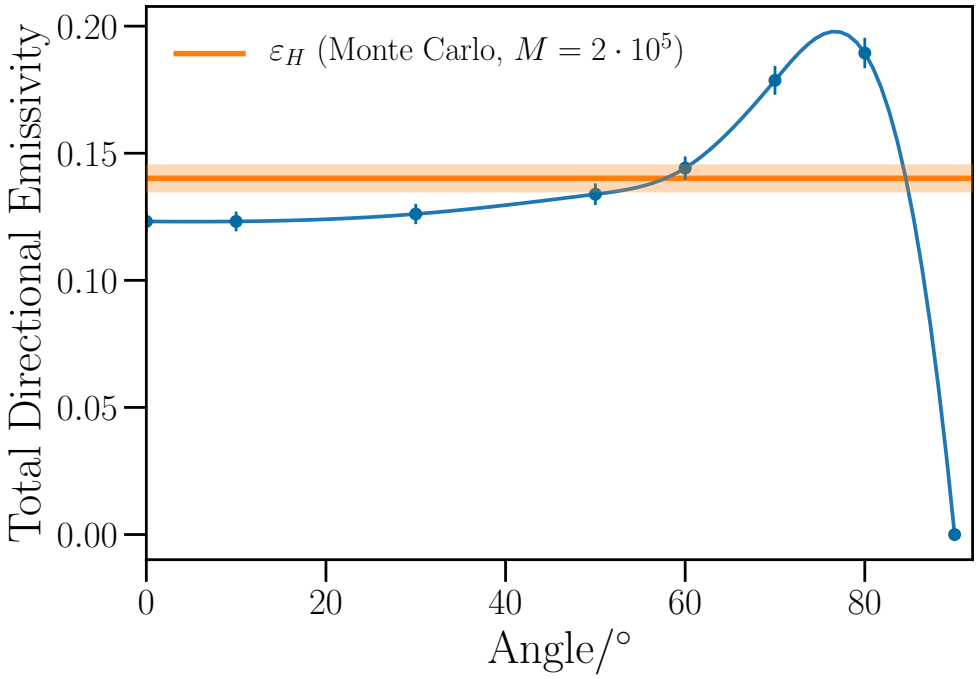

FIGURE 3.17: Total directional emissivities and combined expanded uncertainties ($k = 2$) of a V-4Cr-4Ti alloy at 673 K (blue dots), and total hemispherical emissivity computed using a Monte Carlo method (orange line). The solid blue line is a calculated spline which is used for the integration of the data.

3.7 Conclusions

This Chapter contains an overview of the emissivity measurement equipment and procedures with the HAIRL emissometer of the UPV/EHU, as well as an in-depth update of a significant number of experimental and methodological improvements. Aside from the more technical instrumental upgrades, more profound modifications have been applied to the measurement equation, with the inclusion of more parameters and its reformulation to avoid correlation between the calibration parameters, and to a renewed uncertainty budget for the spectral data, following the GUM guidelines. Moreover, the experimental method has been broadened to include ceramic materials. Finally, an integration and extrapolation procedure for calculation of total emissivities, and their uncertainty calculations using a Monte Carlo method, are also reported. This framework has been preliminarily validated in comparisons to other laboratories for both metallic and ceramic materials.

Chapter 4

Characterization of absorber coatings for solar thermal energy

4.1 Introduction

Solar thermal energy is an alternative power source that takes advantage of the thermal power of solar radiation to heat up fluids which can either provide domestic heating ($T < 473$ K) or electricity ($T > 473$ K). Its high-temperature version, known as concentrated solar power (CSP), provides high-quality heat to turbines for electricity generation. The biggest advantage of this energy source is that, because of its thermal nature, it can be easily coupled to cost-effective thermal energy storage systems and delivered outside the peak solar hours (Pelay et al., 2017). Thus, it can be considered a complementary source to the more widely deployed solar photovoltaic energy, which can only provide electricity during peak solar hours due to the difficulty of large-scale electricity storing. Thus, CSP can act as a base-load power source to balance out peaks in supply and demand of other renewable energy sources with more intermittent output (Chu and Majumdar, 2012). Because of this, several countries with great solar potential (Figure 4.1[1]) have been investing in this technology as a complementary source to photovoltaic. These countries include the most notable cases of Spain and the USA, but also other countries with strategic solar resources, such as Chile or South Africa (*Concentrating Solar Power Projects*).

[1]Map obtained from the "Global Solar Atlas 2.0, a free, web-based application is developed and operated by the company Solargis s.r.o. on behalf of the World Bank Group, utilizing Solargis data, with funding provided by the Energy Sector Management Assistance Program (ESMAP). For additional information: `https://globalsolaratlas.info`

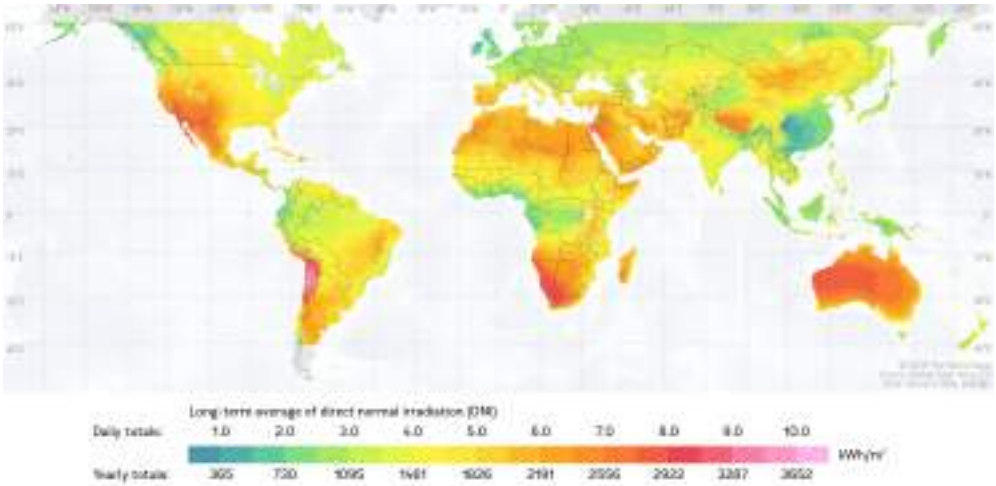

FIGURE 4.1: Global distribution of direct normal solar irradiation in kWh/m^2. Reproduced from Global Solar Atlas 2.0 under the CC BY 4.0 license.

The biggest obstacle to the wide deployment of CSP plants is their high cost compared to other renewable energy sources. The prerequisite for reducing it to a competitive level is to improve the thermal (Carnot) efficiency of the plants; thus, higher operating temperatures are needed (Chu and Majumdar, 2012). Among the main solar thermal configurations, parabolic solar troughs ($T \sim 673$ K) are still by far the most widely deployed. However, solar tower power is increasingly being considered as a more efficient alternative, mainly due to the higher temperatures that it can achieve (873 K and beyond). At these conditions, radiative heat transfer becomes increasingly dominant, and so the development of thermally stable solar-absorbing materials with optimal thermal radiative properties becomes crucial. Thus, the chief challenge faced by these technologies can be formulated as the necessity of increasing their temperatures of operation without incurring in additional heat losses that scale with the fourth power of the temperature (Equation 2.6). A review of the fundamentals of this power source, including discussions on architectures, absorber materials, thermal engines, thermal storage systems, and efficiencies, can be found in Weinstein et al., 2015.

One possible strategy for optimizing the heat balance of CSP plants is the use of selective coatings. A spectrally selective coating is a material with a high solar absorptance α_S and a low total hemispherical emittance ε_H for an

efficient conversion of solar radiation without excessive heat losses (Dan et al., 2017).[2] As the emission of thermal radiation is the only unavoidable heat loss, the competition between absorbed and radiated energies constitutes the essential energy balance of any solar thermal application (Weinstein et al., 2015). A conventional metric is the selectivity ratio between absorptance and emittance, with a common goal being a selectivity of $\alpha_S/\varepsilon_H = 0.95/0.05$, a value which is not always viable. This is because of the interplay between the solar-to-thermal efficiency η_S for a solar concentration factor C:

$$\eta_S = \alpha_S - \frac{\varepsilon_H \sigma T^4}{C E_{\text{AM1.5}}} \simeq \alpha_S - \frac{\varepsilon_H \sigma T^4}{1000 C}, \tag{4.1}$$

and the thermal-to-electricity (or simply thermal) efficiency η_t, described here using the more accurate Chambadal-Novikov expression instead of the more common ideal Carnot efficiency (Novikov, 1958):

$$\eta_t = 1 - \sqrt{\frac{T_0}{T}}, \tag{4.2}$$

where the receiver temperature T acts as the hot reservoir and the environment temperature T_0 as the cold one.

The ideal total efficiency of the CSP plant is then given by the product of these two factors, as all other losses can be theoretically avoided (Weinstein et al., 2015):

$$\eta = \eta_S \cdot \eta_t. \tag{4.3}$$

Thus, if temperatures increase because of the need to maximize Equation 4.2, the range of heat-resistant materials with sufficiently low emittances to offset the radiative losses in Equation 4.1 is reduced. This is the main contradiction driving forward research on solar selective coatings.

Several types of selective coatings have been developed, from intrinsic absorbers to cermets (metal-dielectric composite materials) to multilayers to nano-textured materials. This plethora of solar absorber types has motivated a large number of reviews (Kennedy, 2002; Selvakumar and Barshilia, 2012;

[2] The thermal radiative properties of the materials studied in this Chapter will be described using the *-ance* suffix, as they are multi-layer materials with thickness-dependent properties.

Dan et al., 2017; Xu et al., 2019). One promising category involves the deposition of multilayer coatings where the metallic character (i.e., complex refractive index magnitude $|N|$) decreases progressively from substrate to surface (Dan et al., 2018b). Solar absorption is obtained in these materials by trapping light through inter-layer reflections and thickness tuning to induce interferential destruction of the waves, whereas the low emittance requirements are met using a metallic substrate with low intrinsic emissivity. Many multilayer architecture types with diverse compositions and properties have been researched over the years, with metals of groups 4 to 6 (e.g., Ti, Hf, W) forming the basis of many of them (Dan et al., 2017). Typical examples of these materials are coatings based on Ti-Al-Si oxocarbonitrides, where the metallic character of each successive layer is tuned by setting the ratios of these six elements (Barshilia, 2014; Rebouta et al., 2012; Du et al., 2013; Soum-Glaude et al., 2017; Bilokur et al., 2019; Jyothi et al., 2017).

For typical concentration factors $C \sim 80$ in parabolic solar troughs (Weinstein et al., 2015), the $\sigma T^4/CE$ ratio in Equation 4.1 is not low enough to prevent significant thermal radiative losses unless the emittance ε_H is very low. This is especially true if the temperature is to be further increased, due to the T^4 law. In order to ensure that these optimal radiative properties are maintained at such temperatures, efforts need to be made to accurately characterize the temperature-dependent emittance of these coatings, which are often studied only at room temperature. Setién-Fernández et al., 2013 introduced a direct radiometric characterization of a Mo-SiO_2 cermet coating at the entire working temperature range ($423-873$ K). A further study by Echániz et al., 2015 on a coating with similar composition (Mo-Si_3N_4) from 523 to 873 K showed room-temperature characterizations of thermal radiative properties to be inaccurate if the thermal radiative properties show even small temperature dependences. It is interesting that the temperature dependences of the coatings in both studies differ significantly, despite their similar compositions. The accuracy of extrapolated room-temperature characterizations cannot be known a priori, as some studies find an acceptable agreement between both methods (Bartelmeß et al., 2014; Jyothi et al., 2017), whereas others report significant inaccuracies (Mercatelli, Meucci, and Sani, 2015). This reveals the importance of good emittance characterization of solar selective coatings, especially considering that most published data concerns only the phenomenon of normal emission.

However, all selective coatings face significant issues at temperatures higher than $\sim$ 773 K, as inter-layer diffusion and oxidation of metallic elements activate at such temperatures. Therefore, these materials are unsuitable for central tower applications, which operate in air at temperatures higher than 873 K. Because of the much higher concentration factors allowed by solar tower architectures ($C \sim 1000$ suns), the relative weight of the absorptance in Equation 4.1 is much higher than that of the emittance (Ho and Pacheco, 2014). Thus, maximizing the absorptance is of greater importance compared to the case of parabolic troughs, where the most important issue is the optimization of the selectivity. Therefore, strategies shift from minimizing radiative losses through the use of metallic mirror layers to simpler and more robust materials based on high-absorbing, but also high-emitting, oxide materials. In particular, methods such as the manufacturing of porous structures may become promising alternatives for maximizing light-trapping and absorptance, in order to improve the overall efficiency in a cost-effective manner (Kim et al., 2016; Moon et al., 2014; Sani et al., 2016).

Currently, the most widely adopted solar absorber coating for central tower plants is a commercial black paint known as Pyromark 2500 (hereafter referred to as Pyromark). This paint is easy to deposit in large quantities and shows good solar absorptance, but it is susceptible to aging at high temperatures, which significantly reduces its solar-to-thermal conversion efficiency over time (Boubault et al., 2017). In order to fulfill the ambitious goal set by the SunShot Initiative of increasing the working fluid temperature to 993 K detailed in their 2017 Roadmap, the next-generation solar absorbers for central tower plants must be stable at temperatures around 1073 K (Mehos et al., 2017). This motivates the development of alternatives to Pyromark based on more stable oxide-based materials, such as materials of the spinel group $A^{2+}B_2^{3+}O_4^{2-}$ (Kim et al., 2016; Rubin, Chen, and Chen, 2019; Karas et al., 2018). These materials have been widely characterized in the literature and offer improved thermal and optical capabilities, together with an easily scalable fabrication process by spray-coating.

Accurate characterization of the thermal radiative properties of solar absorber coatings is one of the key requirements for their successful application. However, direct emittance measurements in high-emittance paints can become a challenging task due to a combination of factors related to the temperature measurements of the sample surface, as well as possible thermal gradients due to their low thermal conductivity and high emittance (Honnerová et al., 2014; Honnerová, Martan, and Honner, 2017). Furthermore,

the emissivities of coatings may be affected by extrinsic factors such as non-homogeneous microstructures and surfaces, differences in curing processes or aging effects, which make comparisons between experimental results difficult, even for samples of the same material. These factors help to explain the discrepancies among the reported values of the emittance of Pyromark in the literature (Boubault et al., 2017; Fang et al., 2018; Höser, Wallimann, and Rohr, 2016; Ho et al., 2014; Suo-Anttila, Nakos, and Gill, 2004; Coventry and Burge, 2017). Therefore, a systematic review and characterization of the range of variability and the effect of extrinsic parameters of these materials is key for their application. Moreover, directional emittance data and reliable uncertainties are often lacking in the literature concerning this type of materials (Adibekyan et al., 2017).

This Chapter presents emittance characterization results of two sets of absorber coatings, each one meant for a different application, temperature range, and environment. Directional spectral emittance measurements at the desired operating temperatures of selective absorbers based on W/WAlN/WAlON/Al_2O_3 multilayers and copper-alloyed black spinels ($Cu_{0.5}Cr_{1.1}Mn_{1.4}$ O_4, $CuCr_2O_4$, $CuFeMnO_4$) have been performed. W-based multilayer selective coatings with graded metallic structure feature an excellent room-temperature selectivity of 0.958/0.08. This architecture was chosen for several reasons. Firstly, W is an effective heat mirror, with a large infrared reflectivity and high melting point, which was found to be a promising way to reduce the emissivity of stainless steel (Sibin, John, and Barshilia, 2015). Therefore, the use of W-based dielectric materials as the solar absorbing layers was an obvious choice. Secondly, in the case of the WAlN, WAlON, and Al_2O_3 layers, they offer an easy path to create graded refractive index structures combining the W sputtering target with only one other metallic sputtering target, corresponding to a widely available element (Dan et al., 2016; Dan et al., 2018b). The stoichiometry and metallic character of each layer are thus fixed by the atmosphere inside the sputtering chamber at the time of each deposition. In the case of the black coatings, a new set of solar-absorbing layers based on aggregated Cu-alloyed spinel nanoparticles has been studied. These new materials feature solar absorptance values comparable to (or even higher than) Pyromark while, at the same time, their crystal structure leads to improved high-temperature stability and long-term durability (Rubin, Chen, and Chen, 2019). The main goal of this Chapter is to provide the first accurate and in-depth study of the optical properties of these materials in the infrared, in connection to their solar conversion efficiencies in real applications.

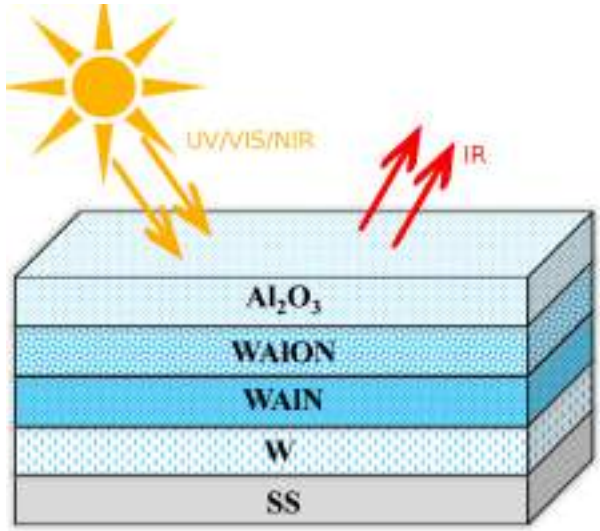

FIGURE 4.2: Schematic representation of the main components of the selective coating.

4.2 Materials and methods

4.2.1 Synthesis of selective coatings

Two W/WAlN/WAlON/Al_2O_3 (hereafter referred to as WWWA) solar selective coatings, shown schematically in Figure 4.2, were deposited on stainless steel (SS) substrates by DC and RF magnetron sputtering using W, Al and Al_2O_3 targets of high purity ($> 99.9\%$). W, WAlN, and WAlON layers were deposited using DC sputtering, whereas the final Al_2O_3 layer was deposited using the RF mode. The SS substrates were mechanically polished using emery paper, followed by diamond nanoparticle suspension. The deposition chamber was evacuated to a base pressure of $8.0 \cdot 10^{-4}$ Pa by means of rotary and turbomolecular pumps. W, WAlN, WAlON and Al_2O_3 layers were deposited successively in Ar, Ar+N_2, Ar+N_2+O_2 and Ar+O_2 environments. The depositions were carried out at a substrate temperature of 573 K. A number of parameters, such as target power, reactive gas flow, and deposition time were tailored to achieve a maximum solar absorptance and low thermal emittance. The details of the deposition method can be found in Dan et al., 2016. The thicknesses of the individual layers of W, WAlN, WAlON and Al_2O_3 were found to be 125, 40, 40 and 62 nm, respectively.

4.2.2 Characterization of selective coatings

The UV-VIS-NIR optical properties of the coating have been characterized at room temperature using a commercial spectrophotometer (PerkinElmer Lambda™ 950), equipped with an integrating sphere for directional-hemispherical reflectance measurements at 0°. Room-temperature solar absorptance and total normal emittance values were determined using a solar spectrum reflectometer and hand-held emissometer (Devices and Services). Their standard uncertainties are given as 0.003 and 0.01, respectively. The high-temperature emittance measurements were performed using the custom-made HAIRL emissometer, as described in Section 3. Measurements were performed first in 10^{-3} hPa vacuum, and then in air, for both samples. No turbomolecular pump was available at the time of this measurement, which explains the lower vacuum level. The temperature of the samples was measured by spot-welding two Type K thermocouples in the intrinsic method directly to the SS substrate, as welding to the coating itself was deemed impractical. Thermal gradients were neglected because of the low thicknesses and high thermal conductivities of all layer materials.

A basic microstructural characterization of the coatings was carried out using X-ray diffraction (XRD). The samples were tested before and after emissivity measurements in air to observe the changes induced by the heat treatment. A Bruker D8 diffractometer with Cu K_α radiation ($\lambda = 0.15406$ nm) was used in Bragg-Brentano geometry in an angular range of $2\theta = 10 - 60°$. Further microstructural studies beyond the scope of this thesis can be found in Dan et al., 2018a.

4.2.3 Synthesis and processing of spinel coatings

$CuCr_2O_4$ and $CuFeMnO_4$ nanoparticles (hereafter referred to as CCO_4 and $CFMO_4$) were synthesized using a hydrothermal method described in Rubin, Chen, and Chen, 2019. $Cu_{0.5}Cr_{1.1}Mn_{1.4}O_4$ nanopowders (hereafter referred to as $CCMO_4$) were purchased from Foshan Huayi Ceramic Colours Co., Ltd. These nanopowders were synthesized through mixing starting metal oxides at high temperature with ball milling until a homogeneous composition was formed.

Details of the deposition procedures can be found in González de Arrieta et al., 2019. Different procedures were used depending on the desired density of the coatings. In the case of the dense coatings of CCO_4 and $CCMO_4$, they

were prepared using a solution of nanoparticles, methyl phenyl polysiloxane resin binder (SILIKOPHEN® P80/X, Evonik), isobutanol, and xylene. The solution was mixed in a ball mill, sprayed onto Inconel® 625 substrates, and then dried and cured from room temperature to 1023 K. The resulting coatings consisted of agglomerated nanoparticles in an amorphous silica matrix and had thicknesses of ~ 25 μm ($< 10\%$ dispersion).

In the case of the porous $CFMO_4$ and $CCMO_4$ layers, sacrificial polymer beads were added to the solution (Kim et al., 2016; Moon et al., 2015). Two types of beads were used, with average sizes of 1.3 μm and 400 nm. The deposition and curing procedures were identical to the dense coatings. The polymer beads decompose at 1023 K during the curing process, leaving nano- and micro-pores in the material. A porous $CFMO_4$ coating was deposited on top of a CCO_4 layer to form a tandem coating, whereas the porous $CCMO_4$ one was produced as a standalone sample directly onto the Inconel 625 substrate. The thicknesses obtained were around 5 μm for the former and 25 μm for the latter. Finally, the commercial LA-CO® Pyromark 2500 paint was diluted with xylene and toluene 10% (mass fraction), spray-coated, and cured with the same recipes as mentioned above.

All coatings were deposited onto Inconel 625 substrates, and so one additional uncoated sample was also prepared for emissivity characterization. Its surface state was studied using a mechanical roughness tester (Mitutoyo SJ-201). The measured roughness parameters were $R_a = 0.23$ μm, $R_q = 0.30$ μm, and $R_z = 1.88$ μm.

4.2.4 Characterization of spinel coatings

The morphology and particle size of as-cured samples were investigated by scanning electron microscopy (SEM) surface images (Zeiss Sigma 500, acceleration voltage 10 kV). The particle sizes of each coating were measured using the ImageJ processing software. The UV/VIS/NIR reflectance spectra of the coatings have been measured at room temperature with a Jasco V780 spectrophotometer equipped with a 150 mm integrating sphere coated with a Spectraflect® diffuse coating. The measured spectral range was 0.28–2.5 μm, with a stated photometric accuracy of 0.3%. The thermal stability and evolution of the microstructure and solar absorptance of the coatings have been extensively characterized previously in Rubin, Chen, and Chen, 2019.

In the case of the $CCMO_4$-based ones, they showed improved solar absorption properties compared to Pyromark, with very little to no degradation after annealing at 1073 K for 2000 h.

The instrumental setup used to perform the emittance measurements is the HAIRL emissometer. Samples are heated using resistor elements, and the surface temperature is measured using two symmetrically located type K thermocouples spot-welded onto the metallic substrate, in an area with ensured good thermal homogeneity. The atmosphere inside the chamber can be controlled using a turbomolecular pump. All measurements in this work have been performed in air, except for that of the substrate, which was measured in a 10^{-4} hPa vacuum. Blackbody measurements have been performed in the corresponding atmospheres to ensure the same optical path for all wavelengths. Inaccuracies around the atmospheric absorption bands of CO_2 and H_2O have been corrected using the transmittance spectra obtained by measurements on blackbodies in air and in N_2 atmosphere.

Directional spectral emittance measurements were made from 473 to 1073 K every 100 K for all samples. Aging effects at 1073 K were considered to be negligible due to the short measurement and stabilization times (< 1 h) (Rubin, Chen, and Chen, 2019). The spectral range was $2 - 22$ μm, and the measured angles were $10 - 80°$, every 10°. The emissivity results are compared to data for Pyromark deposited in the same conditions, as well as to the emissivity of the bare substrate (Inconel 625) acting as a control sample due to possible issues of semitransparency.

4.3 Results and discussion

4.3.1 Characterization of selective coatings

Normal spectral absorptance values of the as-deposited coatings were obtained from normal-hemispherical reflectance measurements ($\alpha = 1 - \rho$) from 0.3 μm to 2.5 μm. The results are shown in Figure 4.3, where the AM1.5 solar irradiance standard spectrum and the spectral exitance of a 773 K blackbody serve to illustrate the relative weights of each wavelength range. A normal spectral emittance spectrum at 773 K is also shown for completeness. The spectral selectivity of the material can be appreciated, with an integrated solar absorptance of 0.959 and a room-temperature total normal emittance of 0.08. Spectrally resolved emittance data are not available at room temperature, as they have been determined calorimetrically using a hand-held emissometer.

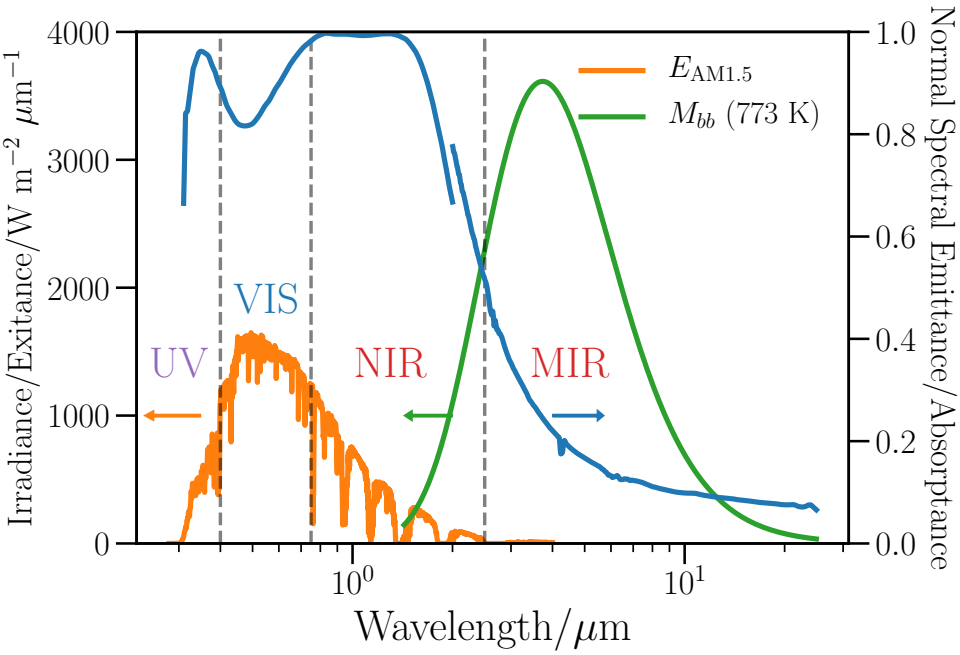

FIGURE 4.3: Combined normal spectral absorptance/emittance (773 K) spectra of a WWWA coating, compared with the spectral distributions of solar irradiance and blackbody exitance at 773 K.

Regarding the microstructural characterization of the coatings, the XRD diffractograms of a WWWA coating before and after the high-temperature emittance measurements are shown in Figure 4.4. Only peaks corresponding to the crystalline phases of W and AlN are observed in the as-deposited sample, which suggests that both top alumina and WAlON layers are amorphous. This is expected, and has been linked to the great thermal and mechanical resistance of the material, by avoiding grain boundary propagation of mechanical dislocations or chemical diffusion (Dan et al., 2016; Dan et al., 2018a). Similarly, the width of the AlN peak suggests a nanocrystalline nature. The amorphous nature of RF sputtered alumina has been demonstrated before (Reddy et al., 2014), and is expected as this material has a melting point much higher than the deposition temperature. Finally, the only observable product of heat treatment in air is the emergence of a broad peak, attributed to WO_3.

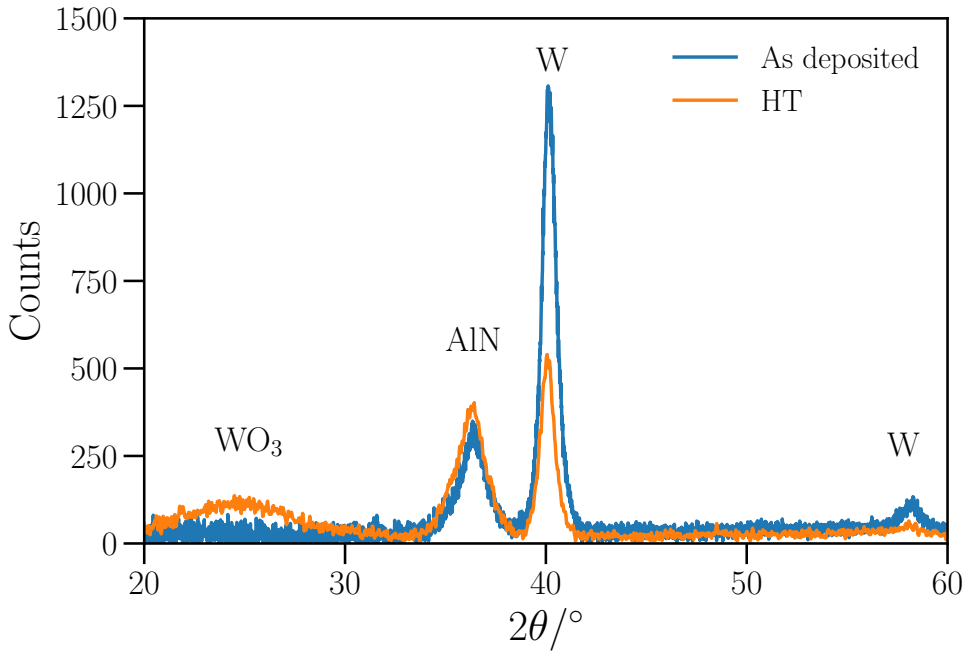

FIGURE 4.4: XRD characterization of a WWWA selective coating before and after heat treatment (HT) at 773 K for 12 h in air.

4.3.2 Emittance measurements of selective coatings

Figure 4.5 shows the first normal spectral emittance results of a comparison between the normal emissivity of the SS 316L substrate and that of both identical coatings (Samples A and B) at the desired working temperature of 773 K. Shades corresponding to the expanded uncertainty ($k = 2$) are shown together with the data, in this figure and thereafter. This serves to illustrate the improved optical properties of this multilayer selective system compared to the optical response of a bare metal. The coatings show a $\sim 50\%$ reduction in the emissivity beyond 5 μm, while their absorptivity in the near infrared reaches a value of more than double that of steel at 2 μm. Since both coatings studied presented identical emissivity spectra within experimental uncertainty at the desired working temperature, only values corresponding to Sample A will be discussed further.

The temperature dependence of the normal spectral emittance of Sample A is shown in Figure 4.6. Apart from the noisy low-wavelength data at 473, the main deviation from the average behavior is observed between 4 and 8 μm, as revealed in the inset. The most significant change takes place at the highest temperature (773 K), although the overall temperature evolution in the range of interest ($473 - 773$ K) is relatively weak. As shown elsewhere, high-temperature characterization is necessary in order to estimate the inaccuracies incurred when extrapolating room-temperature data, and thus decide the best course of action (Echániz et al., 2015; Jyothi et al., 2017). In any case, spectrally resolved data can be extrapolated by changing the temperature in Planck's law, which cannot be done with a hand-held emissometer.

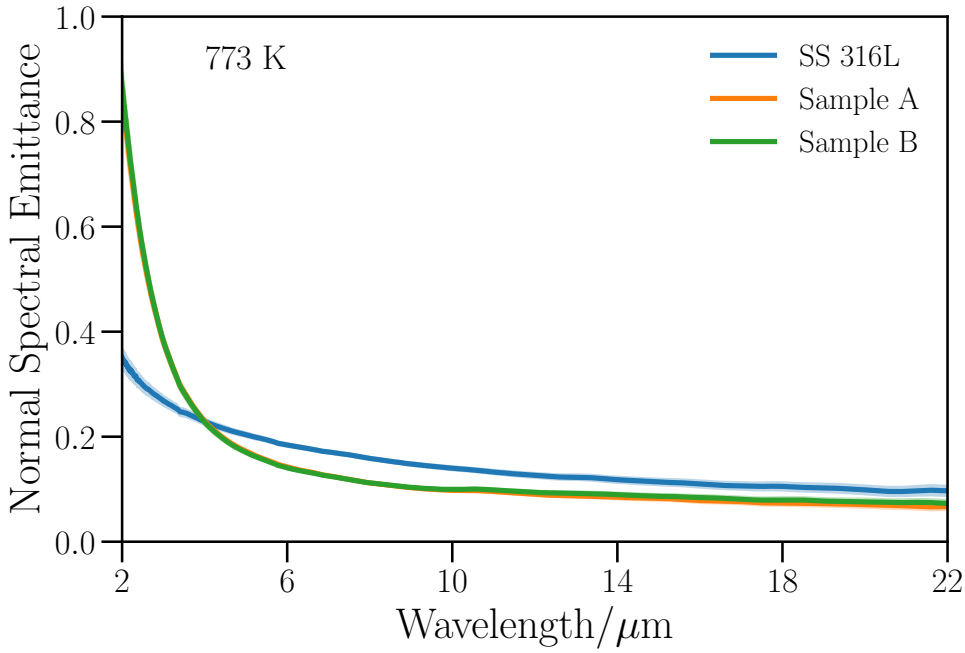

FIGURE 4.5: Normal spectral emittance of the coatings compared to the emissivity of the bare SS substrate. Shaded regions correspond to expanded uncertainty values ($k = 2$).

Given the weak temperature dependence of the results, measurements at 773 K are used to illustrate the angular dependence of the coatings. The emittance of a sample is strongly dependent on the observation angle, an aspect

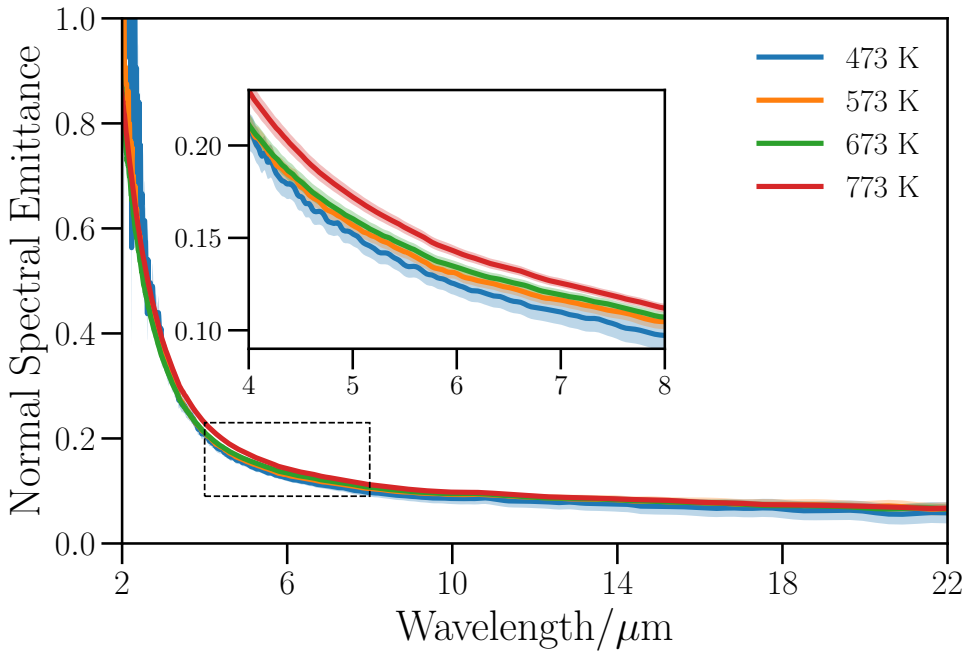

FIGURE 4.6: Temperature dependence of the normal spectral emittance of the coatings. Shaded regions correspond to expanded uncertainty values ($k = 2$).

that is often poorly studied for selective coatings. Directional emittance spectra at viewing angles from 10° to 80° for the wavelength range of $2 - 22$ μm are presented in Figure 4.7. The emittance of the coating decreases with an increase in viewing angle up to a crossover wavelength ~ 4.5 μm. Above this wavelength, a reverse phenomenon can be observed, with the emittance increasing with angle, as usual for metallic materials. It can also be observed that at $10 - 40°$, only small variations in emittance have been observed. At angles higher than 40°, the directional spectral emittance increases considerably in this long-wavelength range. This difference in spectral behavior was expected, since the three thin oxonitride layers are mostly transparent to long wavelenghts in order to minimize emission but strongly absorbent in the near infrared in order to capture the incident solar radiation. Therefore, at long wavelengths the optical properties of the coating are determined by the W layer and the effect of the more less metallic layers (and the dielectric-like

angular dependence illustrated in Figure 2.2a) is strongly revealed only at shorter wavelengths.

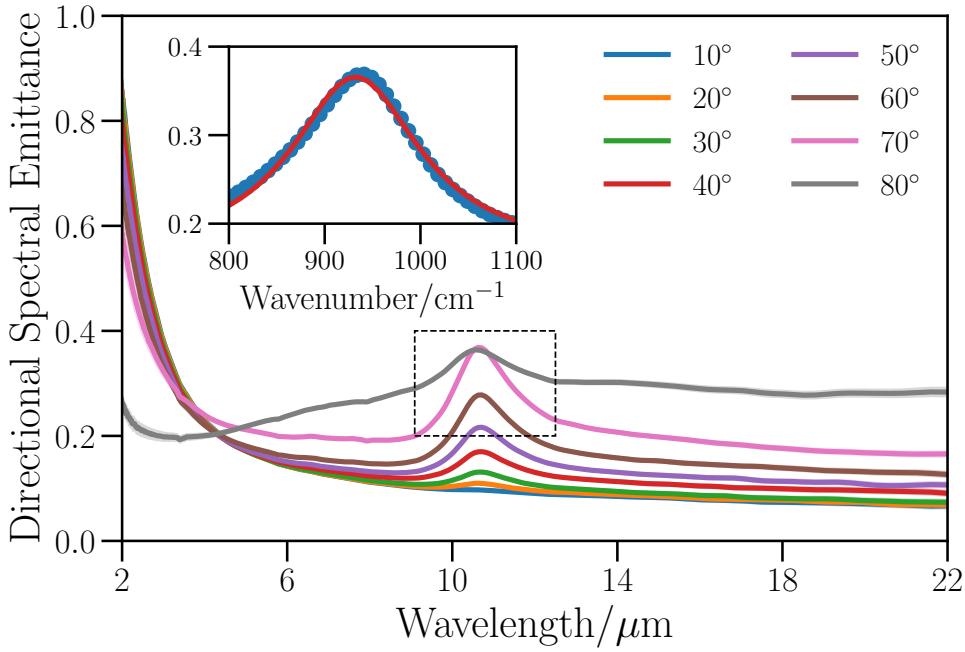

FIGURE 4.7: Directional emittance spectra of Sample A at 773 K. The inset shows a Voigt fitting (red line) to 70° data (blue dots) around the main peak at 932 cm^{-1}.

An interesting result of Figure 4.7 is the presence of a broad emittance maximum around $\sim$ 10.6 μm, whose intensity increases strongly with angle. An interferential peak is ruled out, as it should shift in peak wavelength when measured at different angles, and therefore different optical path lengths. The origin of this resonant peak, which is forbidden under normal incidence, can be found in the Berreman effect (Berreman, 1963). This effect is briefly overviewed in Appendix C. This effect induces a reduction of the reflectance, and thus an enhancement of the directional emittance, of a thin polar film around its longitudinal optical (LO) phonon mode. A simple calculation shows that this effect should be maximized for thicknesses around 100 nm (Equation C.3), a value which is consistent with the 62 nm thickness of the top alumina layer. Despite the alumina being in amorphous form, it has

been observed that the Berreman effect also takes place in amorphous materials (Trasferetti et al., 2004). These materials do not feature a properly defined phonon dispersion relation, but they do show effective LO and TO frequencies which are redshifted and broadened with respect to their crystalline counterparts.

A semi-quantitative measurement of the dielectric loss function $\mathrm{Im}(-1/\epsilon)$ (up to a multiplicative constant) can be performed by fitting the directional emittance data at 70° (at a resolution of 8 cm^{-1}) to a Voigt function, which consists of a convolution of Gaussian and Lorentz functions to account for possible differences in broadening mechanisms in amorphous materials (De Sousa Meneses et al., 2005). The fitting has been implemented using the free FOCUS software (De Sousa Meneses, 2020), with the result being shown in the inset of Figure 4.7. Even though the quality of the procedure could be improved to account for the skewness of the data, a Voigt function is sufficiently accurate to describe this phenomenon and to calculate a mean LO frequency of 932 ± 1 cm^{-1}. As corresponds to an amorphous material, its frequency is markedly different from that of the highest-frequency phonon mode of crystalline sapphire (907 cm^{-1}, Schubert, Tiwald, and Herzinger, 2000). Interestingly, the mean phonon frequency value of the amorphous material is found to be higher than its crystalline counterpart, contrarily to the behavior reported by Trasferetti et al., 2004 for amorphous and crystalline WO_3. Nevertheless, an LO peak in thin alumina films has been observed at room temperature at a close frequency of 935 cm^{-1} in Kaltchev and Tysoe, 1999, a value which matches the one measured in this work when considering the difference in temperature. In this same study, it was observed that this vibrational mode resembled that of γ-Al_2O_3, a cubic metastable allotrope of alumina. This can explain the discrepancy between the LO phonon frequencies of the crystalline and amorphous versions of Al_2O_3. Finally, the presence of this effect has been corroborated in the same type of coatings by Dan et al., 2019, with an observed LO frequency that matches the value reported in this work. The use of polarized reflectance measurements in that work shows that this effect takes places only for p-polarized radiation, thus confirming its origin in the Berreman effect.

Numerical integration of the directional spectral data as a function of temperature gives values of the total normal and total hemispherical emittances, shown in Figure 4.8. The integrated total quantities were calculated according to the procedures outlined in Section 3.6. Hemispherical values for both

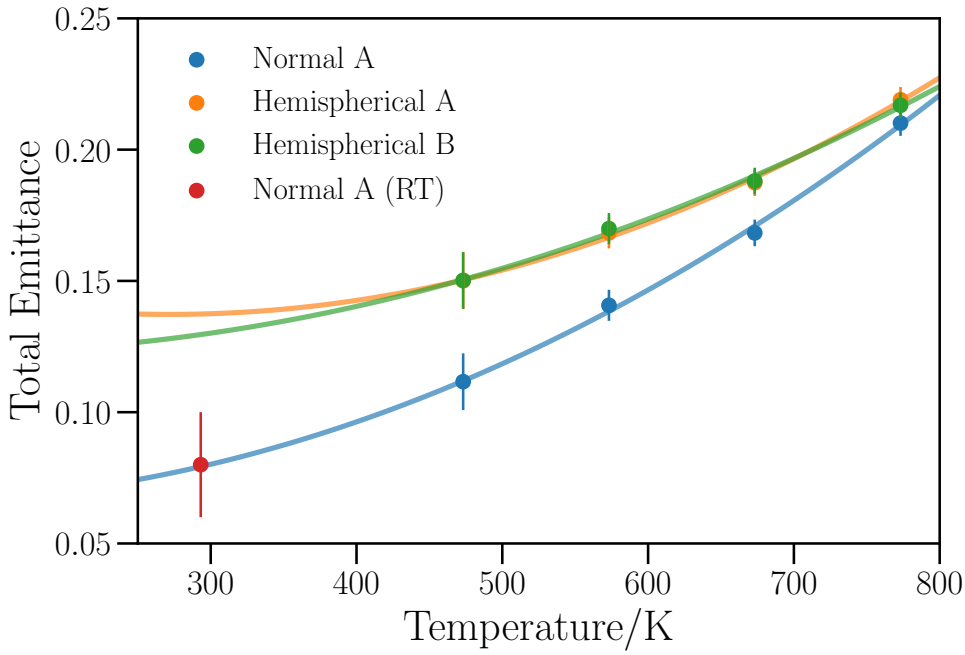

FIGURE 4.8: Total normal and total hemispherical emittances of Sample A as a function of temperature. Room-temperature total normal emittance of Sample A (measured using a hand-held emissometer) and total hemispherical data of Sample B are also shown for validation of the method. Error bars correspond to expanded uncertainty values ($k = 2$).

Sample A and B are shown to illustrate their good agreement and the reproducibility of measurements performed using the HAIRL emissometer. Calculation of this quantity is a significant improvement over previous studies, in which only the total normal emittance was calculated (Setién-Fernández et al., 2013; Echániz et al., 2015). Significant differences are observed between the absolute values and the temperature dependences of both properties, with higher discrepancies at lower temperatures (up to 35% at 473 K). This is due to the fact that the biggest relative variations of the emittance with the emission angle are located at longer wavelengths, where most of the emissive power is concentrated at low temperatures. All temperature-dependent data were

fitted to second-order polynomials, which are useful for comparison to room-temperature data obtained using a hand-held emissometer. The inclusion of this value proves the need to use a polynomial fitting instead of a linear one, which is suggested by Equation 2.42. This stems from the much larger increase of the spectral emittance in the NIR spectral region because of its selective nature. Overall, these results serve an additional purpose of validating the reproducibility of the integrated emittance measurements performed with the HAIRL device.

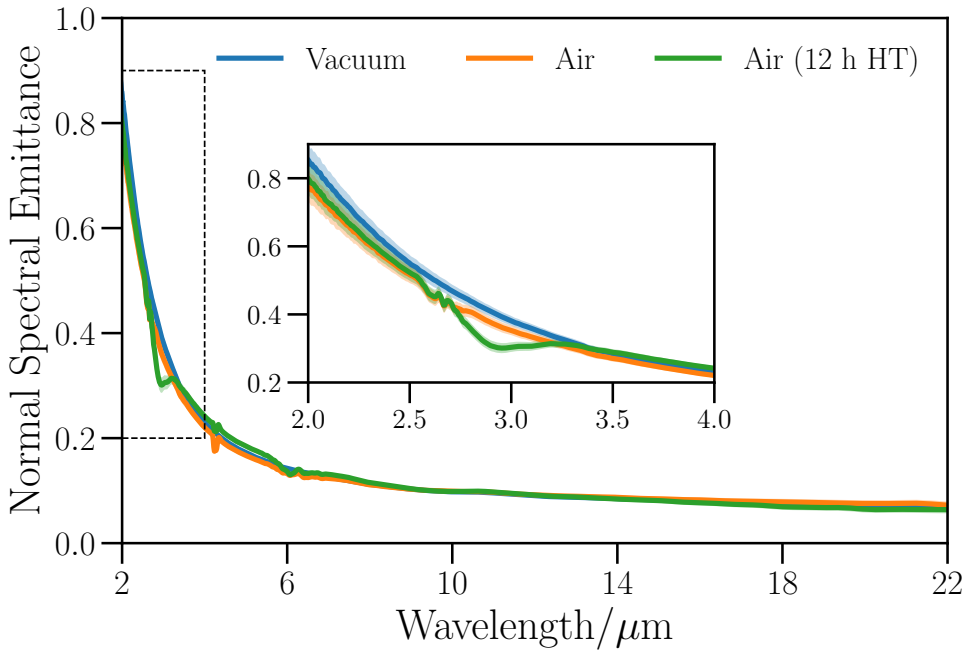

FIGURE 4.9: Normal spectral emittance of Sample A at 773 K in vacuum, in air, and after 12 h heat treatment in air. Shades correspond to expanded uncertainty values ($k = 2$).

Finally, the stability of the infrared properties of the coating was studied by performing another $473 - 773$ K thermal cycle in air. The results are shown in Figure 4.9. The high-temperature spectra in vacuum and in air show relatively good agreement within experimental uncertainty, except around the spectral lines of CO_2 and H_2O. Additionally, the sample was left at 773 K in air for 12 h while its normal spectral emissivity was being monitored every

30 minutes. As seen in Figure 4.9, a slight increase in the emissivity values in the $3-6$ μm spectral range was found, as well as a new band around 3 μm. This is consistent with the formation of a small amount of WO_3 as a result of W diffusion and sample oxidation, as revealed in the XRD results shown in Figure 4.4. The effect of this chemical change is deemed to be tolerable in the infrared, although it can influence the solar absorptance in a greater manner (Dan et al., 2018a).

4.3.3 Characterization of spinel coatings

The morphologies of the black spinel coatings are shown in surface SEM images (Figure 4.10). This allows characterizing the shape and particle size of dense $CCMO_4$, porous $CCMO_4$, the porous $CFMO_4$ top/dense CCO_4 bottom tandem, CCO_4, and Pyromark, respectively. CCO_4 nanoparticles were the smallest, with a range of average sizes from 50 to 100 nm; while $CFMO_4$, Pyromark, and $CCMO_4$ nanoparticles were similarly sized, with average sizes between 100 and 300 nm. Figure 4.11 shows SEM micrographs at lower magnification in order to compare the larger-scale microstructures of both $CCMO_4$ coatings (dense and porous). The most significant difference between the two samples involves the presence of larger and deeper pores for the porous sample, with mean diameters in a broad $0.5-5$ μm range. This feature results from the decomposition of polymer beads, which have a bimodal size distribution ranging from 400 nm to 1.3 μm, designed for more efficient light-trapping in cavities of different length scales (Kim et al., 2016).

The UV/VIS/NIR normal-hemispherical reflectances of the coatings at room temperature are shown in Figure 4.12. Integrated solar absorptance values of the spinel coatings have been obtained by numerical integration of these data and are shown in Table 4.1. They are consistent with results reported in Rubin, Chen, and Chen, 2019 to within the stated 0.3% photometric accuracy of the spectrophotometer. Only two samples show improved solar absorptance values with respect to Pyromark: porous $CCMO_4$ and CCO_4. Interestingly, the tandem structure is the worst-performing sample of all, despite its double-layer structure and porous surface. Thus, it is to be inferred that a combination of the correct composition and structrure is key to improving the solar absorptance. Finally, it is worth mentioning that CCO_4 is the most absorbing sample throughout the visible range, with its excellent performance being hampered only by its resonant modes in the NIR region (Levinson, Berdahl, and Akbari, 2005).

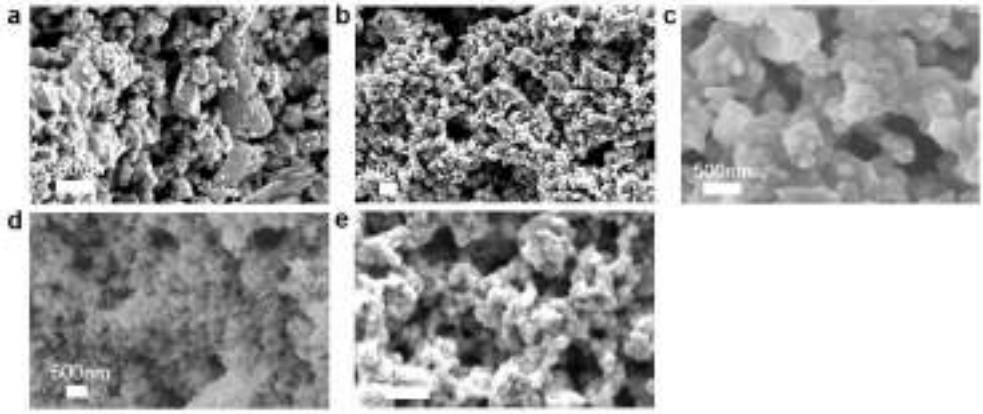

FIGURE 4.10: SEM images of solar absorber coatings (a) dense $CCMO_4$, (b) porous $CCMO_4$, (c) $CFMO_4/CCO_4$ tandem, (d) CCO_4, and (e) Pyromark.

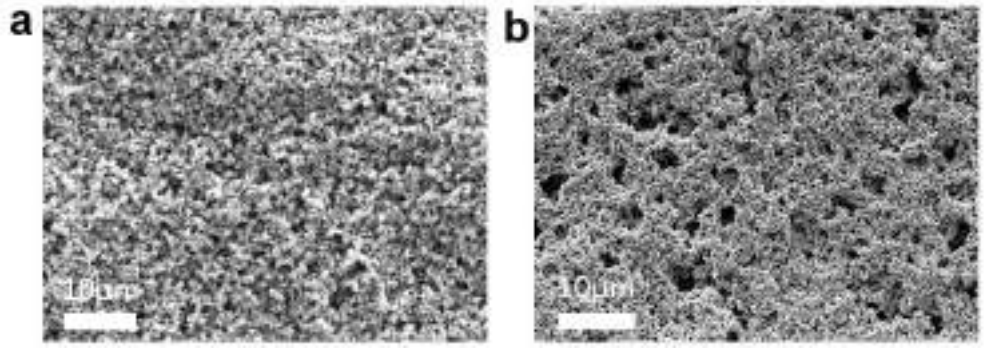

FIGURE 4.11: SEM images of the surface morphologies of both $CCMO_4$ coatings: (a) dense and (b) porous.

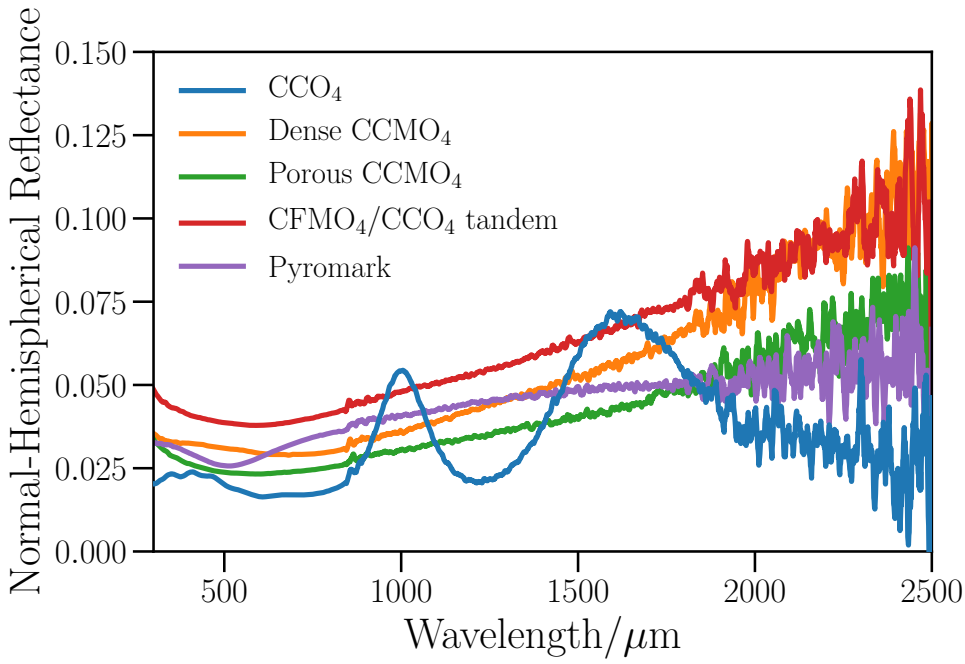

FIGURE 4.12: UV/VIS/NIR normal-hemispherical reflectance spectra of the black spinel coatings.

TABLE 4.1: Solar absorptances of the spinel absorber coatings.

Pyromark	$CCMO_4$ (D)	$CCMO_4$ (P)	CCO_4	Tandem
0.966	0.958	0.972	0.970	0.955

4.3.4 Emittance measurements of spinel coatings

Figure 4.13 shows the normal spectral emittance as a function of temperature for all samples. The substrate shows the general behavior predicted by Equation 2.40, decreasing with increasing wavelength and with a slight increase with temperature, which is mostly apparent in the long-wavelength region. This weak temperature dependence is typical for heavily alloyed metals, for which the electrical resistivity remains high at all temperatures, and thus shows little additional temperature increase. These measurements of the emissivity of the substrate were deemed necessary because of the influence the substrate may bear on the emittance of the materials through a certain

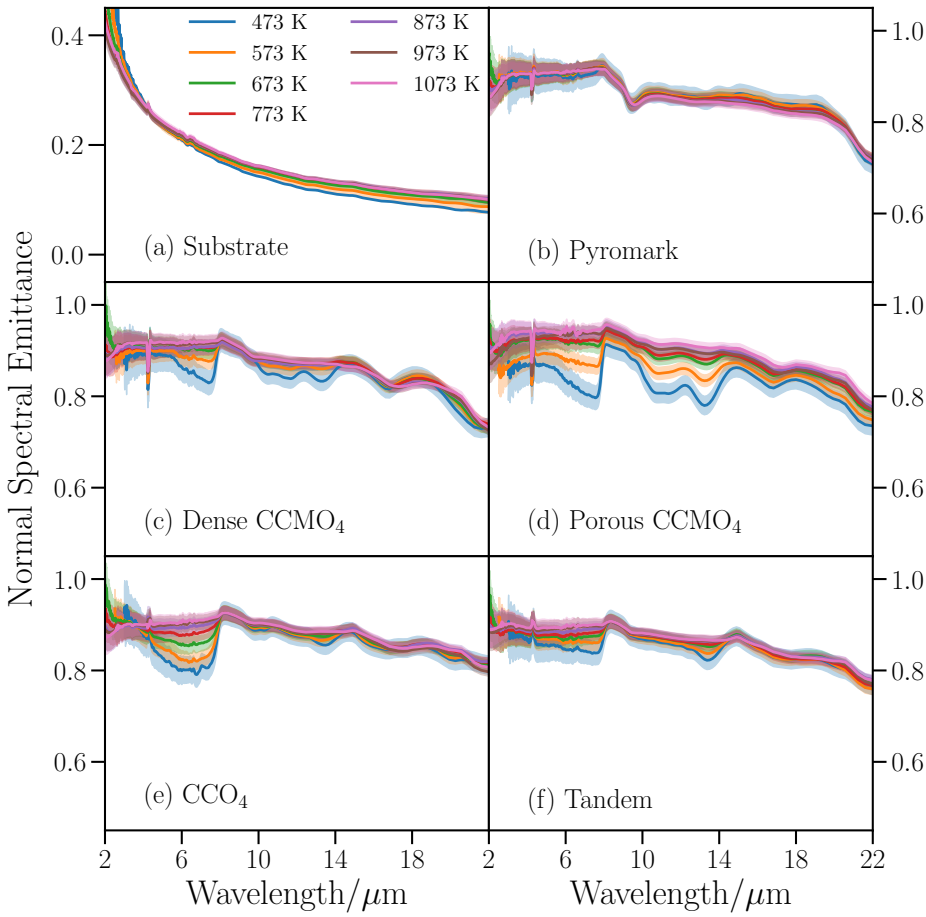

FIGURE 4.13: Normal spectral emittance spectra of the six samples as a function of temperature between 2 and 22 μm. Shaded regions correspond to expanded uncertainty values ($k = 2$). Note the different scales for the emissivity of the substrate and the emittances of the coatings.

degree of semitransparency. Such behaviors have been observed previously, especially for aged or thin coatings (Ho et al., 2014; Coventry and Burge, 2017). It is worth noting that these measurements have to be acquired from a substrate with the same surface state as the one found in substrates that are coated with the spinel paints. As no oxidation of the coated substrates has been found in these samples (Kim et al., 2016; Rubin, Chen, and Chen, 2019), measurements were performed in vacuum to avoid the strong oxidation typical of uncoated metals. The only exception is heavily aged Pyromark, which is not the case for the Pyromark sample studied in this work.

With regards to the coatings, their emittances are all relatively similar and much higher than the emissivity of the substrate. Whereas the emittance of Pyromark does not show any significant temperature dependence, those of all the other coatings experience a general increase with temperature. Temperature-independent spectral behaviors of Pyromark have been reported, although the choice of substrate was also found to induce systematic differences in the normal spectral emittance among samples (Ho et al., 2014). The temperature dependences of the new coatings are mainly observed at wavelengths below 8 μm, which can be due to the thermal evolution of the intrinsic optical properties of their constituent nanoparticles. Interestingly, this spectral range is also the one where most thermal radiation is emitted at high temperatures. The observed changes are reproducible within the experimental uncertainty, and thus not a consequence of microstructural evolution or degradation. A possible substrate-induced origin for these observations is discouraged due to the absence of any substantial increase in the emissivity of the substrate at such wavelengths. Out of all the measured coatings, the behavior of the porous $CCMO_4$ sample (Figure 4.13d) has the largest temperature dependence, showing an increasing emittance with temperature throughout the entire spectral range. Overall, these results suggest that differences in composition are not the most relevant source of high-temperature emittance variations and that similarly deposited coatings have comparable normal spectral emittance values. Moreover, they also prove that the common practice of extrapolating room-temperature emittance spectra to high temperatures can potentially incur in inaccuracies when the coatings exhibit temperature-dependent properties (Echániz et al., 2015). In this case, only Pyromark shows a constant spectral emittance with temperature in the entire spectral range.

The basic microscopic origin of the spectral emittance of these materials is to be found in the intrinsic optical response of the spinel nanoparticles. It

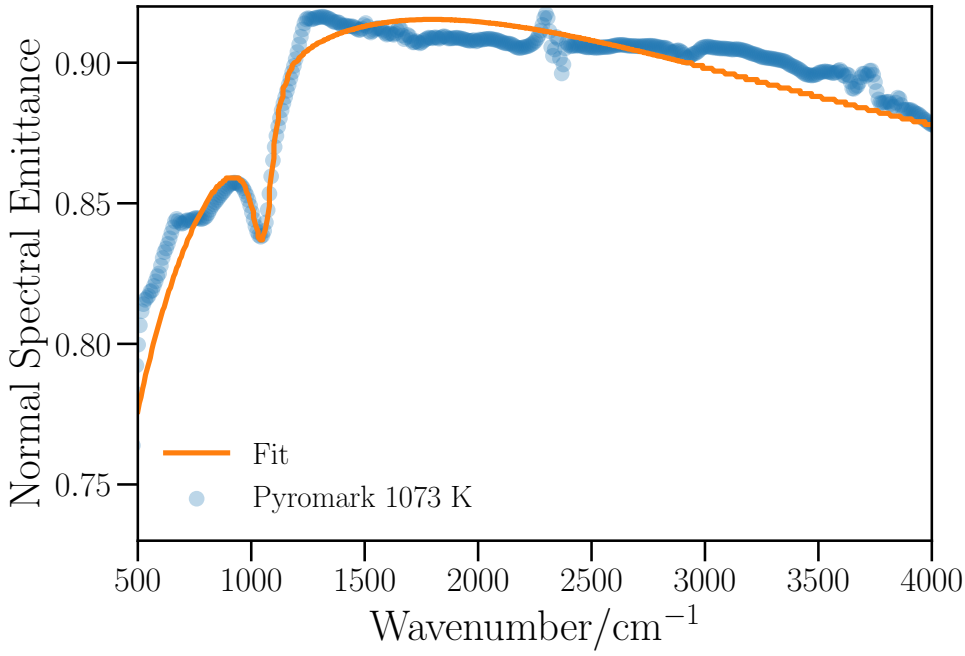

FIGURE 4.14: Normal spectral emittance of Pyromark at 1073 K fitted to a generalized Drude-Lorentz model (Equation 2.38).

is well known that materials such as $CuCr_2O_4$ exhibit non-negligible electrical conductivity, especially at higher temperatures in air (De, Ghose, and Murthy, 1982; Petric and Ling, 2007). One known mechanism for this involves the oxidation of surface Cr ions by atmospheric oxygen, with the subsequent release of free electrons (De, Ghose, and Murthy, 1982). This gives a high absorption coefficient over a broad spectral range, a fact that has been recognized as the cause of their optimal absorbing properties in both the visible and NIR ranges (Levinson, Berdahl, and Akbari, 2005). This behavior is common for transition-metal oxides (black conductors), which often feature very high emittances due to non-stoichiometry (Rousseau et al., 2005; Gervais, 2002). The presence of free electrons induces an opacification of the material, but their concentration is not sufficient to reflect effectively incident radiation at the surface. This behavior is well described by a fitting to the extended Drude-Lorentz model (Equation 2.38), as shown in Figure 4.14 for Pyromark at 1073 K. The fitting has been implemented using the free FOCUS

software (De Sousa Meneses, 2020). A semi-quantitative agreement can be observed for a simple model with only one phonon, although more Lorentz-like resonances can be used to reproduce other spectral features in the other coatings at lower temperatures. This fitting procedure is simplistic and does not account for effects such as surface roughness; thus, it is is not expected to accurately reproduce the measured data and is only meant to show the origin of the high emittance of these materials. More complex models using Monte Carlo methods to calculate the effects of sample texture have been formulated for similar transition-metal oxide compounds (Ta et al., 2010).

Another important step for accurate emittance characterization is to take into account its angular variation. Directional spectral measurements results are reported in Figure 4.15 for all samples. The highest temperature measured (1073 K) is chosen to illustrate the main properties of the directional spectra of the materials, as it corresponds to a temperature close to that which is desired to achieve in future applications. In any case, similar directional dependences have been observed at all temperatures. Regarding the substrate, its directional emissivity increases with the emission angle in the way that is expected for a metallic material and reaches its maximum value at around $70^\circ - 80^\circ$, depending on wavelength. In the case of the coatings, their angular dependences are remarkably similar. The high values they all feature in the normal direction remain nearly constant up to 50° and then decrease to reach relatively low values (~ 0.35) at 80°. It is interesting to note that all 80° spectra are remarkably similar, including the substrate. This shows the significance of the semitransparency issue, which has been hinted at by other authors when studying the thickness- and substrate-dependent properties of Pyromark samples (Ho et al., 2014; Coventry and Burge, 2017).

The most anomalous case among the directional spectral emittances of the coatings corresponds to the porous $CCMO_4$ one (Figure 4.15d). Its emittance is slightly higher than all the others in the normal direction but begins a faster decrease at an angle of only 40°, reaching even lower values than those of the substrate at 70°. This anomalous angular dependence implies that, for example, the value of its emittance at 60° is almost half of that of the corresponding value for its dense counterpart (Figure 4.15c), although the emittance at 80° is similar to that of the other materials. For this coating, the spectral curves also show a crossover in the angular dependence, with an emittance curve for 80° that is larger than for 70° at wavelengths longer than 5 μm. The results of these coating do not follow the standard predictions of angular dependence for dielectric materials (Howell, Mengüç, and Siegel, 2010; Modest,

2013). However, it is important to note that the basic theory only applied to semi-infinite homogeneous materials and ideal surfaces, which is clearly not the case with any of the studied coatings. A possible explanation relies on the fact that the dominant absorption mechanism in the porous coating is due to surface roughness (Kim et al., 2016; Rubin, Chen, and Chen, 2019), a mechanism of optical absorption that is well known to lose effectiveness at larger angles. In the case of the other materials, their bulk absorption is stronger due to their higher density, and their decrease with angle is thus less pronounced. Finally, all coatings converge to roughly similar spectra at 80° due to the influence of the substrate.

Directional measurements also show certain spectral features which are common to all five coatings to varying degrees, such as the 8–10 μm band, and the 3, 15 and 20 μm peaks for high angles. Their presence for all materials suggests an origin common to all of them which is not to be found on the intrinsic optical properties of the constituent nanoparticles. The band at ~ 9 μm has been observed before for some Pyromark samples depending on the substrate used (Ho et al., 2014), but no reference to the other spectral features (which are enhanced at oblique angles) has been made. An explanation can be made by taking into account that absorption bands at these same wavelengths can be found in the infrared spectrum of silica glass (Kitamura, Pilon, and Jonasz, 2007), which is present in all coatings as a binder phase. Thus, differences among samples can be traced back not only to the use of different substrates (Ho et al., 2014), but also to differences in the small secondary phases remaining from the deposition and curing processes. Similar to the results on selective multilayer coatings shown in Section 4.3.2, it is not uncommon for complex multi-component materials to reveal specific spectral signatures and peaks only when emitting at oblique angles, due to the different optical properties and directional dependences of their constituents. These non-ideal behaviors highlight the importance of microstructure in determining the thermal radiative properties of porous materials and hint at the possibility of tuning them to improve their performance in heat transfer applications (Rousseau et al., 2016).

In order to better visualize the behaviors discussed above, directional spectral values at two discrete wavelengths for both $CCMO_4$ samples (dense and porous) have been plotted in Figure 4.16, where the values at 0° and 90° have been set to the values predicted by the electromagnetic theory, as described in Section 3.6. These two samples have been selected to check the influence of the microstructure in the directional emittance of samples

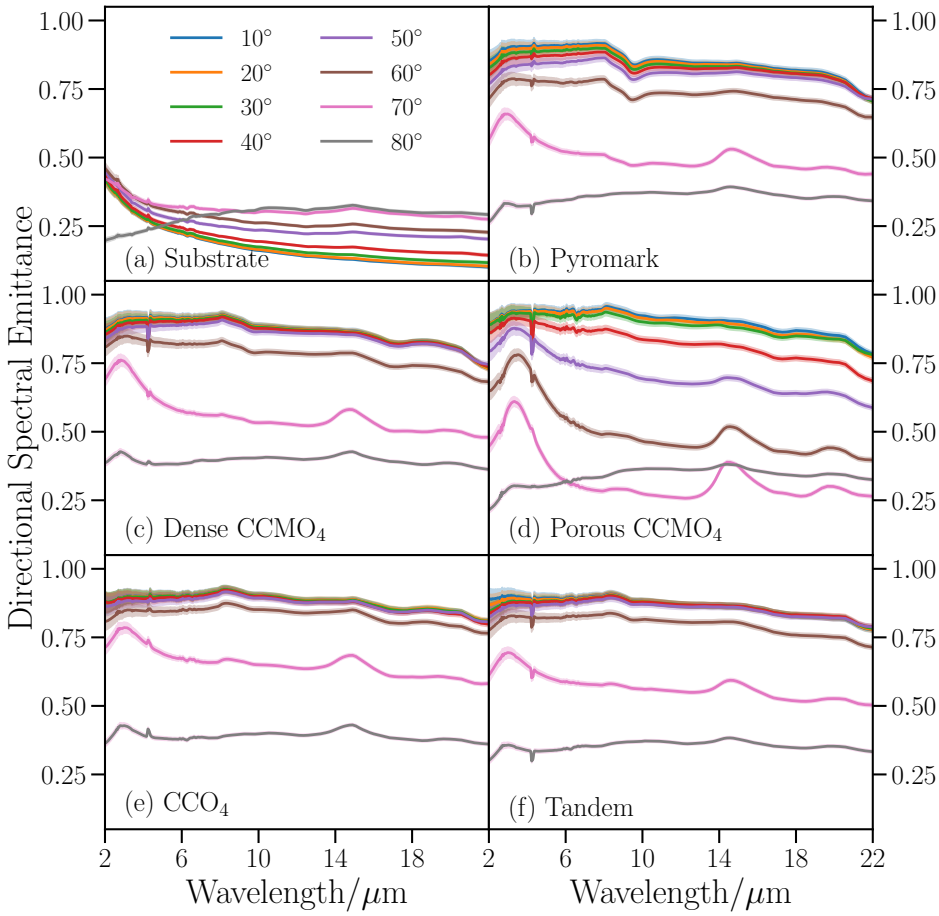

FIGURE 4.15: Directional spectral emittances at 1073 K for all six samples between 2 and 22 μm. Shaded regions correspond to expanded uncertainty values ($k = 2$).

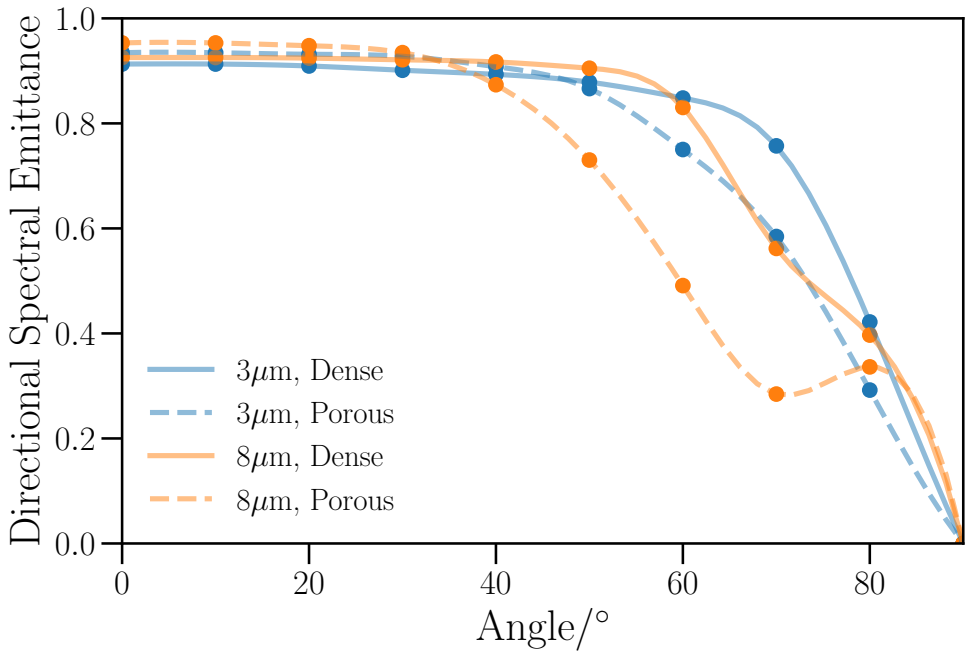

FIGURE 4.16: Comparison of the directional spectral emissivities (1073 K) of the two $CCMO_4$ coatings (dense and porous) at two representative wavelengths.

with the same composition. It can be seen that both materials show similar angular dependences at both wavelengths, but that non-ideal tendencies are more significant for the porous sample. This is best observed at 8 μm above 40°, where the emittance of the porous sample decreases faster than the predictions of the electromagnetic theory (Figure 2.2a) up to 70° and then increases again at 80°. On the contrary, the emittance of the dense sample remains relatively constant up to 60° and then decreases rapidly to zero only above 70°, in agreement with the theoretical predictions. The differences at 3 μm are much less pronounced because this wavelength corresponds to one of the infrared-active modes of the silica glass binder (Kitamura, Pilon, and Jonasz, 2007), and therefore presents higher emittances throughout the entire angular range. Overall, this Figure helps to visually appreciate the strong directionality that can be induced by the use of porous structures and rough surfaces.

Attempts at describing the directional emittance of materials with complex geometry, such as packed beds of spheres or agglomerated nanoparticles, have been made using the radiative transfer equation and Mie's scattering theory (Sacadura, 2011). Other approaches use combinations of extended Drude-Lorentz models and numerical ray tracing to account for complex geometries (Ta et al., 2010). However, agreement of the predicted behavior to the experimental data has traditionally been poor for high angles of incidence (Lopes et al., 2000). A qualitative picture of the sharp decrease of emittance with the emission angle can be formed by considering shadowing effects. In this picture, normally incident light is trapped by multiple reflections inside the geometric features of these systems, but the emission at oblique angles of incidence interacts with an effectively smoother surface since most of the texture is not accessible from those angles. Shadowing effects are known to be key for the thermal radiative properties of other materials with complex geometries at the μm length scale, such as V-grooves or foams (Li et al., 2018; Mulford et al., 2018). Thus, it is suggested that directional selectivity can be inherently induced by the same mechanisms responsible for enhanced light trapping in the normal direction. Some features of these materials, such as the presence of silica glass binder, can be accounted for by effective medium theories, which describe the macroscopic response of composite materials with length scales much lower than the the wavelength range of interest (Stroud, 1998). However, these models cannot describe the infrared response of materials with complex surfaces at the μm scale (Figures 4.10 and 4.11). Therefore, the difficulty of accurately reproducing the full range of radiative properties of these type of materials ensures that experimental measurements will continue to be essential for their applications.

The total hemispherical emittance is the key parameter for solar-to-thermal efficiency estimations, because it controls the total amount of heat lost by thermal radiation at high temperatures (Ho et al., 2014). It can be calculated by numerical integration in both wavelength and solid angle of the temperature-dependent directional spectral data shown previously, according to the procedure described in Section 3.6. Results of the integration for the coatings are shown in Figure 4.17. It is observed that in all cases their total hemispherical emittances increase up to around 773 K and then mostly stabilize. As expected from the directional data, the porous $CCMO_4$ sample is again the most discrepant material, with a total hemispherical emittance that is consistently lower than any of the other samples at all temperatures. As discussed above, the strong angular dependence of this sample is the key to

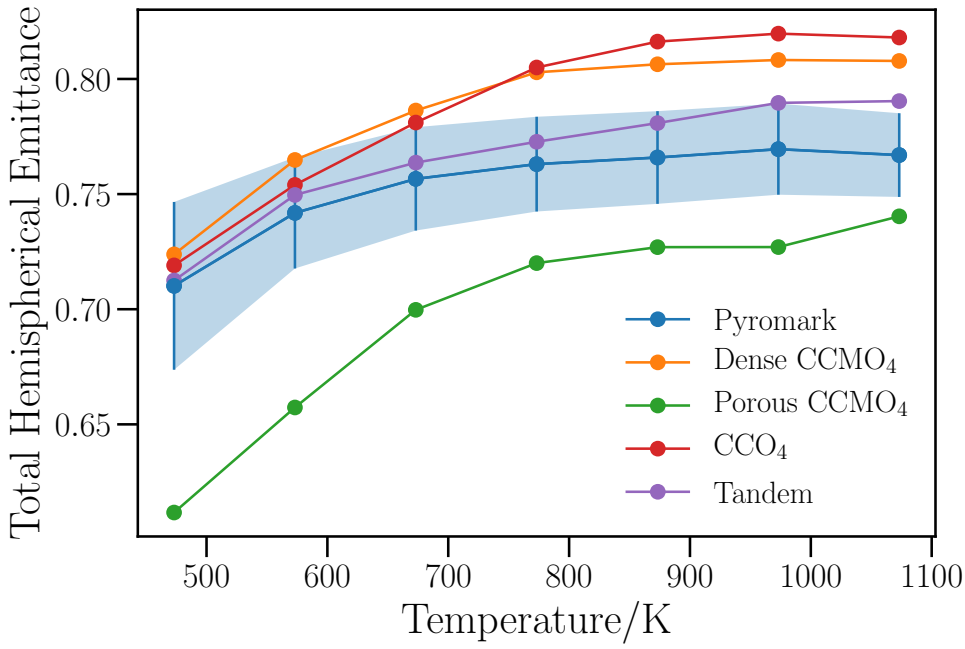

FIGURE 4.17: Total hemispherical emissivities of the five coatings as a function of temperature. Error bars correspond to expanded uncertainty values ($k = 2$).

its overall reduced heat losses and degree of directional selectivity. It boasts the highest solar absorptance and high-temperature normal emittance of the entire set of samples, but its emission at off-normal angles is significantly inhibited by a fast angular decrease of the directional emittance. This translates into a structure with a reduced total hemispherical emittance, which may be a strategy worth pursuing in the design of new materials.

The optical properties of the porous $CCMO_4$ sample can be regarded as typical of a directionally selective surface, a topic of great interest due to the potential of tuning the emittance of materials to emit preferentially in a given direction (Badescu, 2005). Surfaces with this property can offer an increase in efficiency by limiting the amount of heat lost by radiation at non-normal directions. Crucially, this improved efficiency does not necessarily degrade at high temperatures, compared to the more common spectrally selective surfaces (Blanco, Martín, and Alarcón-Padilla, 2004). Many strategies for making

directionally selective materials have been studied, such as photonic crystals (Hamam, Celanovic, and Soljačić, 2011; Shen et al., 2014; Florescu et al., 2007), V-grooves (Mulford et al., 2018), optical cavities (Weinstein et al., 2014) and metamaterials (Costantini et al., 2015; Sakr and Bermel, 2017; Wang et al., 2015). Contrary to those approaches, the directional selectivity obtained in this study is achieved directly as part of the spray deposition method, with the associated reduction in costs.

The behavior of the other coatings is much more similar among themselves, especially at low temperatures. Nevertheless, some tendencies can be observed. The dense $CCMO_4$ and CCO_4 coatings, which are the most similar samples regarding microstructure, also feature close total hemispherical emittance values for the entire temperature range, bearing the highest overall values at high temperatures. Meanwhile, the tandem coating features emittances much closer to those of Pyromark, which correspond to the intermediate values between the porous $CCMO_4$ and the CCO_4, albeit closer to the latter. This is expected, since most of the tandem structure consists of a denser microstructure, with only the top 5 μm corresponding to a porous layer (Kim et al., 2016; Rubin, Chen, and Chen, 2019). It is interesting to note that this material, which has the most complex structure, exhibits the lowest solar absorptance of the five studied coatings (Table 4.1) and does not offer a reduced emittance with respect to Pyromark to compensate for this.

As the last part of this Section, the Pyromark sample has been used as a benchmark for verification of the obtained results and discussion of the variability of literature data. A substantial amount of data on the radiative properties of this paint is available in both the scientific and technical literature, although with a well-known dispersion of values, few reported uncertainties, and mostly in the normal direction (Boubault et al., 2017; Fang et al., 2018; Höser, Wallimann, and Rohr, 2016; Ho et al., 2014; Suo-Anttila, Nakos, and Gill, 2004; Coventry and Burge, 2017). It is important to note that the total hemispherical emittance is the only parameter that accounts for all contributions to the radiative heat losses. Temperature-dependent total normal and total hemispherical experimental data have been separately reported in the literature (Höser, Wallimann, and Rohr, 2016; Ho et al., 2014; Suo-Anttila, Nakos, and Gill, 2004), but no references containing both total normal and total hemispherical measurements for the same samples have been found. A comparison of the data contained in this work to available literature data from Höser, Wallimann, and Rohr, 2016; Ho et al., 2014; Suo-Anttila, Nakos, and

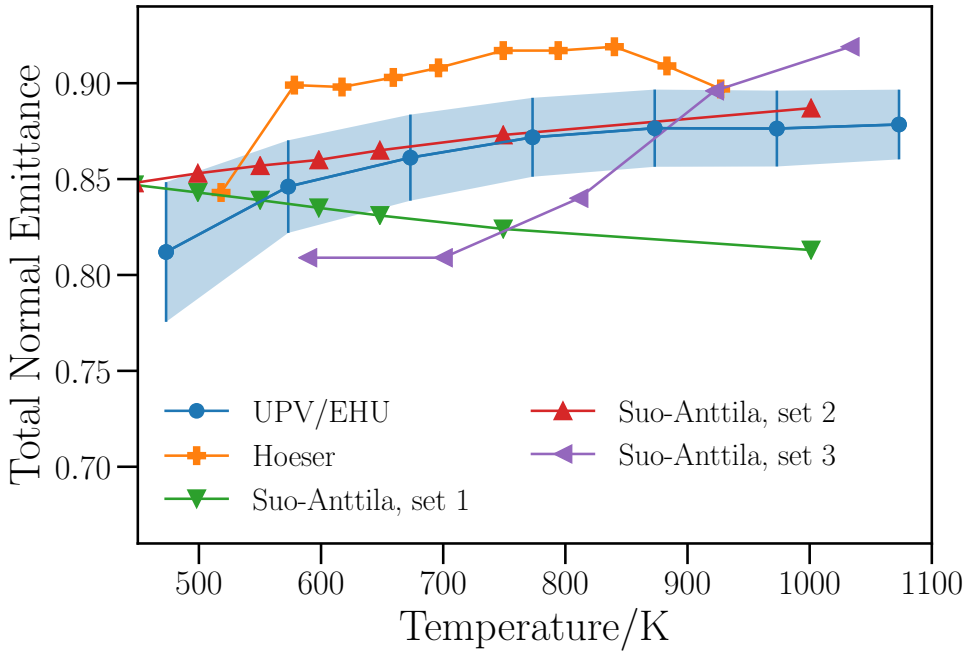

FIGURE 4.18: Total normal emittance of Pyromark reported in this work compared to data from the literature (Höser, Wallimann, and Rohr, 2016; Suo-Anttila, Nakos, and Gill, 2004). Error bars correspond to expanded uncertainty values ($k = 2$).

Gill, 2004 is given in Figure 4.18 (for the total normal emittance) and Figure 4.19 (for the total hemispherical).

A qualitative agreement can be observed for both quantities, although the aforementioned dispersion of values is evident. Most total normal emittance datasets shown in Figure 4.18 feature a positive temperature dependence similar to the data contained in this work, although a negative one has also been found (set 2 from Suo-Anttila, Nakos, and Gill, 2004). In the case of the total hemispherical emittance (Figure 4.19), data from Suo-Anttila, Nakos, and Gill, 2004 agree somewhat with the present results, while those of Ho et al., 2014 show a qualitatively similar but much higher total hemispherical emittance. The discrepancies between datasets, the effects of extrinsic factors (such as morphology and heat treatment) and the difficulty of finding reliable emittance data for Pyromark have been previously discussed by Suo-Anttila,

Nakos, and Gill, 2004. It should be noted that not all measurements have been performed using the same methods. The data by Höser, Wallimann, and Rohr, 2016 have been obtained using an infrared camera in the 8–14 μm range, while data in Ho et al., 2014 have been theoretically extrapolated from normal data obtained using reflectance measurements. This assumes implicitly that the angular dependence of this material is the one predicted by the theory for an ideal dielectric material, which has been shown to not be necessarily the case for all samples. This discrepancy can also be partly explained by the observed variability of samples deposited on different substrates in the same reference. Finally, it must be noted that the curing treatment of Pyromark is known to bear a crucial influence on its optical properties (Boubault et al., 2013). Explaining this discrepancy is key to the proper analysis of costs associated with this material, as well as the potential gains of substituting it with other materials with more optimal optical properties and thermal stability (Ho and Pacheco, 2014). Overall, this brief comparison highlights the significance of direct emittance measurements at working temperatures and the need for accurate characterization of materials.

4.3.5 Efficiency of the coatings

Accurate temperature-dependent emittance data allow for more reliable estimations of the real efficiency of the materials in CSP applications. This final Section presents estimates of efficiencies of the materials presented in this Chapter at the desired working temperatures of each application with representative solar concentration factors (Weinstein et al., 2015).

The simplest way to report the selectivity of a solar absorber is to give a ratio of the solar absorptance and total normal emittance at room temperature, often referred to as α/ε (Kennedy, 2002), but this value in itself is not very useful, as it does not account for temperature, angular emission, or solar concentration factor. Furthermore, it is unbounded, and so comparisons between materials are non-trivial. In this regard, the optimal simplified metric is given by Equation 4.1. This η_S parameter implicitly assumes that heat transfer takes place only by radiation, directly between the Sun and the absorber without participating media. This assumption does not account for convective losses, radiative transfer with the environment, or the transmittance of glass envelopes of parabolic trough systems (Weinstein et al., 2015). However, all these technical complications do not alter the intrinsic efficiencies of

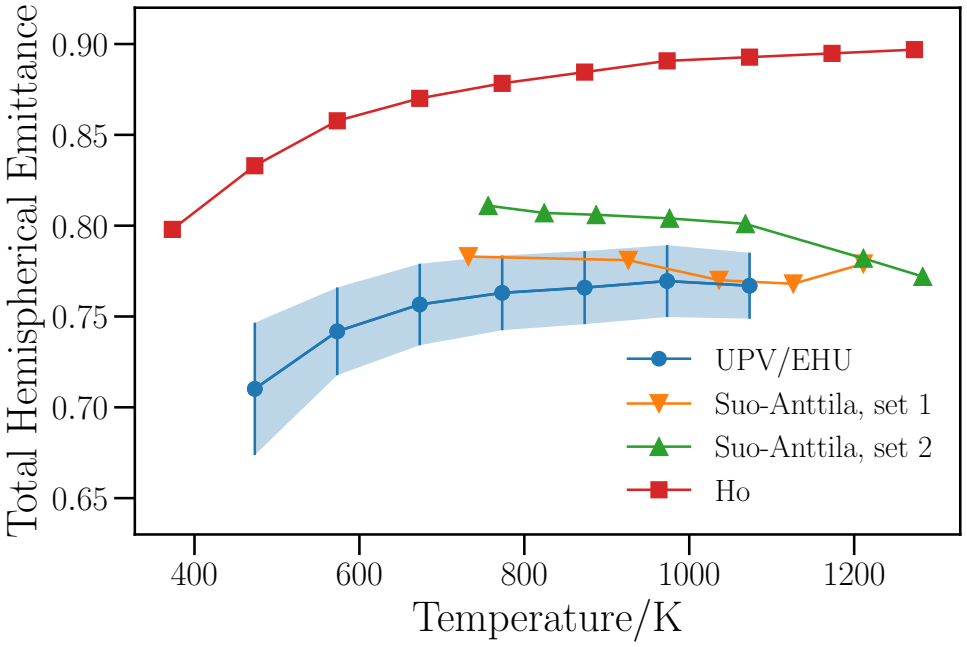

FIGURE 4.19: Total hemispherical emittance of Pyromark reported in this work compared to that calculated from total normal measurements (Ho et al., 2014) and data compiled in Suo-Anttila, Nakos, and Gill, 2004. Error bars correspond to expanded uncertainty values ($k = 2$).

the coatings. Finally, other metrics which take economic parameters into account can be found in the literature, but they will not be considered in this work (Ho and Pacheco, 2014; Boubault et al., 2016; Boubault et al., 2017).

The solar-to-thermal conversion efficiencies of the WWWA coatings and the black spinel coatings are shown in Figures 4.20 and 4.21, respectively. In the case of the selective coatings, only the results corresponding to Sample A are shown. Solar efficiencies corresponding to the $473 - 773$ K temperature range for three solar concentration factors of 40, 80, and 120 suns are reported. This covers the entire expected region of application of these materials. As expected, most solar conversion efficiency values lie above 0.9, even at the highest temperature of 773 K for concentration factors of 80 suns or more. Regarding the black spinel coatings (Figure 4.21), a single receiver temperature

of 1073 K has been selected to illustrate the differences among the coatings, with the concentration factors C ranging between 700 and 1300 suns. This absorber temperature value has been selected in order to comply with the expected aims of future solar tower plants (Mehos et al., 2017). All coatings show promising efficiencies, especially at high concentration factors. Both the porous $CCMO_4$ and the CCO_4 coatings feature higher efficiencies than Pyromark, including efficiencies above 0.92 at 1300 suns. This advantage is particularly useful when taking into account that both samples have greater thermal stability than Pyromark at such temperatures (Rubin, Chen, and Chen, 2019). It is also worth noting that, although both samples show similar solar absorptances within the experimental uncertainty, the efficiency of the CCO_4 coating is reduced by the greater thermal losses produced by its significantly higher total hemispherical emittance. This disadvantage is expected to grow even further because the CCO_4 sample is potentially susceptible to a reduction in solar absorptance upon aging, due to grain coalescence, whereas the porous sample remains more stable (Rubin, Chen, and Chen, 2019). Besides, the influence of hemispherical emittance increases at lower concentrations, which is expected to happen at times where the solar flux is not at its peak (such as the start-up phase).

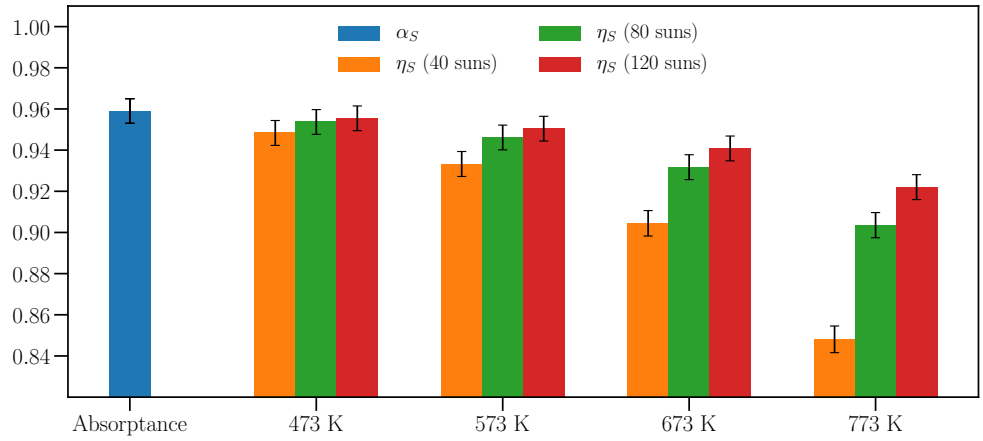

FIGURE 4.20: Solar absorptance (α_S) and conversion efficiencies (η_S) of WWWA Sample A for three solar concentration factors as a function of temperature. Error bars correspond to expanded uncertainty values ($k = 2$).

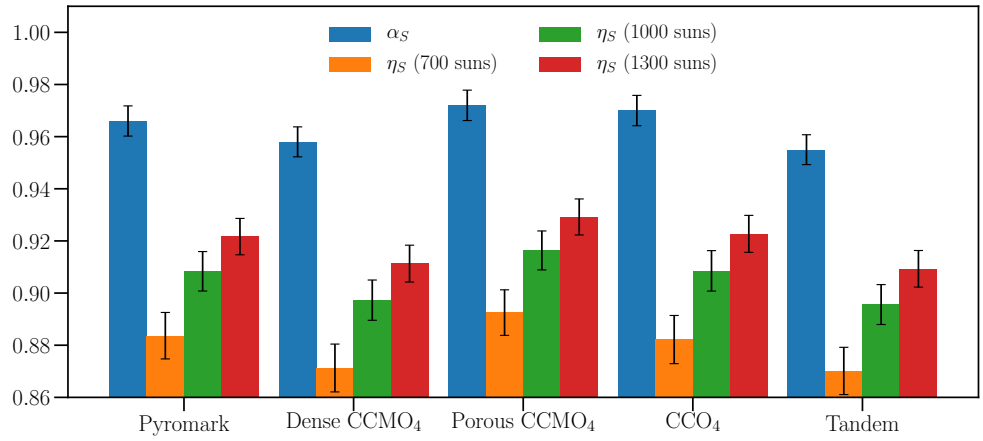

FIGURE 4.21: Solar absorptances (α_S) and conversion efficiencies (η_S) for three solar concentration factors at 1073 K for the five black coatings. Error bars correspond to expanded uncertainty values ($k = 2$).

4.4 Conclusions

High-temperature infrared emittance measurements have been performed for two sets of new solar absorber coatings developed with the aim of increasing the working temperature and lifetime of parabolic trough and solar tower CSP systems.

W/WAlN/WAlON/Al_2O_3 solar selective coatings feature promising selective properties and good thermal stability up to 773 K. By analyzing their optical properties, some interesting features have been observed. The temperature dependence of the directional spectral emittance of these materials has been found to be weak and stable in air in the desired temperature range. The influence of the optical properties of the top alumina layer have been interpreted by means of the Berreman effect. A semi-quantitative analysis of this phenomenon allowed an estimation of the frequency distribution of the amorphous LO phonon. Finally, differences between the total normal and total hemispherical emittances have been shown, which reveal the need to perform accurate characterizations of the whole angular response of the materials. These results also prove the reproducibility of the HAIRL emissometer and validate the total normal results by comparison to an additional measurement scheme (a hand-held emissometer).

Regarding the black spinel coatings, their thermal radiative properties are comparable or even better than those of Pyromark. Out of the four coatings with improved thermal stability, the porous $Cu_{0.5}Cr_{1.1}Mn_{1.4}O_4$ sample presents the best overall results and the highest solar conversion efficiency. This stems from its porous structure, which increases light-trapping and solar absorptance and also reduces the thermal emission at high angles. This type of structures could be further developed to tune the thermal radiative properties of materials. Overall, a combination of structural parameters and chemical composition is key to determining the emittance of these black coatings, as evidenced also by the influence of the substrate and the silica binder phase. This is also true for Pyromark, as revealed by a brief review of the considerable dispersion of literature data.

Chapter 5

Characterization of vanadium alloys for nuclear fusion

5.1 Introduction

Nuclear fusion power is a unique source of sustainable energy that relies on exploiting the immense amount of energy that is produced when hydrogen isotopes collide to form much more stable helium nuclei. Its raw materials are deuterium (^{2}H) and lithium, with no radioactive end-products. Both fuels can be considered plentiful resources when compared to the minute amounts required to power fusion plants (Ongena and Van Oost, 2012). Development of this energy source, which has remained at the forefront of international energy research policy for decades, has been repeatedly delayed. As a matter of fact, successful and commercially viable plasma containment is one of the most complex engineering tasks ever attempted, and each new advance reveals unforeseen challenges in materials design (Bloom, 1998).

Fusion reactors can be classified according to the method used to contain the plasma, which can be inertial (i.e., laser-based) or magnetic. The most promising structure to date seems to be the magnetically confined tokamak design, originally proposed by Soviet scientists in the 1950s. Several reactors have been built based on this concept, chiefly among them the Joint European Torus (JET), the largest plasma containment experiment to date. The next step consists of ITER, a larger tokamak which was originally planned in the 1980s as the first self-sustained reactor, for which the fusion of nuclei finally becomes the dominant plasma heating source (Bigot, 2017). Once this has been achieved, the DEMO project will hopefully bridge the gap between ITER and subsequent commercial fusion reactors somewhere around 2050 (Romanelli et al., 2012).

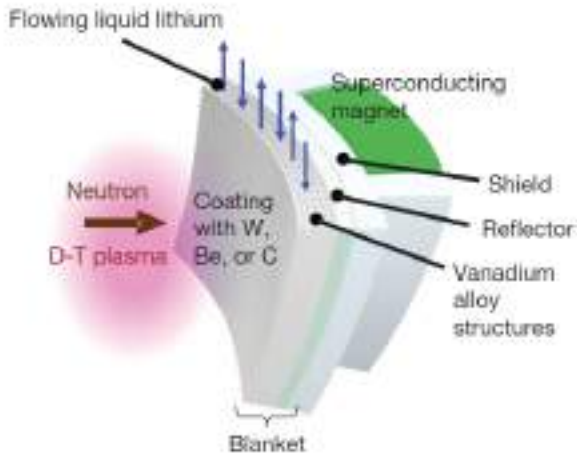

FIGURE 5.1: Schematic view of a nuclear reactor. Reproduced from Muroga, 2012 with permission by Elsevier.

An example of the complexity of a tokamak-type reactor wall is shown in Figure 5.1. The plasma is confined along the central ring of an evacuated toroid enclosed by a complex wall system consisting of several layers of structural materials. The plasma-facing first section is called the blanket. This is the most crucial part of the structure, the one which has the most stringent mechanical, thermal, and nuclear requirements, as well as the one that is most responsible for the thermal balance of the entire system (Končar et al., 2017; Nam et al., 2014).

Thus, the requirements of this monumental engineering task demand great efforts in materials science research. Due to these stringent design requirements, only a handful of materials are considered as candidate structural materials for the first wall/blanket, chiefly among them vanadium (Muroga, 2012; Muroga et al., 2014; Muroga, 2017). Due to its superior nuclear performance and high-temperature mechanical properties, the V-4Cr-4Ti alloy family has been selected as the leading candidate for structural designs which employ liquid Li as a cooling agent (Le Flem, Gentzbittel, and Wident, 2013; Chen et al., 2011; Zinkle et al., 1998). Among the requirements demanded for the materials used in the first wall/blanket environment, the most important ones are the conversion of the kinetic energy of neutrons into heat and the extraction of that heat to generate power (Raffray et al., 2002).

Therefore, accurate data of the radiative properties at working temperatures become necessary as input parameters for numerical simulations to optimize thermal processes by heat transfer calculations (Končar et al., 2017; Nam et al., 2014). This is particularly important for systems that are used under high vacuum conditions, such as nuclear reactors, where heat transfer occurs mainly by radiation. Proof of this importance are the significant efforts devoted to the thermal radiative characterization of candidate materials for fission reactors (Cao et al., 2012; Ruset et al., 2017; Keller et al., 2015; Hunnewell et al., 2017; King et al., 2017; King et al., 2018). Besides, thermal radiative data of these materials are also applicable for non-contact temperature measurements and for the accurate use of infrared thermography as a non-destructive testing technique in these applications (Lott et al., 2010; Hernandez et al., 2008; Seki et al., 2010; Zhang et al., 2018b).

No data on the radiative properties of vanadium-base alloys can be found in the literature. There is some data corresponding to pure vanadium, such as spectral emissivity measurements in the visible and near infrared ranges, as well as total hemispherical emissivity data (Stanimirović, Vuković, and Maglić, 1999; Pottlacher et al., 2007; Paradis et al., 2002; Cheng et al., 1987). Optical constants data in the visible/near-infrared region are also available (Johnson and Christy, 1974; Ordal et al., 1985). Nevertheless, data reported for pure metals cannot generally be used to accurately estimate the properties of their alloys, as optical properties can vary strongly with even minor compositional differences, and especialy in the presence of secondary phases (Roger, Yen, and Ramanathan, 1979; Makino and Kunitomo, 1977). This reveals an important defficiency in the thermophysical characterization of vanadium alloys and the need to perform further studies on their radiative properties.

Taking all the above into consideration, this Chapter introduces an original study on the thermal radiative properties for two vanadium-base alloys for fusion reactors: the standard V-4Cr-4Ti and a reinforced V-4Cr-4Ti-1.8Y-0.4Ti_3SiC_2 (mass%). A complete study of the microstructure of both alloys has been done elsewhere (Fu et al., 2013; Wynne et al., 2016; Zheng et al., 2014). The most effective additional components are Y, which was selected as an oxygen scavenger to deplete the metal of dissolved interstitial elements (mainly O), and Ti-based intermetallic nanoparticles, which have been observed to be useful for pinning down dislocations for improving mechanical properties (Wynne et al., 2016; Zheng et al., 2014). The main goal of this study is to provide reliable data for accurate heat transfer simulations of fusion reactors, as wel as non-contact temperature measurement and testing methods.

5.2 Materials and methods

5.2.1 Sample synthesis and processing

Samples of two alloys of the V-4Cr-4Ti family were studied: the base alloy and a special one with additional 1.8% Y and 0.4%Ti_3SiC_2 (mass %). Two samples of the former composition were synthesized by electron beam melting (EBM) and processed by hot rolling at 1173-1323 K, cold rolling at room temperature and annealing at 1293 K to remove inner stress. Two samples of the latter were synthesized by mechanical alloying (MA) and eventually processed by hot isostatic pressing under 150 MPa at 1373 K. Moreover, in order to investigate the thermal stability of the microstructure and its effect in the thermal radiative properties, one sample of each alloy was heat-treated inside an alumina crucible under vacuum performed by a turbomolecular pump ($4 \cdot 10^{-5}$ hPa). The V-4Cr-4Ti sample (EBM-HT) was heat-treated for 2 hours at 1273 K, whereas the V-4Cr-4Ti-1.8Y-0.4 Ti_3SiC_2 sample (MA-HT) was treated for 2 hours at 1473 K. A Zr foil was used as an oxygen getter in both cases. Table 5.1 shows the characteristics of each sample and the acronyms used for each sample in this paper. Samples were mechanically polished with P800 SiC paper to ensure a reproducible surface since emissivity values can be strongly dependent on the surface roughness (Equation 2.23). Surface roughness parameters were measured with a mechanical profilometer (Mitutoyo SJ-201 roughness tester), and are shown in Table 5.2.

TABLE 5.1: Summary of the compositions, heat treatments and acronyms of the vanadium alloys.

Sample	Synthesis	Heat Treatment	Acronym
V-4Cr-4Ti	Electron Beam Melting	No	EBM
V-4Cr-4Ti-1.8Y-0.4Ti_3SiC_2	Mechanical Alloying	No	MA
V-4Cr-4Ti	Electron Beam Melting	2 h (1273 K)	EBM-HT
V-4Cr-4Ti-1.8Y-0.4Ti_3SiC_2	Mechanical Alloying	2 h (1473 K)	MA-HT

TABLE 5.2: Surface roughness parameters of the vanadium samples, as defined in Section 2.1.3.

Sample	R_a (μm)	R_q (μm)	R_z (μm)
EBM	0.11	0.14	0.85
MA	0.16	0.24	1.55
EBM-HT	0.09	0.11	0.76
MA-HT	0.14	0.18	1.16

5.2.2 Microstructural characterization

Optical and electron microscopy techniques were used to investigate the microstructure. Scanning electron microscopy (SEM) and electron back-scattered diffraction (EBSD) measurements were done in a TESCAN Mira3 XMH field emission gun microscope equipped with an Oxford Instruments Aztec system and operated at 20 kV using a step size of 0.2 μm. Additionally, transmission electron microscopy (TEM) was employed to study the size and distribution of precipitated secondary phases. X-ray diffraction patterns were acquired using Cu K_α radiation in Bragg-Brentano geometry with an angle step of 0.02° in an X'Pert-Pro diffractometer. Finally, X-ray photoelectron spectroscopy (XPS) depth profiles were done with Ar^+ sputtering in a SPECS system equipped with a Phoibos 150 1D-DLD analyzer and a monocromatic Al K_α source. Depth values were determined by comparison to a Ta_2O_5 reference. The ion energies and current applied were 3000 and 5000 eV and 10 mA, respectively.

5.2.3 Emissivity measurements

The emissivity measurements were made using the HAIRL emissometer, as described in Chapter 3. Directional spectral emissivity measurements were performed between 473 and 1073 K every 100 K, as well as at the maximum expected working temperature of 1023 K. A first thermal cycle up to 1023 K was performed previously to allow for stabilization of the material. The sample temperature was measured by two Type K thermocouples located in holes machined through the material by wire electrical discharge machining. The sample chamber reaches a base pressure of $1.5 \cdot 10^{-4}$ hPa. In the case of V-based alloys this vacuum level might not be enough to entirely avoid high temperature oxidation and oxygen diffusion in the metallic matrix (Natesan

and Uz, 2000). To minimize this effect, all measurements were performed using a Zr foil as an oxygen getter.

5.3 Results and discussion

5.3.1 Microstructural characterization

The results of the optical and electron microscopy characterization are shown in Figure 5.2. Figure 5.2a shows an optical micrograph of the EBM sample, with equiaxed grains of 37.8 μm average diameter, similar to the grain sizes reported in Fu et al., 2013. This reference reports grain growth of the small amount of Ti/Cr-carbides present in this sample and the complete solution of the metallic elements are expected upon heat treatment at 1273 K for 2 h applied in the current work, but with no change in the grain size of the matrix (Fu et al., 2013).

In the case of the MA and MA-HT samples, SEM micrographs are shown in Figures 5.2b and 5.2c, respectively. The color maps correspond to crystallographic orientations of the grains, as measured by EBSD. It was observed that in the MA sample there is a bimodal grain size distribution (Figures 5.2b and 5.2d) with some large grains together with a large population of fine grains. After heat treatment, growth in the average grain size is observed, together with a homogenization of the size distribution (with no abnormally large grains observed in Figure 5.2c). The EBSD results allow assigning a crystallographic orientation to each grain, and thus the grain size statistics. However, it is important to distinguish sub-grain boundaries from real grain boundaries when calculating average grain sizes. Thus, the grain size distribution analysis reported in Figure 5.2d has been determined taking into account a 15° misorientation threshold for high-angle grain boundaries. An inset is included to show the low number of large grains present in the MA sample. Then, a bright-field transmission electron microscopy (TEM) image of the MA-HT sample is presented in Figure 5.2e. As reported for another set of V-4Cr-4Ti nanoparticle-strengthened alloys, the concentration of nm-sized precipitates increases upon heat treatment (Zheng et al., 2014).

X-ray diffraction (XRD) patterns obtained for all the samples are shown in Figure 5.3, together with suggested indexations of all observed peaks to known phases that occur in this alloy family. On the one hand, in the case of the EBM and EBM-HT samples, the reflections corresponding to the metallic solid-solutions were the most intense, although a small amount of carbide

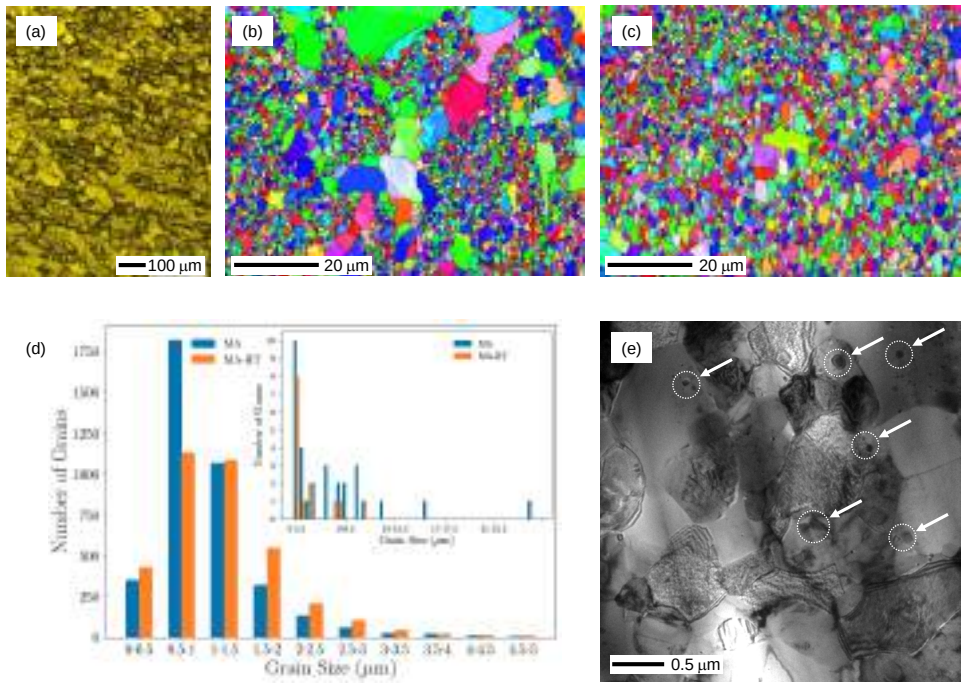

FIGURE 5.2: (a) Optical micrograph of the EBM sample. SEM micrographs and EBSD misorientation maps for (b) the MA sample and (c) the MA-HT sample. (d) Grain size distribution for MA and MA-HT. (e) Bright-field TEM image of the MA-HT sample with precipitates highlighted.

precipitates was also observed, in agreement with Fu et al., 2013. These are the two diffractograms that show the greatest difference, particularly around the regions corresponding to solid solution reflections. In the case of the EBM sample, reflections corresponding to the (V) solid-solution[1] together with those from two other body-centered-cubic solutions were indexed, which after the heat treatment merged in a single (V) solid-solution in the EBM-HT sample. Besides, there was a slight increase in the intensity of the reflections attributed to carbides ($VC_{0.5}$, TiC, $Cr_{23}C_6$) upon heat treatment. On the other

[1]Metallic solid solutions with similar crystallographic parameters to those of an elemental metal M are called (M).

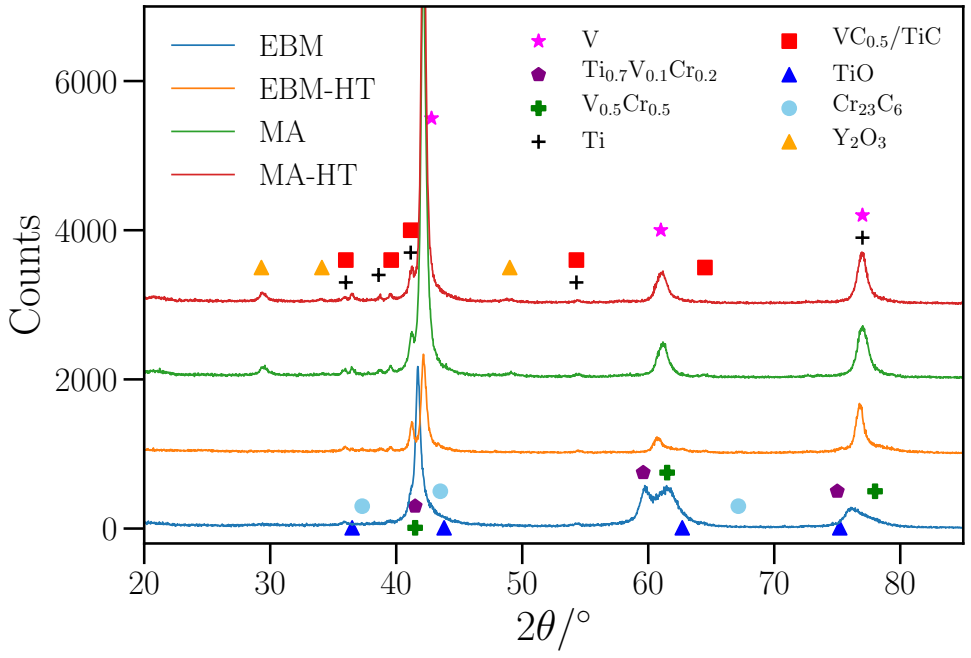

FIGURE 5.3: Room-temperature X-ray diffraction patterns of the four samples. The indexation of the reflections shows the presence of several phases in each sample.

hand, for both MA and MA-HT samples, in addition to the reflections of the (V) matrix, those corresponding to the nanoparticle reinforcements (primarily Y_2O_3 coming from the oxidation of the added Y) are also present. In the case of the MA-HT sample, the intensity of Y_2O_3 reflections is slightly higher. The occurrence of precipitates in these materials and their evolution with heat treatment is important for the discussion of the differences in the properties of the alloys.

Regarding the extent of oxidation of the samples, efforts were made to reduce it as much as possible, due to the well-known oxygen affinity and solubility of vanadium alloys (Natesan and Uz, 2000). However, a slight golden hue was observed after the emissivity measurements in all four samples. In order to analyze the potential influence of this surface oxidation on the emissivity data, the oxide layer was initially characterized by grazing-angle XRD. XRD patterns were acquired at small angles (2, 5, 10, 15 and 50° with respect

to the sample surface) with the purpose of enhancing the contribution of the oxide layer, but only the phases shown in Figure 5.3 for the standard Bragg-Brentano geometry were observed. This rules out the possibility of a thick oxide layer. Then, taking advantage of the presence of a region that had not been in contact with the atmosphere (a masked area at the corner of the sample) and using atomic force microscopy, it was observed that there was no step at the boundary between the oxidized area and the metallic area. This is consistent with an internal mode of oxidation, with residual oxygen in the sample chamber atmosphere diffusing into the bulk of the metal (Natesan and Uz, 2000).

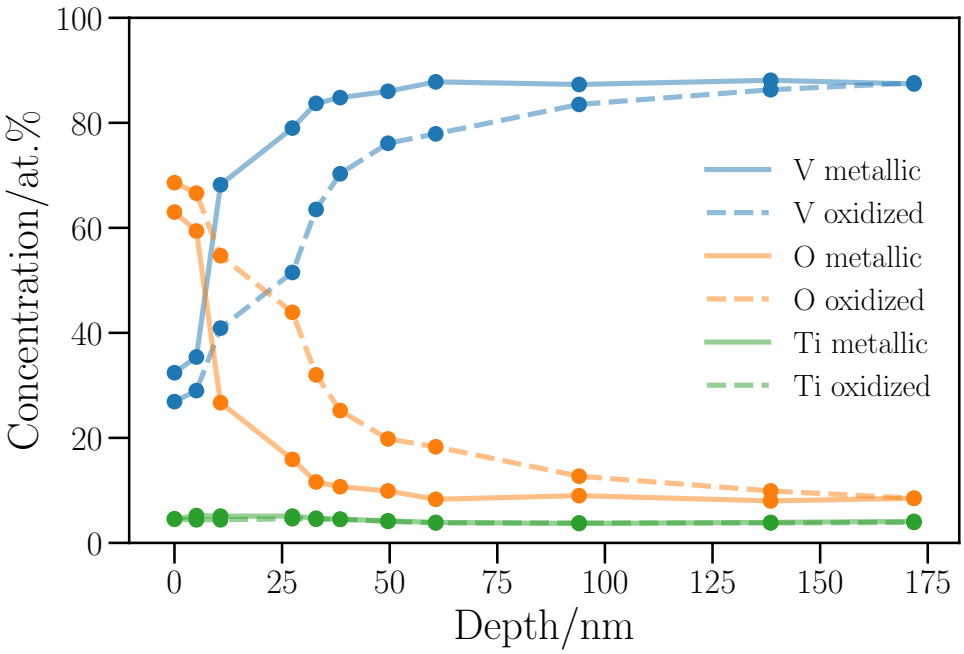

FIGURE 5.4: X-ray photoelectron spectroscopy (XPS) depth profiles of V, Ti, and O for metallic (continuous lines) and oxidized (dashed lines) sections of the surface.

Finally, to determine more accurately the extent of oxygen penetration, X-ray Photoelectron Spectroscopy (XPS) depth profiles were acquired in both the oxidized and masked areas. Figure 5.4 shows a semi-quantitative estimation of the ratios between the integrated signals corresponding to V, Ti and

O. Other minority elements such as Cr, N and C were also detected, but were not deemed relevant for this purpose and were not computed for the total intensity. Ti was included because of the observed surface segregation of this element in vanadium alloys in vacuum (Hatano et al., 2005). The metallic area (continuous lines) showed a native oxide layer of 5 nm (V/O ratio of 1:2) and an oxygen penetration layer of approximately 20 nm below the oxide-metal interface. In the case of the oxidized region, these thickness values are approximately 15 nm and 125 nm, respectively. Beyond 140 nm, the oxygen content in both samples is the same as in the bulk. In both cases, the V/O ratios of the oxide layers suggest a VO_2 composition, which is expected for oxidation of V-4Cr-4Ti alloys in vacuum (Natesan and Uz, 2000). An intermediate region can also be defined at around 30 nm into the oxidized material, where the V/O ratio reaches a value of 1:1 and a potential VO composition. Although the Ti content in the alloy is small, due to its higher oxygen affinity compared with V, surface segregation of Ti was observed for the same alloy at similar conditions (Hatano et al., 2005). This leads to a detectable amount of stable TiO_2 in addition to V oxide in this first layer. In any case, the oxide layer is only slightly thicker than the native one and several orders of magnitude smaller than the infrared wavelengths studied, so it is assumed to bear little influence on the thermal radiative properties of these alloys.

5.3.2 Emissivity measurements

The samples were subjected to two thermal cycles in the HAIRL emissometer between 473 and 1023 K. In the first cycle, possible surface tensions created during polishing were eliminated (del Campo et al., 2006a). Once the surface tensions were assumed to be relieved, a systematic emissivity study was performed from 10 to 80° and between 3 and 22 μm. The low-wavelength limit was restricted to 3 μm, as the specularity of the samples at the usual 2 μm limit was unsatisfactory (as computed by Equation 2.23 using data from Table 5.2). This ensures that the values reported are representative of the materials, with as little influence of the surface state as possible. Nevertheless, the roughnesses reported in Table 5.2 are similar to the ones expected for structural alloys in nuclear power plants, and significantly below the range where their mid-infrared emissivities are strongly influenced (King et al., 2017).

The temperature-dependent normal spectral emissivities of the four alloys are shown in Figure 5.5. Shades corresponding to the expanded uncertainty ($k = 2$) are shown together with the data, in this figure and thereafter.

The data also show weak spectral features corresponding to absorption by residual water and CO_2 in the blackbody optical path. The emissivity curves show the typical metallic behavior with low emissivity values that increase with temperature and decrease with wavelength. As it can be seen from the evolution of the emissivity for both HT samples, the EBM-HT alloy presents stronger temperature dependence than the MA-HT one, which can be associated with the instability of its microstructure, which is prone to precipitation of carbides (Fu et al., 2013). This would indicate that, similarly to the mechanical properties, the radiative properties of this improved alloys are also more stable than those of the original ones (Wynne et al., 2016; Zheng et al., 2014).

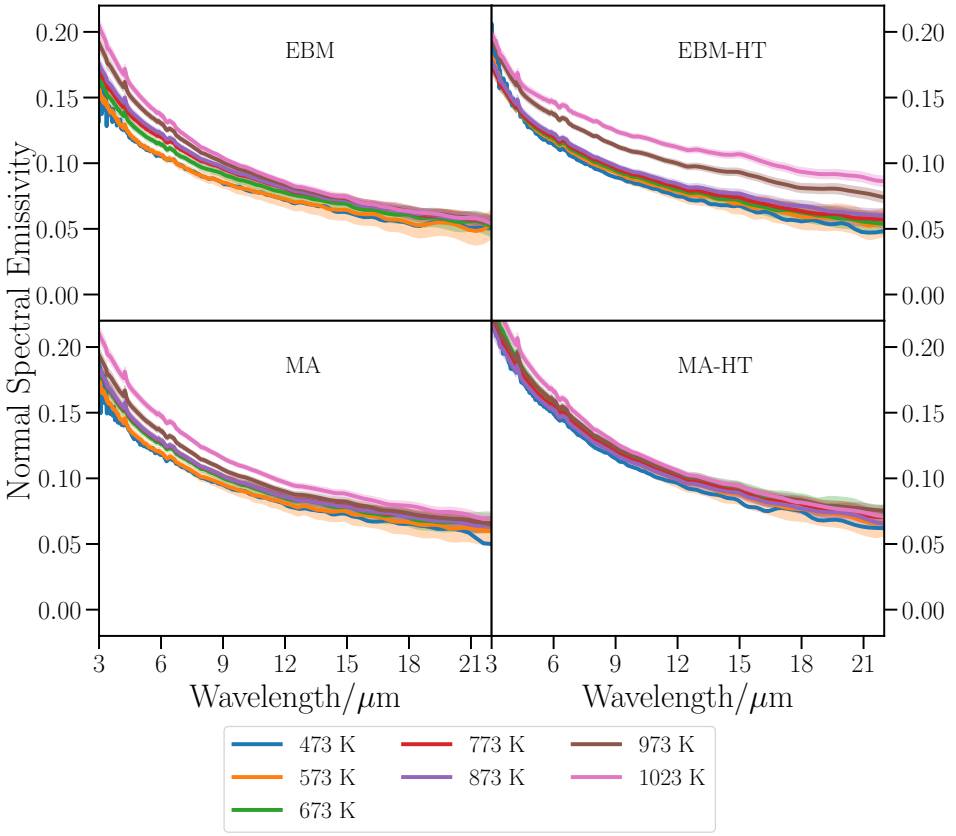

FIGURE 5.5: Temperature dependence of the normal spectral emissivities of the four V-4Cr-4Ti-based samples. Shaded regions correspond to expanded uncertainty values ($k = 2$).

Figure 5.6 shows a comparison between normal spectral emissivity measurements of heat-treated and untreated samples for each alloy at low (473 K) and high (973 K) temperatures. This comparison allows a greater insight into the behavior of the thermal radiative properties of these materials. First, regarding the EBM-type samples, a clear difference can be observed between their low-temperature curves and their high-temperature versions. Both alloys show similar emissivity values at most wavelengths at 473 K, but they grow apart considerably at higher temperatures. While the short-wavelength emissivities of both alloys increase in a similar vein, only the EBM-HT sample shows important increases in the long-wavelength portion of the spectrum. Secondly, regarding the MA-type samples, a significantly different behavior is observed. Both samples show temperature dependence mostly confined to the short-wavelength range of the spectrum, but it is much higher in MA than in MA-HT, which had already been declared the most temperature-independent sample. Interestingly, the high-temperature MA results and those of the low-temperature MA-HT are similar, which may indicate that the effects of heat treatment are partially taking place at lower temperatures.

In addition to the tendencies observed for normal spectral results, the directional dependences also need to be analyzed. Figure 5.7 shows directional spectral emissivity measurements at 973 K for all four samples. Similar to what is observed in Figure 5.6, the biggest evolution between EBM and EBM-HT samples at short angles occurs more at long wavelengths than at short ones. However, from 50° onwards, the EBM-HT spectra become parallel to the EBM spectra. MA and MA-HT samples also show the same type of behavior as in Figure 5.6 at small angles, but at 70 and 80° both curves are parallel. With the only anomalous exception of the 60° curve, the emissivity results of the EBM and MA samples are very close, despite their differences in composition and roughness. This hints at the great role played by the secondary phases precipitated by heat treatment. Finally, in the case of both HT samples, the EBM-HT emissivity is higher than the MA-HT one at all angles except 10°.

An additional representation of the angular dependence of the emissivities of these alloys at 973 K is presented in Figure 5.8, where the results are shown as a function of angle for three discrete wavelengths. The alloys clearly follow the standard metallic behavior, where the emissivity slightly varies at low angles up until 50°, increases up more rapidly until it reaches a maximum between 70 and 85° and then drops down to 0 at 90°, as required by electromagnetic boundary conditions (Howell, Mengüç, and Siegel, 2010). The lines connecting the dots are made by a spline and only help showing where

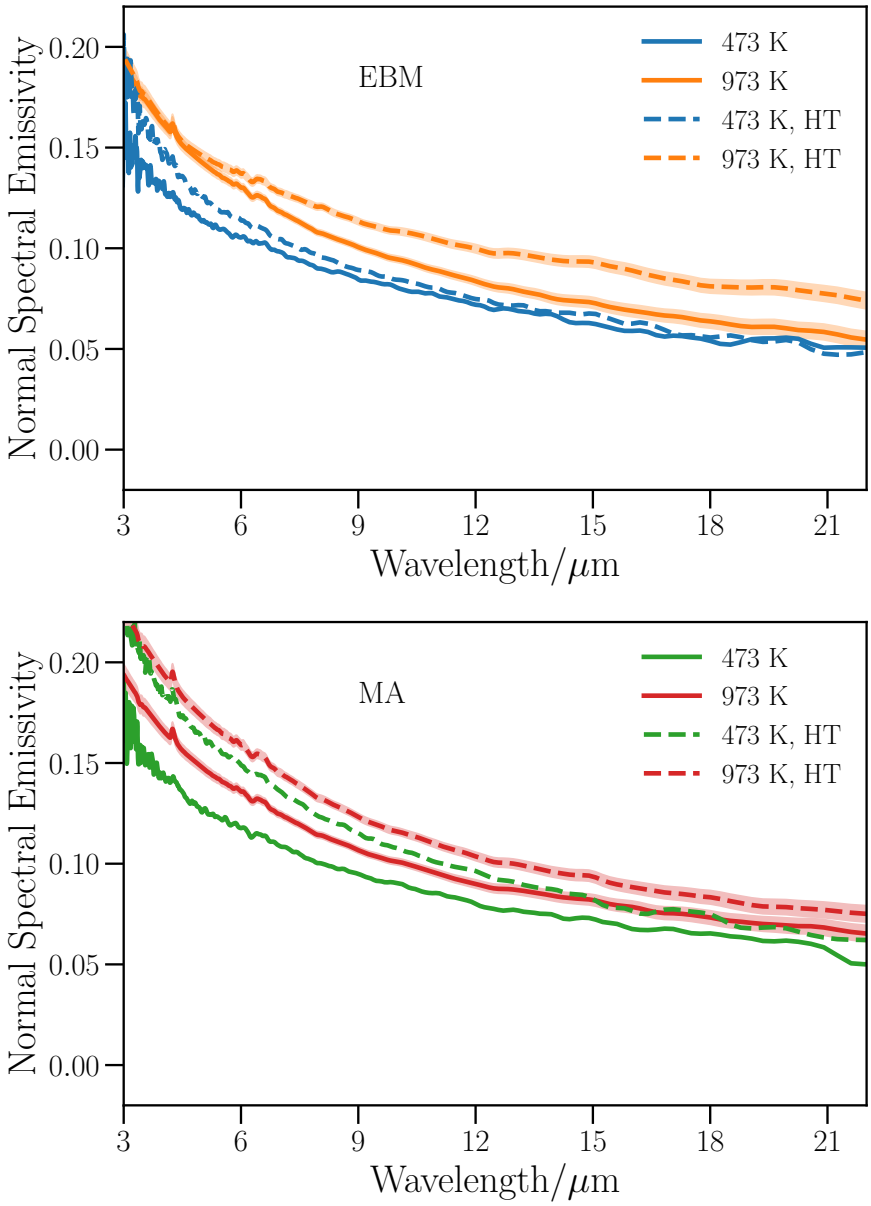

FIGURE 5.6: Normal spectral emissivity measurements for both alloy compositions at low (473 K) and high (973 K) temperatures. Dashed lines correspond to the heat-treated (HT) versions. Shaded regions correspond to expanded uncertainty values ($k = 2$).

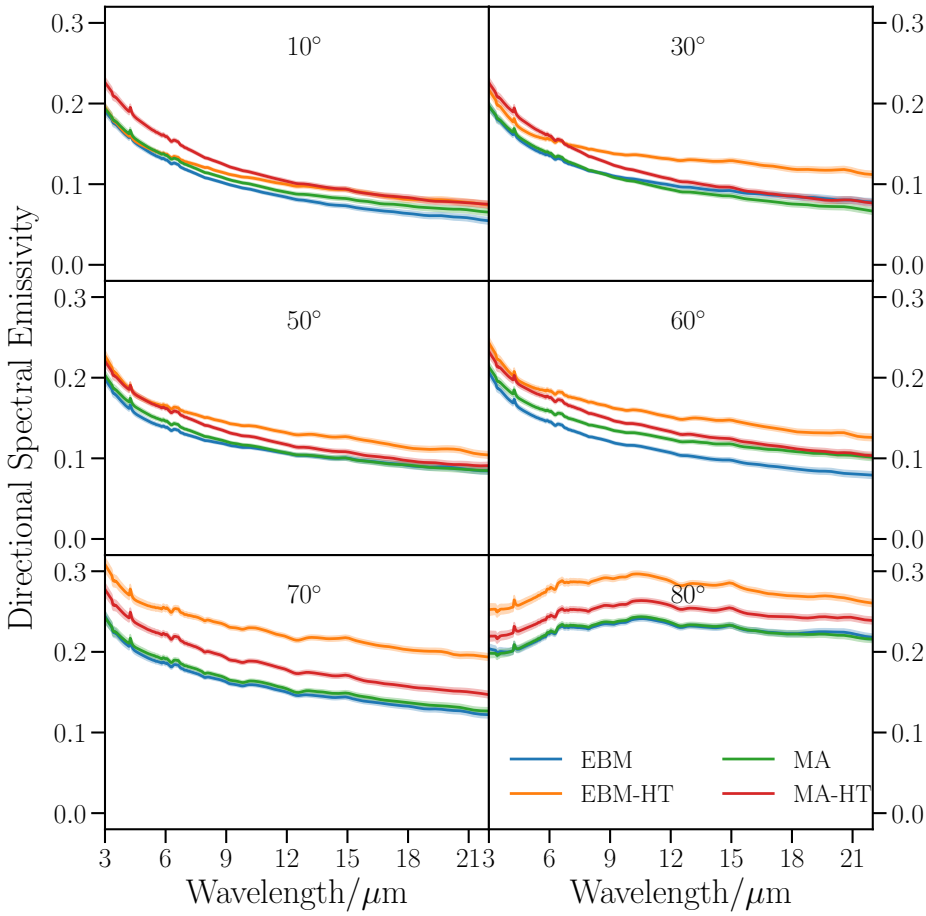

FIGURE 5.7: Directional spectral emissivity measurements at 973 K for all samples at different angles. Shaded regions correspond to expanded uncertainty values ($k = 2$).

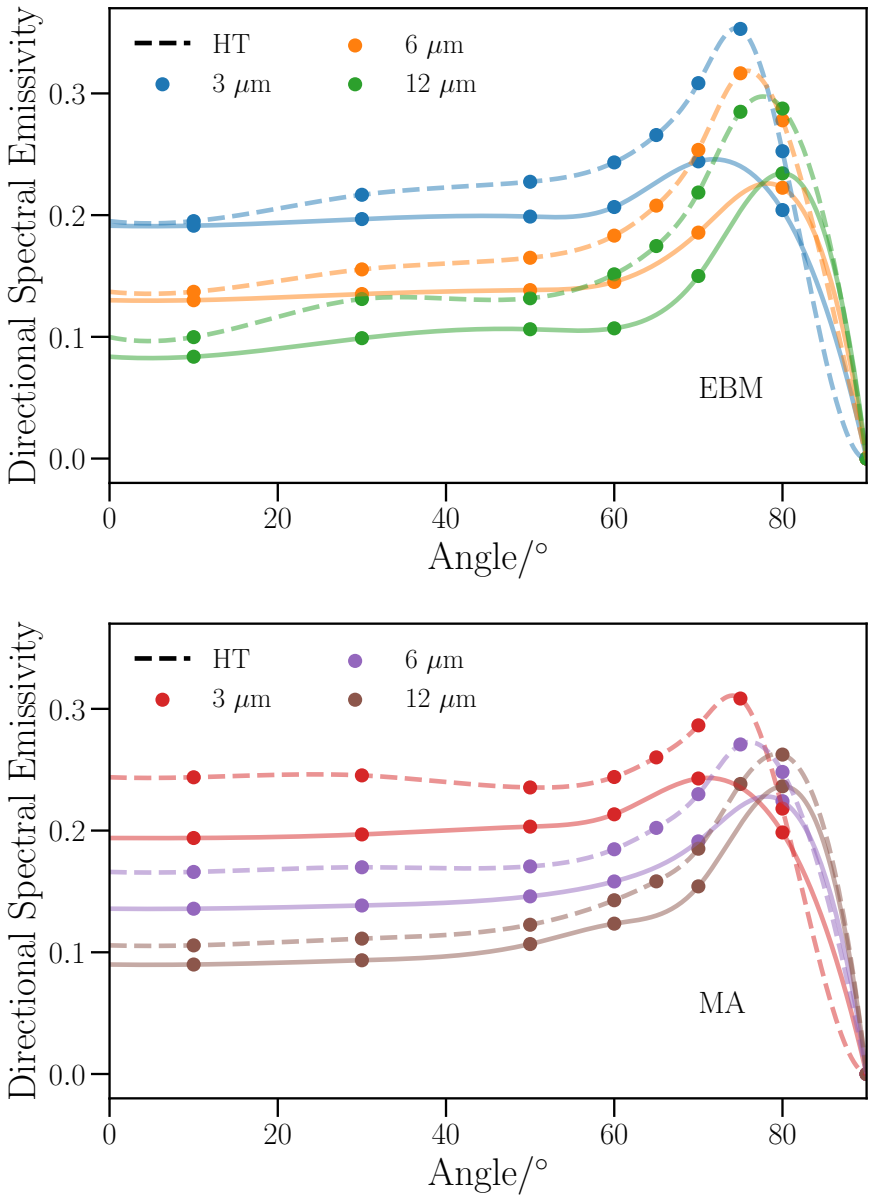

FIGURE 5.8: Angular dependence of the directional spectral emissivities at 973 K at discrete wavelengths for both sets of untreated (continuous lines) and heat-treated (dashed lines) samples.

these emissivity maxima might be situated. Once again, it can be seen that heat treatment induces an emissivity increase at all angles and wavelengths for both compositions, although it does not change the metallic behavior of the directional emissivity. It is important to note that the HT samples have been measured at two additional angles, so the shapes of the curves are not always entirely comparable. Nevertheless, the addition of these additional directional data does not add any significant bias to the total hemispherical calculation, as the $\cos\theta \sin\theta$ weight factor in the directional integral (Equation 2.9) is reduced at both extremes of the polar angle range.

An explanation of the differences between the measured emissivity curves requires knowledge of the microstructure. The microstructural analysis reported above and the ones performed in previous works (Wynne et al., 2016; Fu et al., 2013) have concluded that significant microstructural evolution occurs in these alloys during thermal processing. Some observed phenomena include grain growth of secondary phases (mainly carbides), increase of the concentration of nm-sized precipitates, take-up of residual interstitials (O, N) from the imperfect vacuum, and even abnormal grain growth of the (V) matrix. These microstructural changes reveal themselves in changes in the physical properties of these materials, such as the hardnesss. The observed evolution of the emissivity with heat treatment suggests that these changes may also influence their optical and radiative properties.

Figure 5.9 shows the results of the fitting of all normal spectral emissivities to the Drude model (Equation 2.34) at 973 K. Fittings have been made using the free FOCUS software (De Sousa Meneses, 2020). The spectra are plotted against wavenumber to better appreciate their approximate $\omega^{1/2}$ spectral dependence (as suggested by Equation 2.39). It can be seen that all four samples fit a simple Drude expression accurately, which allows extracting some useful parameters for the analysis of the microscopic origin of their differences. This is achieved by comparing the main results of the fitting for each sample, as shown in Figure 5.10. The effective electrical conductivity (Equation 2.43) has been reported because of the dispersion of values obtained for ω_p and γ. By combining both phenomenological parameters into a single one, the comparison of the samples becomes easier. The other reported parameter is the high-frequency dielectric constant ϵ_∞, which characterizes in a broad manner the near-infrared response of the material and all non-Drude contributions. Literature data for both parameters are also shown for comparison (Smith et al., 1995; Cheng et al., 1987). It can be seen in Figure 5.10 that all samples feature effective conductivities that are similar to the value reported by Smith et

al., 1995 (at 873 K), but all residual dielectric constants are many times higher than the one reported for pure V in Smith et al., 1995. As discussed above, this is expected because of the complex microstructure of these alloys, in comparison with pure vanadium. An explanation for the enhanced dielectric response can be found, for example, in the presence of secondary dielectric phases in the form of nanoparticles, as evidenced by the microstructural characterization shown in Figures 5.2 and 5.3.

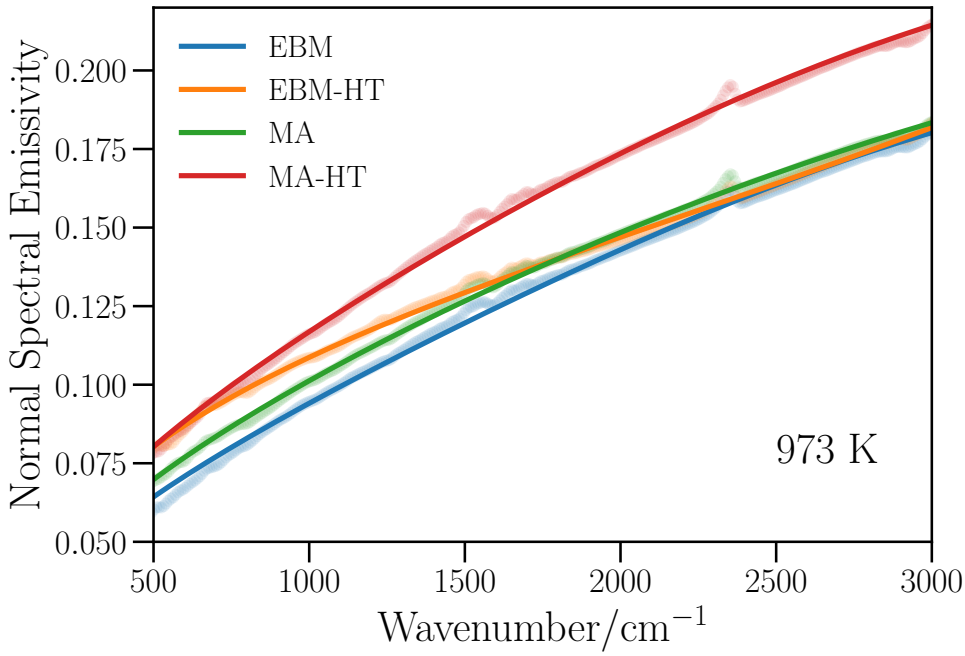

FIGURE 5.9: Normal spectral emissivities of the four samples at 973 K fitted to the Drude model (Equation 2.34).

Some tendencies can be observed by comparing the fitting results for each sample and its heat-trated version. In both cases, the obtained values for both parameters decrease after thermal processing, although in a different manner. This change is much more pronounced in the EBM set of samples, where the conductivity is reduced by half, and the dielectric constant by an order of magnitude. An explanation may be found in Fu et al., 2013, where it is observed that cold working during processing produces precipitation of coarse Ti-Cr oxocarbonitrides along grain boundaries. This is detrimental to

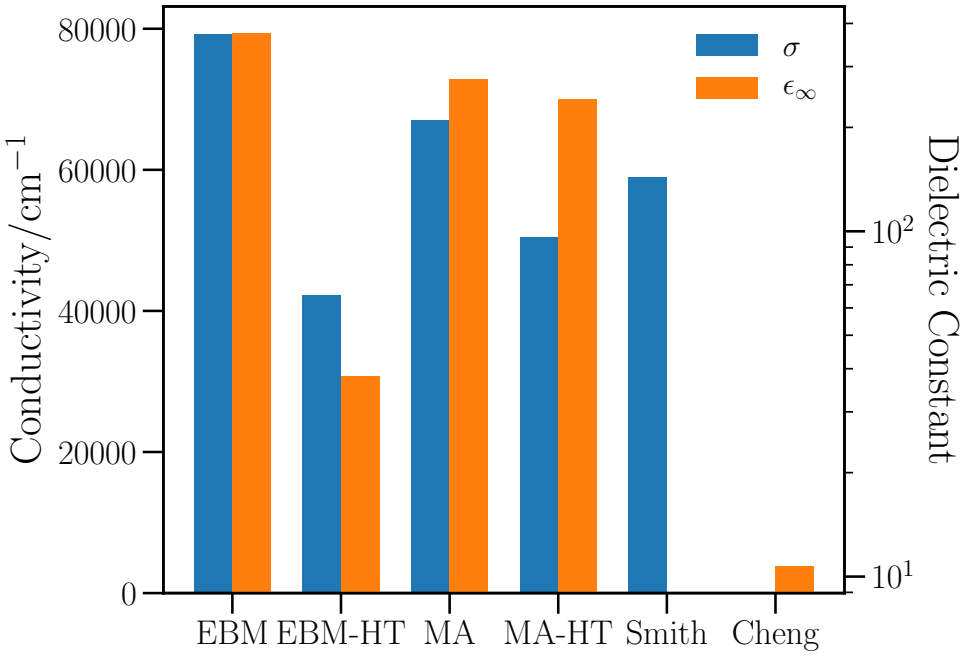

FIGURE 5.10: Results of the Drude fitting parameters at 973 K, compared to literature data on the electrical conductivity at 873 K (Smith et al., 1995) and the high-frequency dielectric constant of pure V (Cheng et al., 1987).

the mechanical properties of the material, but it also means that the matrix is relatively depleted of impurities. This can explain the high conductivity of the EBM sample, while the large number of coarse dielectrics may induce a greater ϵ_∞. However, aging treatments at high temperature reduce the number of coarse precipitates and increase heavily the concentration of nm-sized precipitates inside the grains, which may reduce the conductivity while also featuring a weaker dielectric response. In the case of the MA set of samples, however, the changes are less significant. This can be explained by the fact that the main secondary phases in these alloys have been added during synthesis to provide structural stability, and thus are not expected to evolve much. However, an important microstructural evolution of unclear origin after HT at 1473 K has been found to significantly increase the hardness of this material (Wynne et al., 2016). Possible hypotheses involve either precipitation

of secondary phases or the take-up of residual gases in the vacuum chamber at such temperatures, either of which could explain the decreases in both fitted parameters. Interestingly, these relatively minor changes (compared to the EBM set) translate into much larger emissivity changes due to their influence upon the NIR emissivity, which is the most important emissive region at high temperatures. This analysis can help to shed some light onto the mechanisms behind the factors influencing the thermal radiative properties of multi-phase alloys. Nevertheless, the complexity of the microstructures, lack of strong spectral features, and range of temperature- and angle-dependent properties observed make a more in-depth interpretation of these results difficult.

Finally, the spectral directional results were integrated in order to obtain the total hemispherical emissivity, which is required for heat transfer calculations and thermal simulations of tokamaks. The integrated total hemispherical results are shown in Figure 5.11. The total hemispherical emissivity values increase with temperature in a quasi-linear manner and roughly parallel to one another, with the exception of the large increase at the highest temperatures for the EBM-HT sample, similarly to what was already observed in Figure 5.5. It is worth noting that differences between samples are statistically significant, which justifies the need to characterize the full range of samples and compositions. No data for these alloys is available for comparison, but electrical resistivity data of V-4Cr-4Ti between 673 and 873 K obtained in Smith et al., 1995 are used to calculate the total hemispherical emissivity using Equation 2.42. The predicted values for the available temperature range are depicted in purple squares in Figure 5.11, while the extrapolated dashed line is obtained by assuming a linear temperature dependence for the electrical resistivity. The qualitative agreement between the direct emissivity measurements and the theoretical prediction from resistivity data is very good. This was expected from the good fitting of the normal spectral data to the Drude expression in Figures 5.9 and 5.10. Quantitative differences can nevertheless be observed between the five data sets. The predicted data, which is reported for a basic V-4Cr-4Ti composition, lies between both studied EBM-type samples (which share the same composition), although it resembles the MA data the most. Finally, it is clearly seen that both set of samples present a higher total hemispherical emissivity when the heat treatment is performed, as has been shown throughout this Section. Thus, an important conclusion is that exposure to temperatures beyond the $973-1023$ K working temperature limit enhances the emissivity of the alloys, which can be useful for improving their radiative heat transfer capacity in overheating conditions. More generally, it

is shown that the thermal radiative properties of alloys can be tuned by heat-treatment and microstructural changes.

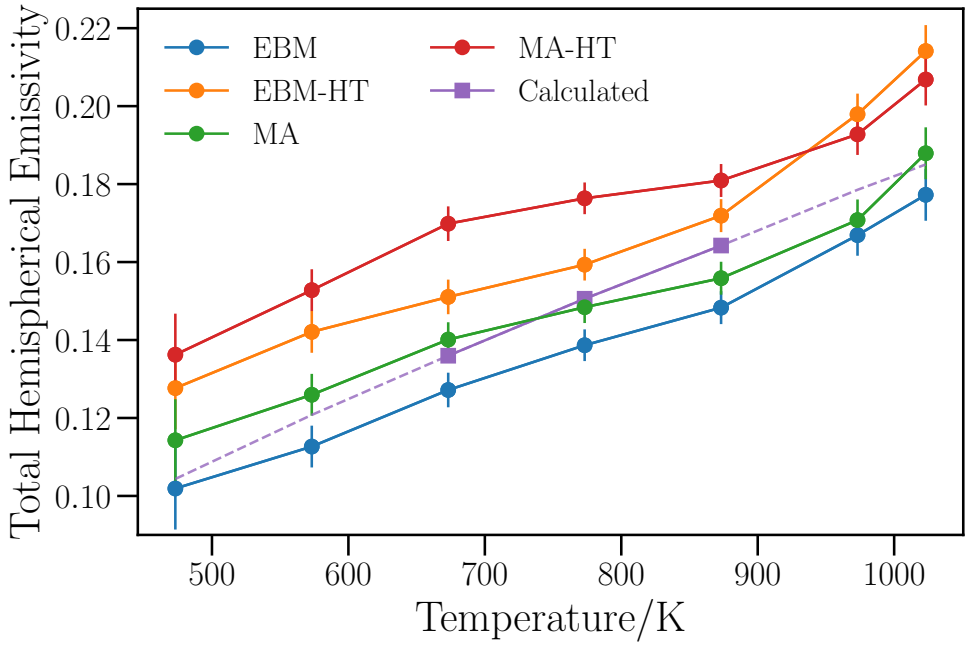

FIGURE 5.11: Total hemispherical emissivity for all four samples between 473 and 1023 K. Calculated data usind electrical resistivity measurements reported in Smith et al., 1995 are shown as squares. Extrapolated values are shown as a dashed line. Error bars correspond to expanded uncertainty values ($k = 2$).

Lastly, it is important to compare the obtained values with reference data. Thermal budgets assume emissivity values of $0.25 - 0.35$ for structural materials in the thermal budgets of both DEMO and ITER (Končar et al., 2017; Nam et al., 2014). In contrast, not even the highest-emitting sample under study features a total hemispherical emissivity larger than 0.22 at any feasible temperature. Although these estimates take into account also steel-based alternatives to V-4Cr-4Ti, it is unlikely that they are representative of those materials either (Roger, Yen, and Ramanathan, 1979). Finally, reported data for pure vanadium lie below 0.1 for most temperatures of interest (Cheng et

al., 1987), which means they are not useful for predicting the behavior of these alloys. This highlights the importance of providing reliable direct emissivity data for the application of vanadium-base alloys.

5.4 Conclusions

The thermal radiative properties of two alloys of the V-Cr-Ti family have been studied from 473 to 1023 K, which spans the entire working temperature range expected for these alloys in future fusion reactor designs. Two compositions and synthesis methods have been investigated, as well as the effects of heat treatment on the microstructure of the alloys. A combination of theoretical fitting of emissivity data and an extensive microstructural study, combining XRD, XPS, and several microscopy techniques, has allowed for an understanding of the evolution of the thermal radiative properties. The presence and evolution of precipitated secondary phases and interstitials dissolved in the (V) matrix are the main mechanisms behind the observed emissivity changes. Finally, the radiative heat transfer capability of each sample has been evaluated through its integrated total hemispherical emissivity. It has been shown that heat treatment and exposure to high temperatures lead to an increase in this parameter and an improved self-refrigerating capability for both alloys. Nevertheless, all the obtained values lie significantly below those assumed by the thermal budgets of future fusion reactors. Overall, these data are crucial thermophysical parameters for calculations of heat flow and temperature measurement inside the reactor; thus, this work helps to fill a deficiency on the thermophysical characterization of structural materials for these reactors.

Chapter 6

General conclusions

Over the course of this Ph.D., I have endeavored in several research lines concerning the measurement of thermal radiative and optical properties of materials. A selection of topics has been included in this thesis, within the framework of materials science in the field of alternative energies.

There are two main takeaways of this work. First, emissivity measurements still constitute a tough experimental challenge. Despite important developments and active research at the metrological level, emissivity characterization procedures at standard research laboratories have not been fully developed yet. Even though the work carried out during these 4 years is insufficient to guarantee the highest standards of quality for emissivity measurements with the HAIRL device, it is still a significant improvement from the previous stage, particularly with regards to the uncertainty calculations. Secondly, it has also been shown that the procedures required for accurate emissivity characterization of new materials for energy applications are often more complex than usually assumed. The dependences of emissivity on temperature, angle of emission, wavelength, and state of the material are all crucial for a proper understanding of their properties and accurate estimations of their real behavior. This is particularly relevant given that several alternative energy sources rely heavily on thermal radiation, perhaps even more so than the conventional ones. Thus, a more holistic approach to materials science must be followed, devoting greater care to all steps in the development of new materials to tackle the rising challenges in energy production and climate change mitigation.

Together, these points highlight the challenges lying ahead for true integration of proper emissivity characterization into the development chain of new materials with heat transfer applications. To this date, only the simplest characterization routines have found widespread use among the heat-transfer

community, as well as a certain degree of standardization. Fortunately, the recent surge in laboratories dedicated to the study of thermal radiative properties of materials signals a greater interest on this topic and points at a future with great potential.

Moreover, some interesting results from this thesis remain to be tackled. For example, the role of the Berreman effect in thin-film heat transfer and selective solar coatings, as well as a quantitative explanation of the impact of microstructural changes in the emissivity of alloys, to name a few, remain to be explored in more detail. Other pieces of work which did not end up in the thesis are also expected to be published soon and help to achieve that aim.

At this point, future lines of research must be highlighted. They can be summarized in three main points:

1. To continue upgrading the technical specifications of the HAIRL emissometer, with the aim of not only broadening its range, but to put it as close to a metrological standard of measurement as possible. Moreover, it is imperative to carry out intercomparisons with established research teams, in order to characterize systematic errors.

2. To carry on with the development and characterization of the thermal radiative properties of new materials for alternative energies. It is crucial that both studies complement each other increasingly more.

3. To advance in the theoretical description and interpretation of the thermal radiative properties of real materials, which will not only allow for a better interpretation of the results, but also aid in the design and development of new materials.

Appendices

"Constant practice devoted to one subject often outdoes both intelligence and skill."

Cicero

Appendix A

Fourier-transform infrared (FTIR) spectroscopy

Infrared spectroscopy is an essential experimental tool for analytical chemistry and condensed matter physics, among other fields. Due to the relatively long wavelengths of this spectral range, the standard spectroscopic method of filtering radiation using dispersive elements becomes inaccurate and time-consuming. Thus, other measurement approaches must be applied. The most successful of those relies on interferometrically modulated signals to measure all frequencies of interest at once, which improves both the wavelength accuracy and the signal-to-noise ratio. This Appendix includes a brief overview of these Fourier-transform infrared (FTIR) methods and the data analysis methods required.

Excellent reviews of the theoretical basis of FTIR techniques are available in classic texts, such as Griffiths and De Haseth, 1986 and Chamberlain, 1979. More introductory-level texts, such as Herres and Gronholz, 1984 and Gronholz and Herres, 1985, are also available. The fundamental concept behind this measurement procedure is the Michelson interferometer, which was exploited in the classic Michelson-Morley experiment in 1887 to detect the Earth's relative motion to the aether. A summary of the early history of interferometric spectroscopy can be found in Chamberlain, 1979, Chapter 1. In a typical Michelson interferometer, two mirrors are located in a perpendicular configuration with a 45° beamsplitter in the middle position (Figure A.1). This element theoretically reflects 50% of the radiation incident upon it and transmits the remaining 50 %. Then, both signals are reflected by their respective mirrors and then are recombined when passing through the beamsplitter again before reaching the detector. Therefore, the measured output signal intensity depends on the interference between the split signals, and thus on the

optical path difference between the interferometer arms.

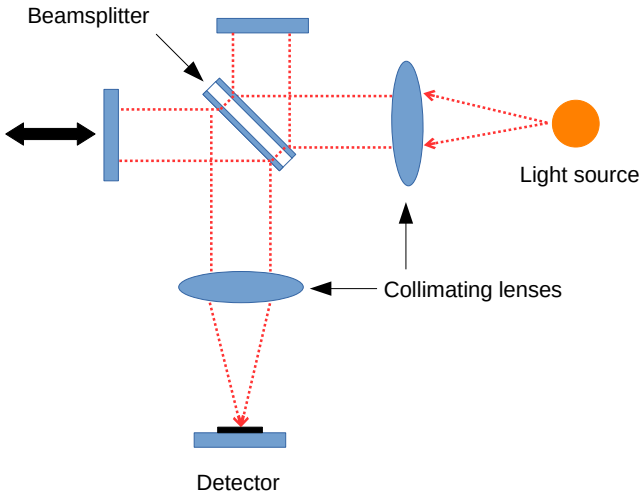

FIGURE A.1: A schematic Michelson interferometer.

The central feature of any FTIR spectrometer is a Michelson-like interferometer in which one of the mirrors oscillates periodically, thus modifying the optical path difference in a measurable manner. When shone with a polychromatic light, this mirror movement gives rise to an interferometric pattern (interferogram). If the mirror movement is accurately known (e.g., by using a He-Ne laser in parallel to provide a highly accurate and instantaneous measurement of the optical path difference), the spectral distribution of the incident light can be reconstructed by performing a real (cosine) Fourier transform of the interferogram $I(x)$:

$$S(\sigma) = \int_{-\infty}^{\infty} I(x) \cos(2\pi\sigma x) dx. \tag{A.1}$$

However, extracting useful spectroscopic information from raw interferograms is not a simple task. Firstly, Equation A.1 is always approximated by a discrete sum, which may lead to artifacts when the measured spectra features spectral lines that are not much broader than the experimental resolution. Secondly, it is not possible to probe the entire infinite range of optical path differences, but any truncated Fourier transform introduces artifical broadening of the transformed signal away from the main frequency (a phenomenon which

is dubbed leakage). Thirdly, no real-life interferometer will give rise to a completely symmetric pattern with respect to the zero-path difference (ZPD) point (as seen in Fig. A.2a), which means that it has to be phase-corrected.

Thus, the data processing performed in the Bruker IFS66v/S FTIR spectrometer equipped in the HAIRL emissometer takes places as follows. The signal received by the detector is filtered to remove high-frequency noise, and is fed to a 16-bit analog-to-digital converter. The recorded interferograms are double-sided and bi-directional, meaning that they are recorded at both sides of the ZPD in both the forward and backward directions to improve the signal-to-noise ratio.

After recording the digitized data, it is often necessary to increase the amount of datapoints in the array to a power of 2, because the fastest Fourier-transform algorithms require input data to have such a dimension for more efficient computation (Griffiths and De Haseth, 1986, Chapter 3). Therefore, zeros are added to both ends of our 3554-point interferograms until $2^{12} = 4096$ points are obtained. Then, in connection with the first data-treatment issue mentioned above, an additional zero-filling of 2 is performed (that is, the total array size is doubled by adding zeros). This increasing of the array length results in an effective interpolation of the transformed results and leads to a finer data grid without increasing the number of measured points (Herres and Gronholz, 1984). It is also more accurate than performing numerical interpolations afterwards. It must be noted that this procedure does not increase the real resolution of the data, but does allow for removing certain distortions in the shape of narrow bands.

The second main data processing stage concerns the problem of truncating the interferogram at a finite path difference D. This means that a proper Fourier transform cannot be performed. This is mathematically equivalent to performing a Fourier transform of the product of an infinite interferogram and a truncation function:

$$\int_{-D}^{D} I(x)\cos(2\pi\sigma x)dx = \int_{-\infty}^{\infty} I(x)A(x,D)\cos(2\pi\sigma x)dx, \qquad \text{(A.2)}$$

where the term $A(x, D)$ is a box function that truncates the data at path differences D and $-D$.

The problem with truncation of data is that the Fourier transform of the boxcar function $A(x, D)$ is a heavily oscillating function ($\sin(\pi\sigma)/\pi\sigma$) that leaks some of the intensity at each wavenumber to spectral regions further

apart. In order to deal with this issue, a group of solutions collective termed apodization (*removal of the foot* in Greek) have been suggested. The basis of this approach consists of selecting a smoother truncation function $A(x, D)$ that does not introduce such side-lobes when Fourier-transformed. In the case of the measurements performed in this thesis, a heavy apodization is made using the Blackman-Harris 3-term window function. This function introduces a greater broadening to the final processed signal than other options, but ensures that the least possible amount of signal is leaked far away from the desired wavenumber in the form of sine oscillations (Gronholz and Herres, 1985). As the spectral resolution chosen for this work is very low (Chapter 3), this side effect of apodization is not crucial for the accuracy of the reported results.

Finally, the phase correction procedure must be mentioned. The origin of a wavenumber-dependent interferogram phase stems from the measured ZPD point not corresponding exactly to the real one, as well as from phase delays introduced by one of more components along the optical path, such as the beamsplitter and the low-pass electronic filters (Gronholz and Herres, 1985; Griffiths and De Haseth, 1986). The main consequence of these effects is that sine components must be added to Equation A.1, which makes it a complex Fourier transform. Thus, the measured interferogram includes a wavenumber-dependent phase $\varphi(\sigma)$, which must be reconstructed:

$$I(x) = \int_{-\infty}^{\infty} S(\sigma) \cos[2\pi\sigma x - \varphi(\sigma)] d\sigma. \tag{A.3}$$

In order to compensate for this, a phase correction procedure needs to be applied. In our case, the phase correction has been performed using the standard Mertz (or multiplicative) algorithm. This procedure relies on performing both sine and cosine Fourier transforms of a shortened and weighted version of the interferogram, and then the phase is computed from the real and imaginary parts of the complex interferogram:

$$\tilde{S}(\sigma) = X(\sigma) + iY(\sigma) = S(\sigma)e^{i\varphi(\sigma)} \rightarrow \varphi(\sigma) = \arctan\left(\frac{Y(\sigma)}{X(\sigma)}\right). \tag{A.4}$$

Details of the phase correction can be found elsewhere (Griffiths and De Haseth, 1986; Gronholz and Herres, 1985).

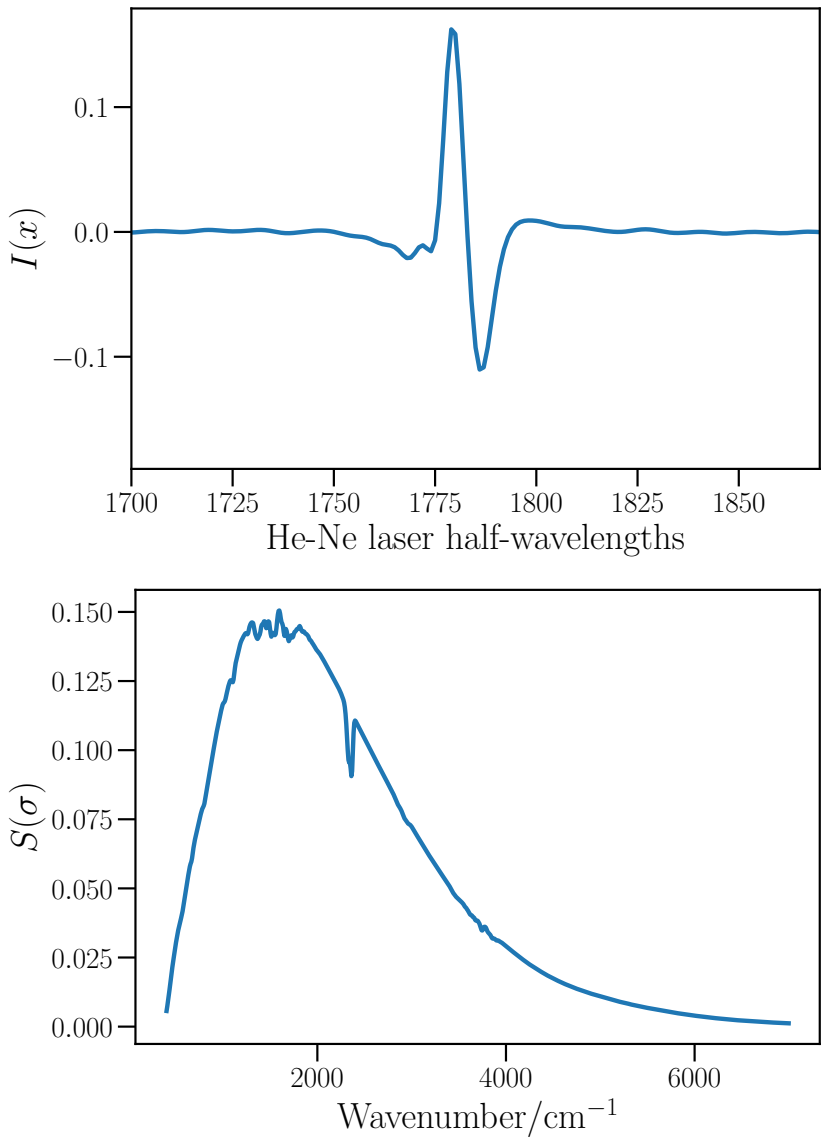

FIGURE A.2: Interferometer signal of a blackbody source in air at 1082 K and its Fourier transform after phase correction and apodization.

Appendix B

Glossary of metrological terms

Selected definitions of relevant terms adapted from the International Vocabulary of Metrology (JCGM, 2012).

Measurement uncertainty

Non-negative parameter characterizing the dispersion of the values being attributed to a quantity intended to be measured, based on the information used.

Type A evaluation of measurement uncertainty

Evaluation of a component of **measurement uncertainty** by a statistical analysis of measured quantity values obtained under defined measurement conditions.

Type B evaluation of measurement uncertainty

Evaluation of a component of **measurement uncertainty** determined by means other than a Type A evaluation of measurement uncertainty.

Standard measurement uncertainty

Measurement uncertainty expressed as a standard deviation.

Combined standard measurement uncertainty

Standard measurement uncertainty that is obtained using the individual standard measurement uncertainties associated with the input quantities in a **measurement model**.

Measurement model

Mathematical relation among all quantities known to be involved in a measurement.

Relative standard measurement uncertainty

Standard measurement uncertainty divided by the absolute value of the measured quantity value.

Uncertainty budget

Statement of a **measurement uncertainty**, of the components of that **measurement uncertainty**, and of their calculation and combination.

Expanded measurement uncertainty

Product of a combined standard measurement uncertainty and a factor larger than one (**coverage factor**).

Coverage factor

Number larger than one by which a **combined standard measurement uncertainty** is multiplied to obtain an **expanded measurement uncertainty**.

Coverage interval

Interval containing the set of true quantity values of a measured quantity with a stated probability, based on the information available.

Coverage probability

Probability that the set of true quantity values of a measured quantity is contained within a specified **coverage interval**.

Measurement error

Measured quantity value minus a reference quantity value.

Random measurement error

Component of **measurement error** that in replicate measurements varies in an unpredictable manner.

Systematic measurement error

Component of **measurement error** that in replicate measurements remains constant or varies in a predictable manner.

Measurement bias

Estimate of a **systematic measurement error**.

Correction

Compensation for an estimated systematic effect.

Limits of error

Extreme value of **measurement error**, with respect to a known reference quantity value, permitted by specifications or regulations for a given measurement, measuring instrument, or measuring system.

Measurement accuracy

Closeness of agreement between a measured quantity value and a true quantity value.

Measurement precision

Closeness of agreement between indications or measured quantity values obtained by replicate measurements on the same or similar objects under specified **conditions**.

Repeatability condition of measurement

Condition of measurement, out of a set of conditions that includes the same measurement procedure, same operators, same measuring system, same operating conditions and same location, and replicate measurements on the same or similar objects over a short period of time.

Reproducibility condition of measurement

Condition of measurement, out of a set of conditions that includes different locations, operators, measuring systems, and replicate measurements on the same or similar objects .

Measurement reproducibility

Measurement precision under **reproducibility conditions of measurement**.

Measurement standard

Realization of the definition of a given quantity, with stated quantity value and associated **measurement uncertainty**, used as a reference.

Calibration

Operation that, under specified conditions, in a first step, establishes a relation between the quantity values with measurement uncertainties provided by **measurement standards** and corresponding indications with associated **measurement uncertainties** and, in a second step, uses this information to establish a relation for obtaining a measurement result from an indication.

Metrological traceability

Property of a measurement result whereby the result can be related to a reference through a documented unbroken chain of calibrations, each contributing to the **measurement uncertainty**.

Reference material

Sufficiently homogeneous and stable material, with reference to specified properties, which has been established to be fit for its intended use in measurement.

Appendix C

The Berreman effect

A peculiar optical property of thin films, which is not predicted by the rather simple theory introduced in Chapter 2, has been observed in the materials shown in Chapter 4. This effect is named after D.W. Berreman, who first formulated it theoretically. Some of its main properties will be briefly discussed in this Appendix.[1]

The Berreman effect is a characteristic property of polar thin films when probed with obliquely incident light (Berreman, 1963). It consists of optical resonances that arise at particular frequencies in off-normal optical experiments, when the p-polarized component of the incident light couples with the LO frequency of a polar lattice mode of the film. This coupling is forbidden for infinite crystals, as electromagnetic radiation is exponentially damped inside the material for frequencies between ω_{TO} and ω_{LO}, but it is possible for films much thinner than the wavelength (Kittel, 1996).

In the case of a thin film, the Fresnel relations described in Chapter 2 (Equations 2.28 and 2.29) need to be generalized. By imposing new boundary conditions in Maxwell's equations for the thin film-substrate system, new relations can be found. To a rough first approximation, the polarized reflectances of a very thin film on a perfectly reflecting substrate can be described by rather simple expressions (Berreman, 1963):

$$\rho_s(\lambda,\theta) = |r_s|^2 \simeq 1. \tag{C.1}$$

$$\rho_p(\lambda,\theta) = |r_p|^2 \simeq 1 - \frac{8\pi d}{\lambda}\mathrm{Im}\left(-\frac{1}{\epsilon(\lambda)}\right)\frac{\sin^2\theta}{\cos\theta}, \tag{C.2}$$

[1] This Appendix will use Gaussian CGS units for simplicity of the resulting equations.

where d is the thickness of the film and $\mathrm{Im}(-1/\epsilon(\lambda))$ is the dielectric loss function of the material.

It is clear that the dielectric loss function contains all the spectral information that is relevant to the Berreman effect. This functions is shown for the particular case of LiF (same material as in Chapter 2) in Figure C.1. It has been calculated using the phonon frequencies reported in Kittel, 1996 and by setting $\gamma_{LO}/2\pi c = \gamma_{TO}/2\pi c = 10$ cm^{-1} (as in Chapter 2). It is clear from Figure C.1 that the Berreman effect must be observed at the longitudinal polar lattice mode, where $|\epsilon| \rightarrow 0$ and, thus, the dielectric loss function reaches a maximum. No strong spectral feature corresponding to the transverse mode frequency can be observed.

The key assumptions behind Equations C.1 and C.2 are that the film is placed onto a perfect reflector, and that the film is much thinner than one wavelength. Both conditions guarantee that negligible absorption takes place around the transverse mode frequency, but the longitudinal-mode absorption never vanishes. Despite their simplicity, these Equations are still useful for illustrating the semi-quantitative behavior of the observed effects. All the relevant spectral information is contained in the dielectric loss function, whose peak coincides with the LO phonon frequency in the case of a material described by Equation 2.37 (Figure C.1).

A revision of the fundamentals of the Berreman effect, along with a discussion of numerical results, can be found in Harbecke, Heinz, and Grosse, 1985. Among other results, the authors give a simple analytical expression for the critical film thickness for which the Berreman effect is maximized:

$$d_B = \frac{\lambda_{LO}}{2\pi}\frac{\cos\theta}{\sin^2\theta}\left(\mathrm{Im}\left\{-\frac{1}{\epsilon(\lambda_{LO})}\right\}\right)^{-1}. \tag{C.3}$$

Harbecke, Heinz, and Grosse, 1985 give a rough value of ~ 100 nm for the critical thickness of SiO_2 at an incident angle of 70°, but the actual value depends greatly on the peak value of the dielectric loss function under study. Nevertheless, this number is still useful to have a rough idea of the thickness required for a moderately strong effect.

Finally, the Berreman effect is illustrated using classical experimental data originally reported by Berreman, 1963 and reproduced from Kittel, 1996. Figure C.2 shows the great difference between s- and p-polarized results for reflectance experiments of silver-backed LiF at an incidence angle of 30°, relative to the bare substrate reflectivity.

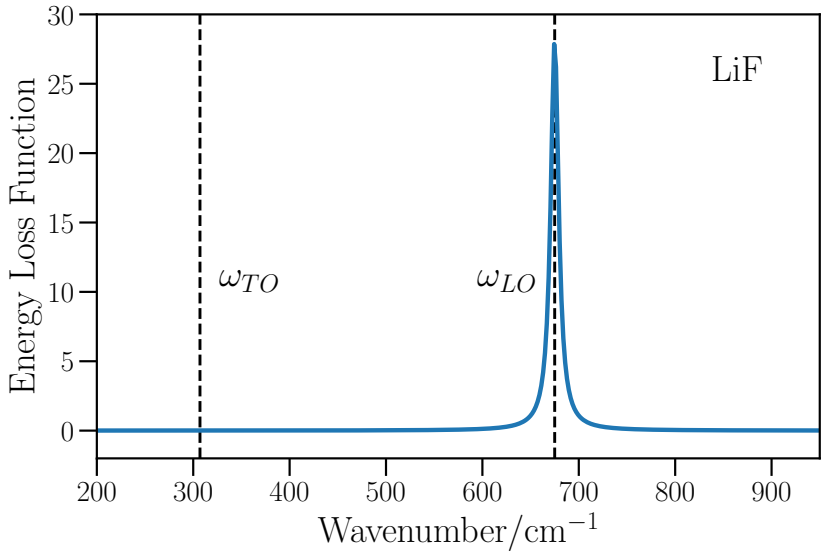

FIGURE C.1: Calculated dielectric loss function for LiF.

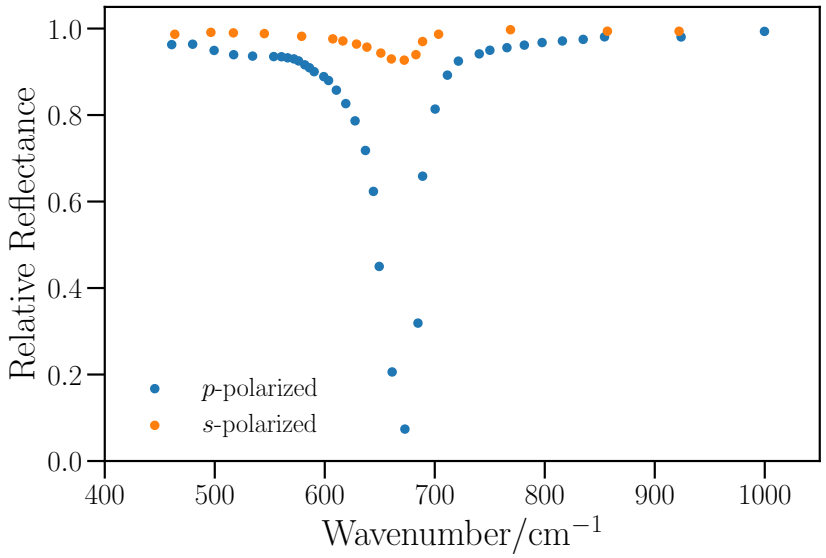

FIGURE C.2: Polarized oblique-angle (30°) reflectance of a LiF thin film on silver showing the Berreman effect.

List of publications

This thesis reproduces, in part or in full, contents from several original publications in international journals. Of those publications that involve a collaborative project, only the information regarding work performed at the University of the Basque Country (UPV/EHU), or else crucial to its interpretation, has been included in the thesis. The reader is referred to the papers for further details of these works.

This thesis reproduces contents from the following articles:

- González de Arrieta, I., T. Echániz, R. Fuente, J. M. Campillo-Robles, J. M. Igartua, G. A. López (2020). "Updated measurement method and uncertainty budget for direct emissivity measurements at UPV/EHU". *Metrologia*. Accepted manuscript.

- González de Arrieta, I., T. Echániz, R. Fuente, E. Rubin, R. Chen, J. M. Igartua, M. J. Tello, G. A. López (2019). "Infrared emissivity of copper-alloyed spinel coatings for concentrated solar power systems". *Solar Energy Materials and Solar Cells* 200, p. 109961.

- Echániz, T., I. González de Arrieta, R. Fuente, I. Urcelay-Olabarria, J. M. Igartua, N. de la Pinta, W. Ran, H. Fu, J. Chen, P. F. Zheng, M. J. Tello, G. A. López (2019). "Thermal radiative properties of electron-beam-melted and mechanically alloyed V-4Cr-4Ti based alloys between 200 and 750 °C". *Journal of Nuclear Materials* 513, pp. 86-93.

- Dan, A., B. Basu, T. Echániz, I. González de Arrieta, G. A. López, H. C. Barshilia (2018). "Effects of environmental and operational variability on the spectrally selective properties of W/WAlN/WAlON/Al_2O_3-based solar absorber coating". *Solar Energy Materials and Solar Cells* 185, pp. 342-350.

The additional publications listed below have been developed in parallel to the main research lines described in this thesis, but have been excluded in order to ensure continuity and coherence of the document:

- González de Arrieta, I., L. González-Fernández, E. Risueño, T. Echániz, M. J. Tello (2020). "Isothermal oxidation kinetics of nitrided Ti-6Al-4V studied by infrared emissivity", *Corrosion Science*. Accepted manuscript.
- González de Arrieta, I., T. Echániz, R. Fuente, G. A. López (2020). "Angle-resolved direct emissivity measurements on unencapsulated solar cells: implications for radiative cooling". In preparation.
- González de Arrieta, I. (2019). "A quartile-based interpretation of Wien's displacement law". *The Physics Teacher*. Under review.
- López, G. A., I. Alonso, J. Sáenz, A. Leonardo, S. J. González-Rojí, I. González de Arrieta, T. Echániz, I. Unzueta, J. Lafuente-Bartolome, N. de la Pinta, P. García-Goiricelaya, J. Martinez-Perdiguero, I. G. Gurtubay (2019). "Combining strategies to make General Physics lectures more attractive and to improve students' performances". *Journal of Physics: Conference Series* 1287, p. 012027.
- González de Arrieta, I., T. Echániz, J. M. Olmos, R. Fuente, I. Urcelay-Olabarria, J. M. Igartua, M. J. Tello, G. A. López (2019). "Evolution of the infrared emissivity of Ni during thermal oxidation until oxide layer opacity". *Infrared Physics & Technology* 97, pp. 270-276.
- Echániz, T., I. González de Arrieta, R. Fuente, I. Urcelay-Olabarria, E. Risueño, A. Faik, G. A. López, M. J. Tello (2018). "Sensitivity of thermal emission spectroscopy for the study of structural phase transitions". *Infrared Physics & Technology* 93, pp. 16-19.
- González de Arrieta, I., T. Echániz, R. Fuente, L. del Campo, D. De Sousa Meneses, G. A. López, M. J. Tello (2017). "Mid-infrared optical properties of pyrolytic boron nitride in the 390-1050 °C temperature range using spectral emissivity measurements". *Journal of Quantitative Spectroscopy and Radiative Transfer* 194, pp. 1-6.
- González de Arrieta, I., T. Echániz, R.B. Pérez-Sáez, M. J. Tello (2016). "Thermo-radiative and optical properties of a cutting tool based on polycrystalline cubic boron nitride (PCBN)". *Materials Research Express* 3, p. 045904.

Some results contained in this thesis have also been presented in the following conferences:

- TEMPMEKO 2019, Chengdu, China.
- THERMEC 2018, Paris, France. Invited contribution.
- Materialen Zientzia eta Teknologia IV. Kongresua 2018, San Sebastian, Basque Country, Spain.
- 20th Symposium on Thermophysical Properties 2018, Boulder, USA.
- International Conference on Materials and Energy, ICOME 2018, San Sebastian, Basque Country, Spain.
- 21st European Conference on Thermophysical Properties 2017, Graz, Austria.

Finally, science outreach and popular science efforts about topics related to the contents of this thesis include:

- González de Arrieta, I., I. González Cubiella (2019). "Dysonen esferen bila". *Elhuyar*. CAF Elhuyar 2019 science outreach prize winner.
- Echániz, T., I. González de Arrieta, R. Fuente, I. Urcelay-Olabarria, G. A. Lopez, J. M. Igartua (2018). "Eguzki-energia termikoa metatzeko materialetako emisibitate-esperimentuak". *Ekaia* 34 pp. 199-210.
- Urcelay-Olabarria, I., R. Fuente, I. González de Arrieta, T. Echániz (2018). "Dirdai berezia daukazu gaur". *Elhuyar*.

Resumen en castellano

La emisividad infrarroja es una propiedad termofísica de los materiales que relaciona la cantidad de radiación térmica que emiten con la radiada por un material ideal, un cuerpo negro. Se trata de una propiedad de gran importancia industrial, ya que su valor condiciona las transferencias de calor en situaciones de alta temperatura o alto vacío. Asimismo, su insuficiente desarrollo experimental y teórico, en comparación con otras propiedades ópticas más estudiadas, presenta desafíos científicos interesantes.

La formulación de la ley de cuerpo negro por Max Planck en 1900 dio paso a la revolución cuántica, cuyo pilar básico durante los años 10 y 20 fue el estudio de la interacción radiación-materia. Sin embargo, el desarrollo de aplicaciones tecnológicas de la radiación infrarroja tuvo que esperar décadas. Esto empezó a cambiar en los albores de la Segunda Guerra Mundial, cuando algunas de las mayores potencias militares del globo descubrieron las posibilidades que abrían los detectores infrarrojos para el combate nocturno. Posteriormente, la tecnología infrarroja se convirtió en un campo de batalla en la pugna entre la Unión Soviética y los Estados Unidos de América.

Durante gran parte del siglo XX, las aplicaciones de este rango espectral se encontraban restringidas fundamentalmente a los campos militar y aeronáutico. Organizaciones gubernamentales como la NASA poseían un monopolio efectivo sobre el conocimiento de las propiedades termorradiativas de los materiales. Posteriormente, se redujo el interés en este campo debido al descenso de financiación de estos organismos tras las misiones Apolo. No obstante, la radiación térmica ha experimentado un resurgimiento como tema de investigación en los últimos 30 años, relacionado con la fabricación de materiales de ultra alta temperatura y el mayor peso del modelado de transferencias de calor en el desarrollo de procesos industriales. A ello se suma el descubrimiento de materiales con propiedades emisivas cada vez más exóticas y con

un mayor abanico de aplicaciones. Se puede afirmar que, hoy en día, el estudio de la emisividad ha dejado de ser un terreno exclusivo del mundo militar, con una cantidad creciente de aplicaciones civiles. En particular, el desarrollo de nuevas formas de energía alternativa para combatir la inminente crisis climática requiere nuevos materiales con propiedades óptimas para la transferencia de calor por radiación.

Esta tesis doctoral se enmarca dentro de una continuidad investigadora en emisividad de materiales en los Departamentos de Física de la Materia Condensada y Física Aplicada II de la Universidad del País Vasco (UPV/EHU). Esta línea, inaugurada en 2002, continúa proveyendo de medidas de emisividad de alta exactitud y precisión a la comunidad científica internacional y al tejido industrial español. En la línea de los trabajos realizados previamente en este laboratorio por los doctores Leire del Campo, Luis González y Telmo Echániz, la presente tesis se divide en dos apartados fundamentales: por una parte, el desarrollo y mejora de métodos de medida de emisividad y, por otra, la aplicación de dichos métodos a la caracterización de materiales de interés industrial. De acuerdo con los tiempos actuales, estas aplicaciones industriales de la emisividad han virado hacia el sector energético, con el fin de desarrollar sistemas más eficientes para producir energías bajas en carbono.

Tras una introducción global y una descripción del fundamento teórico en los Capítulos 1 y 2, el Capítulo 3 reporta las bases metodológicas y experimentales de esta tesis doctoral. Tras realizar una breve revisión del estado del arte en cuanto a la medición de la emisividad infrarroja, se procede a una descripción del radiómetro HAIRL, construido en la UPV/EHU por la doctora Leire del Campo a partir de un diseño original. El método de medida y el procedimiento del aparato quedan descritos y sus especificaciones técnicas actualizadas. A continuación, se introducen un número sustancial de modificaciones al método de medida de la emisividad espectral direccional y de cuantificación de la incertidumbre experimental, que constituyen uno de los objetivos principales de la tesis. Entre ellos, se encuentra una modificación de la ecuación de medida, y una compensación de errores sistemáticos, así como un análisis mejorado de la incertidumbre para cumplir con los estándares internacionales. Además, se plantea un novedoso método de cálculo de emisividades totales mediante la integración numérica de los datos espectrales y la propagación de sus incertidumbres por un método de Monte Carlo. Por último, se presentan resultados para materiales metálicos y cerámicos con el fin de validar dicha metodología. Se espera que estos avances sean de utilidad a la comunidad, debido a la similitud entre los métodos de medida.

A continuación, en el Capítulo 4 se introducen los materiales para energía solar térmica empleados en esta tesis y la caracterización de sus propiedades termorradiativas. La energía solar térmica es una fuente alternativa de energía que aprovecha directamente el calor radiado por el sol para calentar fluidos. En su versión de mayor escala, denominada energía termosolar de concentración (CSP, por sus siglas en inglés), posee la capacidad de proveer energía de base a una red eléctrica, puesto que el almacenamiento de calor (y su posterior conversión en una turbina) es mucho más sencillo que el almacenamiento directo de electricidad. Existen dos tipos fundamentales de tecnologías CSP, aquellas que emplean espejos parabólicos para calentar tubos y las que emplean campos de espejos focalizando la radiación solar en lo alto de una torre. Cada uno de estos métodos presenta unos requisitos diferentes: mientras los sistemas parabólicos de tubo trabajan a menor temperatura en vacío, los sistemas de torre operan en aire a temperaturas mucho más altas.

Los sistemas de energía termosolar concentrada de tubo consisten en espejos parabólicos que concentran la energía del sol en su línea focal, donde se encuentra un tubo por el que circula un fluido que extrae el calor absorbido. Con el fin de maximizar la energía retenida, se recubren dichos tubos con materiales que absorban la mayor cantidad de radiación solar posible y reemitan la mínima. A estos materiales se los denomina recubrimientos selectivos, puesto que presentan propiedades ópticas y termorradiativas diferentes para las longitudes de onda de la luz solar y para el infrarrojo. Dado que estos tubos se emplean con un sistema de vacío, es posible explorar materiales multicapa con propiedades exóticas que no serían estables en aire. En esta tesis hemos estudiado unos recubrimientos de base wolframio ($W/WAlN/WAlON/Al_2O_3$) con unas propiedades prometedoras. Se ha determinado su emisividad en función de la temperatura, longitud de onda y ángulo. Se observa que su emisividad espectral depende sólo ligeramente de la temperatura en el rango hasta 500 °C, tanto en vacío como en aire. No obstante, debido a la fuerte dependencia de la emisividad con la longitud de onda, sí se aprecia un aumento notable de la emisión total a las temperaturas más altas. Por último, se observa un aumento sustancial de la emisividad espectral en función del ángulo, incluyendo un modo resonante que ha sido asociado al efecto Berreman en la capa superior de alúmina. Esto revela la importancia de una correcta caracterización de la emisividad de estos recubrimientos a la hora de estimar sus pérdidas reales de calor por radiación y su eficiencia en condiciones reales de trabajo.

Por otra parte, las torres solares funcionan al aire a mucha mayor temperatura, por lo que no es posible emplear materiales complejos para optimizar la eficiencia de captación de energía solar. Por ello, la estrategia habitual consiste en emplear pinturas negras de alta absorbancia solar y resistentes a las altas temperaturas, aunque sus pérdidas por radiación sean significativas. El estándar actual de esta tecnología es la pintura Pyromark 2500, que posee unas buenas propiedades pero no es estable a las temperaturas extremas a las que se pretende hacer trabajar estos sistemas en el futuro. Por ello, se investigan actualmente alternativas más estables y que, a poder ser, presenten además mejoras en la captación y retención de la energía térmica. Entre ellas, las espinelas son unos materiales con propiedades prometedoras, debido a su gran estabilidad estructural a alta temperatura. En este trabajo se han estudiado varios tipos de espinelas ($Cu_{0.5}Cr_{1.1}Mn_{1.4}O_4$, $CuFeMnO_4$ y $CuCr_2O_4$) y se han comparado sus propiedades termorradiativas con las de una muestra de Pyromark 2500 depositada en las mismas condiciones. Se observa una importante correlación entre la porosidad de estos materiales y su eficiencia, puesto que la creación de poros aumenta la capacidad del material de atrapar la radiación incidente y también reduce su capacidad de emisión mediante un cierto grado de selectividad direccional. Esta correlación positiva indica la posibilidad de optimizar materiales por esta vía, dada la dificultad de desarrollar materiales selectivos en longitud de onda a temperaturas tan altas. En general, se demuestra la importancia de la estructura del material a la hora de determinar sus propiedades termorradiativas. A pesar de que se todos estos materiales son más estables que la pintura Pyromark, no todos presentan eficiencias de conversión solar tan altas. No obstante, en el caso del recubrimiento más poroso, sí se consigue un incremento de la eficiencia de 0.93, comparado con un valor de 0.92 (Pyromark) a temperaturas en las cuales dicha pintura no sería estable a largo plazo.

Por último, el Capítulo 5 introduce la última familia de muestras estudiada en esta tesis. Se trata de aleaciones de base vanadio con potencial para ser empleadas como materiales estructurales en reactores de fusión experimentales como DEMO, el sucesor del famoso ITER. Las exigentes condiciones que debe cumplir un material aplicado en tal reactor implican que sólo compuestos formados por unos pocos elementos pueden ser empleados. Dadas dichas limitaciones, las aleaciones V-Cr-Ti se revelan como unas de las pocas familias de materiales compatibles. Sin embargo, su síntesis y procesado es muy complejo, por lo que existe una amplia variabilidad de microestructuras entre muestras, en función de su historia térmica y método de

fabricación. Puesto que el principal modo de transferencia de calor en estos reactores es la radiación térmica, la ausencia de datos fiables sobre la emisividad de estas aleaciones supone un problema a la hora de realizar simulaciones precisas sobre el comportamiento del reactor. Asimismo, es crucial averiguar qué influencia tiene dicha variabilidad microestructural en las propiedades termorradiativas de estos materiales. Hemos determinado que, si bien el comportamiento general obedece las predicciones de la teoría de los metales, existen diferencias estadísticamente significativas entre las emisividades de las cuatro muestras estudiadas. En particular, hemos encontrado que la mayor y más estable emisividad corresponde a una muestra de composición mejorada (Y_2O_3, Ti_3SiC_2) aleada mecánicamente, que es asimismo la muestra con mejores propiedades mecánicas. La razón de las diferencias en las propiedades radiativas de las distintas muestras se haya en la complejidad microscópica de estos materiales (fases secundarias, elementos intersticiales) y su evolución con la temperatura. Es posible analizar estas diferencias de modo semicuantitativo mediante el modelo de Drude, que arroja luz sobre el tipo de evolución microestructural que experimenta cada tipo de muestra, lo cual se puede correlacionar con medidas experimentales de difraccion de rayos X y microscopía, entre otras. Por último, es importante observar que en todas las muestras estudiadas las emisividades integradas se encuentran por debajo de los valores entre 0.25 y 0.35 comúnmente asumidos en las simulaciones de transferencias de calor en reactores de fusión nuclear.

En resumen, esta tesis doctoral reporta importantes avances originales en la mejora de los métodos de medición de la emisividad infrarroja, así como resultados de mediciones de dicha propiedad en materiales de alto interés para el sector de las energías alternativas. Se demuestra la complejidad del estudio de las propiedades termorradiativas, así como la necesidad de emprender estudios más rigurosos para obtener estimaciones más exactas y precisas del comportamiento de los materiales en aplicaciones de transferencia de calor.

Bibliography

Adibekyan, A., E. Kononogova, C. Monte, and J. Hollandt (2017). "High-accuracy emissivity data on the coatings Nextel 811-21, Herberts 1534, Aeroglaze Z306 and Acktar Fractal Black". *International Journal of Thermophysics* 38, p. 89. DOI: 10.1007/s10765-017-2212-z.

Adibekyan, A., C. Monte, M. Kehrt, B. Gutschwager, and J. Hollandt (2015). "Emissivity measurement under vacuum from 4 μm to 100 μm and from -40 °C to 450 °C at PTB". *International Journal of Thermophysics* 36, pp. 283–289. DOI: 10.1007/s10765-014-1745-7.

ASTM (2012). *Standard Tables for Reference Solar Spectral Irradiances: Direct Normal and Hemispherical on 37° Tilted Surface*. Standard. West Conshohocken: ASTM International. DOI: 10.1520/G0173-03R12.

Autio, G. W. and E. Scala (1966). "The normal spectral emissivity of isotropic and anisotropic materials". *Carbon* 4, pp. 13–28. DOI: 10.1016/0008-6223(66)90005-4.

Badescu, V. (2005). "Spectrally and angularly selective photothermal and photovoltaic converters under one-sun illumination". *Journal of Physics D: Applied Physics* 38, p. 2166. DOI: 10.1088/0022-3727/38/13/014.

Balat-Pichelin, M., J. L. Sans, E. Bêche, V. Flaud, and J. Annaloro (2017). "Oxidation and emissivity of Inconel 718 alloy as potential space debris during its atmospheric entry". *Materials Characterization* 127, pp. 379–390. DOI: 10.1016/j.matchar.2017.02.016.

Barshilia, H. C. (2014). "Growth, characterization and performance evaluation of Ti/AlTiN/AlTiON/AlTiO high temperature spectrally selective coatings for solar thermal power applications". *Solar Energy Materials and Solar Cells* 130, pp. 322–330. DOI: 10.1016/j.solmat.2014.07.037.

Bartelmeß, L., C. Monte, A. Adibekyan, O. Sohr, C. Ottermann, T. Korb, and J. Hollandt (2014). "Characterization of high temperature solar thermal selective absorber coatings at operation temperature". *Energy Procedia* 49, pp. 2070–2079. DOI: 10.1016/j.egypro.2014.03.219.

Berreman, D. W. (1963). "Infrared absorption at longitudinal optic frequency in cubic crystal films". *Physical Review* 130, pp. 2193–2198. DOI: 10.1103/PhysRev.130.2193.

Berreman, D. W. and F. Unterwald (1968). "Adjusting poles and zeros of dielectric dispersion to fit Reststrahlen of $PrCl_3$ and $LaCl_3$". *Physical Review* 174, pp. 791–799. DOI: 10.1103/PhysRev.174.791.

Bigot, B. (2017). "ITER: A unique international collaboration to harness the power of the stars". *Comptes Rendus Physique* 18, pp. 367–371. DOI: 10.1016/j.crhy.2017.09.002.

Bilokur, M., A. R. Gentle, M. D. Arnold, M. B. Cortie, and G. B. Smith (2019). "High temperature optically stable spectrally-selective $Ti_{1-x}Al_xN$-based multilayer coating for concentrated solar thermal applications". *Solar Energy Materials and Solar Cells* 200, p. 109964. DOI: 10.1016/j.solmat.2019.109964.

Blanco, M. J., J. G. Martín, and D. C. Alarcón-Padilla (2004). "Theoretical efficiencies of angular-selective non-concentrating solar thermal systems". *Solar Energy* 76, pp. 683–691. DOI: 10.1016/j.solener.2004.01.005.

Bloom, E. E. (1998). "The challenge of developing structural materials for fusion power systems". *Journal of Nuclear Materials* 258, pp. 7–17. DOI: 10.1016/S0022-3115(98)00352-3.

Boubault, A., B. Claudet, O. Faugeroux, N. Guerin, and G. Olalde (2013). "Study of the aging of a solar absorber material following the evolution of its thermoradiative and thermophysical properties". *High Temperatures–High Pressures* 42, pp. 405–420.

Boubault, A., C. K. Ho, A. Hall, T. N. Lambert, and A. Ambrosini (2016). "Levelized cost of energy (LCOE) metric to characterize solar absorber coatings for the CSP industry". *Renewable Energy* 85, pp. 472–483. DOI: 10.1016/j.renene.2015.06.059.

Boubault, A., C. K. Ho, A. Hall, T. N. Lambert, and A. Ambrosini (2017). "Durability of solar absorber coatings and their cost-effectiveness". *Solar Energy Materials and Solar Cells* 166, pp. 176–184. DOI: 10.1016/j.solmat.2017.03.010.

Cao, G., S. J. Weber, S. O. Martin, M. H. Anderson, K. Sridharan, and T. R. Allen (2012). "Spectral emissivity measurements of candidate materials for very high temperature reactors". *Nuclear Engineering and Design* 251, pp. 78–83. DOI: 10.1016/j.nucengdes.2011.10.067.

Cárdenas-García, D. (2014). "Emissivity measurement of high-emissivity black paint at CENAM". *Revista Mexicana de Fisica* 60, pp. 305–308.

Cárdenas-García, D. and C. Monte (2014). "Bilateral intercomparison of spectral directional emissivity measurement between CENAM and PTB". *International Journal of Thermophysics* 35, pp. 1299–1309. DOI: 10.1007/s10765-014-1686-1.

Chamberlain, J. (1979). *The principles of interferometric spectroscopy*. Chichester: Wiley.

Chen, J. M., V. M. Chernov, R. J. Kurtz, and T. Muroga (2011). "Overview of the vanadium alloy researches for fusion reactors". *Journal of Nuclear Materials* 417, pp. 289–294. DOI: 10.1016/j.jnucmat.2011.02.015.

Cheng, S. X., P. Cebe, L. M. Hanssen, D. M. Riffe, and A. J. Sievers (1987). "Hemispherical emissivity of V, Nb, Ta, Mo, and W from 300 to 1000 K". *Journal of the Optical Society of America B* 4, pp. 351–356. DOI: 10.1364/JOSAB.4.000351.

Chu, S. and A. Majumdar (2012). "Opportunities and challenges for a sustainable energy future". *Nature* 488, pp. 294–303. DOI: 10.1038/nature11475.

Cohen, E. R. and P. Giacomo (1987). *Symbols, units, nomenclature and fundamental constants in physics*. Tech. rep. IUPAP-25 (SUNAMCO 87-1). International Union of Pure and Applied Physics.

Cordero, R. R., G. Seckmeyer, D. Pissulla, and F. Labbe (2007). "Uncertainty of experimental integrals: application to the UV index calculation". *Metrologia* 45, pp. 1–10. DOI: 10.1088/0026-1394/45/1/001.

Costantini, D., A. Lefebvre, A. L. Coutrot, I. Moldovan-Doyen, J. P. Hugonin, S. Boutami, F. Marquier, H. Benisty, and J. J. Greffet (2015). "Plasmonic metasurface for directional and frequency-selective thermal emission". *Physical Review Applied* 4, p. 014023. DOI: 10.1103/PhysRevApplied.4.014023.

Coventry, J. and P. Burge (2017). "Optical properties of Pyromark 2500 coatings of variable thicknesses on a range of materials for concentrating solar thermal applications". *AIP Conference Proceedings* 1850, p. 030012. DOI: 10.1063/1.4984355.

Dan, A., B. Basu, T. Echániz, I. González de Arrieta, G. A. López, and H. C. Barshilia (2018a). "Effects of environmental and operational variability on the spectrally selective properties of W/WAlN/WAlON/Al_2O_3-based solar absorber coating". *Solar Energy Materials and Solar Cells* 185, pp. 342 – 350. DOI: 10.1016/j.solmat.2018.04.020.

Dan, A., H. C. Barshilia, K. Chattopadhyay, and B. Basu (2017). "Solar energy absorption mediated by surface plasma polaritons in spectrally selective

dielectric-metal-dielectric coatings: a critical review". *Renewable and Sustainable Energy Reviews* 79, pp. 1050–1077. DOI: 10.1016/j.rser.2017.05.062.

Dan, A., A. Biswas, P. Sarkar, S. Kashyap, K. Chattopadhyay, H. C. Barshilia, and B. Basu (2018b). "Enhancing spectrally selective response of W/WAlN /WAlON/Al_2O_3-based nanostructured multilayer absorber coating through graded optical constants". *Solar Energy Materials and Solar Cells* 176, pp. 157–166. DOI: 10.1016/j.solmat.2017.11.013.

Dan, A., J. Jyothi, K. Chattopadhyay, H. C. Barshilia, and B. Basu (2016). "Spectrally selective absorber coating of WAlN/WAlON/Al_2O_3 for solar thermal applications". *Solar Energy Materials and Solar Cells* 157, pp. 716–726. DOI: 10.1016/j.solmat.2016.07.018.

Dan, A., A. Soum-Glaude, A. Carling-Plaza, C. K. Ho, K. Chattopadhyay, H. C. Barshilia, and B. Basu (2019). "Temperature- and angle-dependent emissivity and thermal shock resistance of the W/WAlN/WAlON/Al_2O_3-based spectrally selective absorber". *ACS Applied Energy Materials* 2, pp. 5557–5567. DOI: 10.1021/acsaem.9b00743.

De, K. S., J. Ghose, and K. S. R. C. Murthy (1982). "Electrical properties of the $CuCr_2O_4$ spinel catalyst". *Journal of Solid State Chemistry* 43, pp. 261–266. DOI: 10.1016/0022-4596(82)90238-9.

De Sousa Meneses, D., G. Gruener, M. Malki, and P. Echegut (2005). "Causal Voigt profile for modeling reflectivity spectra of glasses". *Journal of Non-Crystalline Solids* 351, pp. 124–129. DOI: 10.1016/j.jnoncrysol.2004.09.028.

De Sousa Meneses, D., P. Melin, L. del Campo, L. Cosson, and P. Echegut (2015). "Apparatus for measuring the emittance of materials from far infrared to visible wavelengths in extreme conditions of temperature". *Infrared Physics & Technology* 69, pp. 96 –101. DOI: 10.1016/j.infrared.2015.01.011.

De Sousa Meneses, D. (2020). *FOCUS - Curve fitting software 2.0*. https://www.cemhti.cnrs-orleans.fr/pot/software/focus.html.

del Campo, L., R. B. Pérez-Sáez, M. J. Tello, X. Esquisabel, and I. Fernández (2006a). "Armco iron normal spectral emissivity measurements". *International Journal of Thermophysics* 27, pp. 1160–1172. DOI: 10.1007/s10765-006-0081-y.

del Campo, L., R. B. Pérez-Sáez, X. Esquisabel, I. Fernández, and M. J. Tello (2006b). "New experimental device for infrared spectral directional emissivity measurements in a controlled environment". *Review of Scientific Instruments* 77, p. 113111. DOI: 10.1063/1.2393157.

del Campo, L., R. B. Pérez-Sáez, L. González-Fernández, and M. J. Tello (2010). "Combined standard uncertainty in direct emissivity measurements". *Journal of Applied Physics* 107, p. 113510. DOI: 10.1063/1.3431541.

Dressel, M. and G. Grüner (2002). *Electrodynamics of solids: optical properties of electrons in matter*. Cambridge: Cambridge University Press.

Du, M., X. Liu, L. Hao, X. Wang, J. Mi, L. Jiang, and Q. Yu (2013). "Microstructure and thermal stability of $Al/Ti_{0.5}Al_{0.5}N/Ti_{0.25}Al_{0.75}N/AlN$ solar selective coating". *Solar Energy Materials and Solar Cells* 111, pp. 49–56. DOI: 10.1016/j.solmat.2012.12.010.

Dufour, P. C., N. L. Rowell, and A. G. Steele (1998). "Fourier-transform radiation thermometry: measurements and uncertainties". *Applied Optics* 37, pp. 5923–5931. DOI: 10.1364/AO.37.005923.

Echániz, T., I. González de Arrieta, R. Fuente, I. Urcelay-Olabarria, J. M. Igartua, N. de la Pinta, W. Ran, H. Fu, J. Chen, P. F. Zheng, M. J. Tello, and G. A. López (2019). "Thermal radiative properties of electron-beam-melted and mechanically alloyed V-4Cr-4Ti based alloys between 200 and 750 °C". *Journal of Nuclear Materials* 513, pp. 86–93. DOI: 10.1016/j.jnucmat.2018.10.051.

Echániz, T., R. B. Pérez-Sáez, and M. J. Tello (2017). "IR radiometer sensitivity and accuracy improvement by eliminating spurious radiation for emissivity measurements on highly specular samples in the 2–25 μm spectral range". *Measurement* 110, pp. 22–26. DOI: 10.1016/j.measurement.2017.06.010.

Echániz, T., I. Setién-Fernández, R. B. Pérez-Sáez, C. Prieto, R. Escobar Galindo, and M. J. Tello (2015). "Importance of the spectral emissivity measurements at working temperature to determine the efficiency of a solar selective coating". *Solar Energy Materials and Solar Cells* 140, pp. 249–252. DOI: 10.1016/j.solmat.2015.04.009.

Esward, T. J., A. de Ginestous, P. M. Harris, I. D. Hill, S. G. R. Salim, I. M. Smith, B. A. Wichmann, R. Winkler, and E. R. Woolliams (2007). "A Monte Carlo method for uncertainty evaluation implemented on a distributed computing system". *Metrologia* 44, pp. 319–326. DOI: 10.1088/0026-1394/44/5/008.

Fang, J., N. Tu, J. Wei, and X. Du (2018). "Effects of surface optical and radiative properties on the thermal performance of a solar cavity receiver". *Solar Energy* 171, pp. 157–170. DOI: 10.1016/j.solener.2018.06.075.

Filtz, J. R. and J. Hameury (2000). *Intercomparison of total hemispherical and normal spectral emissivity measurements*. Tech. rep. EUROMET Project 516. European Collaboration in Measurement Standards. URL: https://www.euramet.org/Media/docs/projects/516_THERM_Final.pdf.

Filtz, J. R., J. Wu, C. Stacey, J. Hollandt, C. Monte, B. Hay, J. Hameury, M. A. Villamañan, E. Thurzo-Andras, and S. Sarge (2015). "A European roadmap for thermophysical properties metrology". *International Journal of Thermophysics* 36, pp. 516–528. DOI: 10.1007/s10765-014-1807-x.

Florescu, M., H. Lee, I. Puscasu, M. Pralle, L. Florescu, D. Z. Ting, and J. P. Dowling (2007). "Improving solar cell efficiency using photonic band-gap materials". *Solar Energy Materials and Solar Cells* 91, pp. 1599–1610. DOI: 10.1016/j.solmat.2007.05.001.

Fu, H. Y., J. M. Chen, P. F. Zheng, T. Nagasaka, T. Muroga, Z. D. Li, S. Cui, and Z. Y. Xu (2013). "Fabrication using electron beam melting of a V–4Cr–4Ti alloy and its thermo-mechanical strengthening study". *Journal of Nuclear Materials* 442, S336–S340. DOI: 10.1016/j.jnucmat.2013.01.337.

Gervais, F. (2002). "Optical conductivity of oxides". *Materials Science and Engineering: R: Reports* 39, pp. 29–92. DOI: 10.1016/S0927-796X(02)00073-6.

González de Arrieta, I., T. Echániz, R. Fuente, J. M. Campillo-Robles, J. M. Igartua, and G. A. López (2020). "Updated measurement method and uncertainty budget for direct emissivity measurements at UPV/EHU". *Metrologia*. Accepted manuscript. DOI: 10.1088/1681-7575/ab84ff. eprint: arXiv:1910.08315.

González de Arrieta, I., T. Echániz, R. Fuente, E. Rubin, R. Chen, J. M. Igartua, M. J. Tello, and G. A. López (2019). "Infrared emissivity of copper-alloyed spinel black coatings for concentrated solar power systems". *Solar Energy Materials and Solar Cells* 200, p. 109961. DOI: 10.1016/j.solmat.2019.109961.

González de Arrieta, I., T. Echániz, J. M. Olmos, R. Fuente, I. Urcelay-Olabarria, J. M. Igartua, M. J. Tello, and G. A. López (2019). "Evolution of the infrared emissivity of Ni during thermal oxidation until oxide layer opacity". *Infrared Physics & Technology* 97, pp. 270 –276. DOI: 10.1016/j.infrared.2019.01.002.

González de Arrieta, I., T. Echániz, R. B. Pérez-Sáez, and M. J. Tello (2016). "Thermo-radiative and optical properties of a cutting tool based on polycrystalline cubic boron nitride (PCBN)". *Materials Research Express* 3, p. 045904. DOI: 10.1088/2053-1591/3/4/045904.

González-Fernández, L., R. B. Pérez-Sáez, L. del Campo, and M. J. Tello (2010). "Analysis of calibration methods for direct emissivity measurements". *Applied Optics* 49, pp. 2728–2735. DOI: 10.1364/AO.49.002728.

Griffiths, P. R. and J. A. De Haseth (1986). "Fourier transform infrared spectrometry." *Chemical Analysis: A series of monographs on analytical chemistry and its applications*. Ed. by P. J. Elving and J. D. Winefordner. Vol. 83. New York: John Wiley & Sons.

Gronholz, J. and W. Herres (1985). "Understanding FT-IR data processing. Part 2: Details of the spectrum calculation". *Intelligent Instruments and Computers, Applications in the Laboratory* 3, pp. 10–19.

Hamam, R. E., I. Celanovic, and M. Soljačić (2011). "Angular photonic band gap". *Physical Review A* 83, p. 035806. DOI: 10.1103/PhysRevA.83.035806.

Hameury, J., S. Clausen, F. Manoocheri, R. Kersting, J. Manara, T. Meisel, C. Monte, E. Palacio, G. P. Adorno, and H. Simon (2018). "Improvement of emissivity measurements on reflective insulation materials". *20th Symposium on Thermophysical Properties*. Boulder, CO. URL: https://thermosymposium.nist.gov/pdf/Abstract_3562.pdf.

Hanssen, L. M., B. Wilthan, J. R. Filtz, J. Hameury, F. Girard, M. Battuello, J. Ishii, J. Hollandt, and C. Monte (2016). "Infrared spectral normal emittance/emissivity comparison". *Metrologia* 53, p. 03001. DOI: 10.1088/0026-1394/53/1A/03001.

Hanssen, L. M., C. P. Cagran, A. V. Prokhorov, S. N. Mekhontsev, and V. B. Khromchenko (2007). "Use of a high-temperature integrating sphere reflectometer for surface-temperature measurements". *International Journal of Thermophysics* 28, pp. 566–580. DOI: 10.1007/s10765-007-0180-4.

Harbecke, B., B. Heinz, and P. Grosse (1985). "Optical properties of thin films and the Berreman effect". *Applied Physics A* 38, pp. 263–267. DOI: 10.1007/BF00616061.

Hatano, Y., R. Hayakawa, K. Nishino, S. Ikeno, T. Nagasaka, T. Muroga, and K. Watanabe (2005). "Surface segregation of Ti in a V-4Cr-4Ti alloy and its influence on the surface reaction rates of hydrogen isotopes". *Materials Transactions* 46, pp. 511–516. DOI: 10.2320/matertrans.46.511.

Hernandez, D., J. M. Badie, F. Escourbiac, and R. Reichle (2008). "Development of two-colour pyroreflectometry technique for temperature monitoring of tungsten plasma facing components". *Fusion Engineering and Design* 83, pp. 672–679. DOI: 10.1016/j.fusengdes.2008.02.008.

Herres, W. and J. Gronholz (1984). "Understanding FT-IR data processing. Part 1: Data acquisition and Fourier transformation". *Computer Applications in the Laboratory* 2, pp. 216–220.

Ho, C. K., A. R. Mahoney, A. Ambrosini, M. Bencomo, A. Hall, and T. N. Lambert (2014). "Characterization of Pyromark 2500 paint for high-temperature solar receivers". *Journal of Solar Energy Engineering* 136, p. 014502. DOI: 10.1115/1.4024031.

Ho, C. K. and J. E. Pacheco (2014). "Levelized Cost of Coating (LCOC) for selective absorber materials". *Solar Energy* 108, pp. 315–321. DOI: 10.1016/j.solener.2014.05.017.

Honner, M. and P. Honnerová (2015). "Survey of emissivity measurement by radiometric methods". *Applied Optics* 54, pp. 669–683. DOI: 10.1364/AO.54.000669.

Honnerová, P., J. Martan, and M. Honner (2017). "Uncertainty determination in high-temperature spectral emissivity measurement method of coatings". *Applied Thermal Engineering* 124, pp. 261–270. DOI: 10.1016/j.applthermaleng.2017.06.022.

Honnerová, P., J. Martan, M. Kučera, M. Honner, and J. Hameury (2014). "New experimental device for high-temperature normal spectral emissivity measurements of coatings". *Measurement Science and Technology* 25, p. 095501. DOI: 10.1088/0957-0233/25/9/095501.

Höser, D., R. Wallimann, and P. R. von Rohr (2016). "Uncertainty analysis for emissivity measurement at elevated temperatures with an infrared camera". *International Journal of Thermophysics* 37, p. 14. DOI: 10.1007/s10765-015-2022-0.

Howell, J. R., M. P. Mengüç, and R. Siegel (2010). *Thermal Radiation Heat Transfer*. 5th ed. Boca Raton: CRC Press.

Hunnewell, T. S., K. L. Walton, S. Sharma, T. K. Ghosh, R. V. Tompson, D. S. Viswanath, and S. K. Loyalka (2017). "Total hemispherical emissivity of SS 316L with simulated very high temperature reactor surface conditions". *Nuclear Technology* 198, pp. 293–305. DOI: 10.1080/00295450.2017.1311120.

Ishii, J. and A. Ono (2001). "Uncertainty estimation for emissivity measurements near room temperature with a Fourier transform spectrometer".

Measurement Science and Technology 12, p. 2103. DOI: 10.1088/0957-0233/12/12/311.

JCGM (2008a). *Evaluation of measurement data - Guide to the expression of uncertainty in measurement*. Tech. rep. JCGM 100:2008. Joint Committee for Guides in Metrology.

JCGM (2008b). *Evaluation of measurement data - Supplement 1 to the "Guide to the expression of uncertainty in measurement" - Propagation of distributions using a Monte Carlo method*. Tech. rep. JCGM 101:2008. Joint Committee for Guides in Metrology.

JCGM (2012). *The international vocabulary of metrology - Basic and general concepts and associated terms (VIM)*. Tech. rep. JCGM 200:2012. Joint Committee for Guides in Metrology.

Jeon, S., S. N. Park, Y. S. Yoo, J. Hwang, C. W. Park, and G. W. Lee (2010). "Simultaneous measurement of emittance, transmittance, and reflectance of semitransparent materials at elevated temperature". *Optics Letters* 35, pp. 4015–4017. DOI: 10.1364/OL.35.004015.

JIS (2001). *Geometrical Product Specifications (GPS)-Surface texture:Profile method-Terms, definitions and surface texture parameters*. Standard. Tokyo: Japanese Industrial Standards.

Johnson, P. B. and R. W. Christy (1974). "Optical constants of transition metals: Ti, V, Cr, Mn, Fe, Co, Ni, and Pd". *Physical Review B* 9, pp. 5056–5070. DOI: 10.1103/PhysRevB.9.5056.

Jyothi, J., A. Soum-Glaude, H. S. Nagaraja, and H. C. Barshilia (2017). "Measurement of high temperature emissivity and photothermal conversion efficiency of TiAlC/TiAlCN/TiAlSiCN/TiAlSiCO/TiAlSiO spectrally selective coating". *Solar Energy Materials and Solar Cells* 171, pp. 123–130. DOI: 10.1016/j.solmat.2017.06.057.

Kaltchev, M. and W. T. Tysoe (1999). "An infrared spectroscopic investigation of thin alumina films: measurement of acid sites and surface reactivity". *Surface Science* 430, pp. 29–36. DOI: 10.1016/S0039-6028(99)00376-3.

Karas, D. E., J. Byun, J. Moon, and C. Jose (2018). "Copper-oxide spinel absorber coatings for high-temperature concentrated solar power systems". *Solar Energy Materials and Solar Cells* 182, pp. 321–330. DOI: 10.1016/j.solmat.2018.03.025.

Keller, B. P., S. E. Nelson, K. L. Walton, T. K. Ghosh, R. V. Tompson, and S. K. Loyalka (2015). "Total hemispherical emissivity of Inconel 718". *Nuclear*

Engineering and Design 287, pp. 11–18. DOI: 10.1016/j.nucengdes.2015.02.018.

Keltner, N. R. and J. V. Beck (1983). "Surface temperature measurement errors". *Journal of Heat Transfer* 105, pp. 312–318. DOI: 10.1115/1.3245580.

Kennedy, C. E. (2002). *Review of mid-to high-temperature solar selective absorber materials*. Tech. rep. NREL/TP-520-31267. National Renewable Energy Lab. URL: https://www.nrel.gov/docs/fy02osti/31267.pdf.

Kim, T. K., B. VanSaders, E. Caldwell, S. Shin, Z. Liu, S. Jin, and R. Chen (2016). "Copper-alloyed spinel black oxides and tandem-structured solar absorbing layers for high-temperature concentrating solar power systems". *Solar Energy* 132, pp. 257–266. DOI: 10.1016/j.solener.2016.03.007.

King, J. L., H. Jo, R. Tirawat, K. Blomstrand, and K. Sridharan (2017). "Effects of surface roughness, oxidation, and temperature on the emissivity of reactor pressure vessel alloys". *Nuclear Technology* 200, pp. 1–14. DOI: 10.1080/00295450.2017.1353869.

King, J. L., H. Jo, A. Shahsafi, K. Blomstrand, K. Sridharan, and M. A. Kats (2018). "Impact of corrosion on the emissivity of advanced reactor structural alloys". *Journal of Nuclear Materials* 508, pp. 465–471. DOI: 10.1016/j.jnucmat.2018.05.047.

Kitamura, R., L. Pilon, and M. Jonasz (2007). "Optical constants of silica glass from extreme ultraviolet to far infrared at near room temperature". *Applied Optics* 46, pp. 8118–8133. DOI: 10.1364/AO.46.008118.

Kittel, C. (1996). *Introduction to Solid State Physics*. 7th ed. New York: John Wiley & Sons.

Končar, B., M. Draksler, O. C. Garrido, and B. Meszaros (2017). "Thermal radiation analysis of DEMO tokamak". *Fusion Engineering and Design* 124, pp. 567–571. DOI: 10.1016/j.fusengdes.2017.03.134.

Le Baron, E., O. Raccurt, P. Giraud, M. Adier, J. Barriga, B. Diaz, P. Echegut, D. De Sousa Meneses, C. Capiani, D. Sciti, A. Soum-Glaude, C. Escape, I. Jerman, G. A. López, T. Echániz, M. J. Tello, F. Matino, A. Maccari, L. Mercatelli, and E. Sani (2019). "Round Robin Test for the comparison of spectral emittance measurement apparatuses". *Solar Energy Materials and Solar Cells* 191, pp. 476 –485. DOI: 10.1016/j.solmat.2018.11.026.

Le Flem, M., J. M. Gentzbittel, and P. Wident (2013). "Assessment of a European V–4Cr–4Ti alloy–CEA-J57". *Journal of Nuclear Materials* 442, S325–S329. DOI: 0.1016/j.jnucmat.2013.02.072.

Lee, G. W., S. Jeon, S.-N. Park, Y. S. Yoo, and C.-W. Park (2011). "Temperature and thickness dependence of IR optical properties of sapphire at moderate temperature". *International Journal of Thermophysics* 32, pp. 1448–1456. DOI: 10.1007/s10765-011-0990-2.

Levinson, R., P. Berdahl, and H. Akbari (2005). "Solar spectral optical properties of pigments-Part II: survey of common colorants". *Solar Energy Materials and Solar Cells* 89, pp. 351–389. DOI: 10.1016/j.solmat.2004.11.013.

Li, Y., X. L. Xia, C. Sun, Q. Ai, B. Liu, and H. P. Tan (2018). "Tomography-based analysis of apparent directional spectral emissivity of high-porosity nickel foams". *International Journal of Heat and Mass Transfer* 118, pp. 402–415. DOI: 10.1016/j.ijheatmasstransfer.2017.11.005.

Lopes, R., L. M. Moura, D. Baillis, and J. F. Sacadura (2000). "Directional spectral emittance of a packed bed: correlation between theoretical prediction and experimental data". *Journal of Heat Transfer* 123, pp. 240–248. DOI: 10.1115/1.1338134.

Lott, F., A. Netchaieff, F. Escourbiac, J. L. Jouvelot, S. Constans, and D. Hernandez (2010). "Advances in optical thermometry for the ITER divertor". *Fusion Engineering and Design* 85, pp. 146–152. DOI: 10.1016/j.fusengdes.2009.08.007.

Makino, T., H. Kawasaki, and T. Kunitomo (1982). "Study of the radiative properties of heat resisting metals and alloys: (1st report, optical constants and emissivities of nickel, cobalt and chromium)". *Bulletin of JSME* 25, pp. 804–811. DOI: 10.1299/jsme1958.25.804.

Makino, T., R. Kishida, H. Kawasaki, and T. Kunitomo (1980). "Optical constants and emissivities of iron and steel in the ferrite and austenite phases at high temperatures". *Bulletin of JSME* 23, pp. 1835–1841. DOI: 10.1299/jsme1958.23.1835.

Makino, T. and T. Kunitomo (1977). "Dispersions of optical constants and emissivities of iron and steel in the temperature range up to the Curie point". *Bulletin of JSME* 20, pp. 1607–1614. DOI: 10.1299/jsme1958.20.1607.

Mangano, A. and G. Coggiola (1993). "Stability of K-, N- and S-type thermocouples in the temperature range from 0 °C to 1060 °C". *Measurement* 12, pp. 171 –182. DOI: 10.1016/0263-2241(93)90024-C.

Matsumoto, M. and T. Nishimura (1998). "Mersenne Twister: a 623-dimensionally equidistributed uniform pseudo-random number generator". *ACM Transactions on Modeling and Computer Simulation* 8, pp. 3–30. DOI: 10.1145/272991.272995.

Mehos, M., C. Turchi, J. Vidal, M. Wagner, Z. Ma, C. K. Ho, W. Kolb, C. Andraka, and A. Kruizenga (2017). *Concentrating solar power Gen3 demonstration roadmap*. Tech. rep. NREL/TP-5500-67464. National Renewable Energy Lab. URL: https://www.nrel.gov/docs/fy17osti/67464.pdf.

Mercatelli, L., M. Meucci, and E. Sani (2015). "Facility for assessing spectral normal emittance of solid materials at high temperature". *Applied Optics* 54, pp. 8700–8705. DOI: 10.1364/AO.54.008700.

Modest, M. F. (2013). *Radiative Heat Transfer*. 3rd ed. Oxford: Academic Press.

Monchau, J. P., J. Hameury, P. Ausset, B. Hay, L. Ibos, and Y. Candau (2018). "Comparative study of radiometric and calorimetric methods for total hemispherical emissivity measurements". *Heat and Mass Transfer* 54, pp. 1415–1425. DOI: 10.1007/s00231-017-2238-6.

Monte, C. and J. Hollandt (2010). "The determination of the uncertainties of spectral emissivity measurements in air at the PTB". *Metrologia* 47, S172–S181. DOI: 10.1088/0026-1394/47/2/s14.

Moon, J., T. K. Kim, B. VanSaders, C. Choi, Z. Liu, S. Jin, and R. Chen (2015). "Black oxide nanoparticles as durable solar absorbing material for high-temperature concentrating solar power system". *Solar Energy Materials and Solar Cells* 134, pp. 417–424. DOI: 10.1016/j.solmat.2014.12.004.

Moon, J., D. Lu, B. VanSaders, T. K. Kim, S. D. Kong, S. Jin, R. Chen, and Z. Liu (2014). "High performance multi-scaled nanostructured spectrally selective coating for concentrating solar power". *Nano Energy* 8, pp. 238–246. DOI: 10.1016/j.nanoen.2014.06.016.

Mulford, R. B., N. S. Collins, M. S. Farnsworth, M. R. Jones, and B. D. Iverson (2018). "Total hemispherical apparent radiative properties of the infinite V-groove with specular reflection". *International Journal of Heat and Mass Transfer* 124, pp. 168–176. DOI: 10.1016/j.ijheatmasstransfer.2018.03.041.

Muroga, T. (2012). "Vanadium for Nuclear Systems". *Comprehensive Nuclear Materials*. Ed. by R. Konings. Amsterdam: Elsevier, pp. 391 –406. DOI: 10.1016/B978-0-08-056033-5.00094-X.

Muroga, T. (2017). "Refractory metals as core materials for Generation IV nuclear reactors". *Structural Materials for Generation IV Nuclear Reactors*. Ed.

by P. Yvon. Cambridge: Woodhead Publishing, pp. 415–440. DOI: 10.1016/B978-0-08-100906-2.00011-2.

Muroga, T., J. M. Chen, V. M. Chernov, R. J. Kurtz, and M. Le Flem (2014). "Present status of vanadium alloys for fusion applications". *Journal of Nuclear Materials* 455, pp. 263–268. DOI: 10.1016/j.jnucmat.2014.06.025.

Nakar, D. and D. Feuermann (2016). "Surface roughness impact on the heat loss of solar vacuum heat collector elements (HCE)". *Renewable Energy* 96, pp. 148–156. DOI: 10.1016/j.renene.2016.04.041.

Nakos, J. T. (2004). *Uncertainty analysis of thermocouple measurements used in normal and abnormal thermal environment experiments at Sandia's Radiant Heat Facility and Lurance Canyon Burn Site*. Tech. rep. SAND2004-1023. Sandia National Laboratories. URL: http://prod.sandia.gov/techlib/access-control.cgi/2004/041023.pdf.

Nam, K., W. Chung, C. H. Noh, D. Kang, K. O. Kang, H. J. Ahn, H. G. Lee, C. Hamlyn-Harris, N. Her, C. H. Choi, and C. Sborchia (2014). "Thermal analysis on detailed 3D models of ITER thermal shield". *Fusion Engineering and Design* 89, pp. 1843–1847. DOI: 10.1016/j.fusengdes.2014.02.060.

Natesan, K. and M. Uz (2000). "Oxidation performance of V-Cr-Ti alloys". *Fusion Engineering and Design* 51, pp. 145–152. DOI: 10.1016/S0920-3796(00)00308-2.

Novikov, I. I. (1958). "The efficiency of atomic power stations (a review)". *Journal of Nuclear Energy (1954)* 7, pp. 125–128. DOI: 10.1016/0891-3919(58)90244-4.

Ongena, J. and G. Van Oost (2012). "Energy for future centuries: prospects for fusion power as a future energy source". *Fusion Science and Technology* 61, pp. 3–16. DOI: 10.13182/FST12-A13488.

Ordal, M. A., R. J. Bell, R. W. Alexander, L. L. Long, and M. R. Querry (1985). "Optical properties of fourteen metals in the infrared and far infrared: Al, Co, Cu, Au, Fe, Pb, Mo, Ni, Pd, Pt, Ag, Ti, V, and W." *Applied Optics* 24, pp. 4493–4499. DOI: 10.1364/AO.24.004493.

Paradis, P. F., T. Ishikawa, T. Aoyama, and S. Yoda (2002). "Thermophysical properties of vanadium at high temperature measured with an electrostatic levitation furnace". *The Journal of Chemical Thermodynamics* 34, pp. 1929–1942. DOI: 10.1016/S0021-9614(02)00126-X.

Pavese, F. (2009). "About the treatment of systematic effects in metrology". *Measurement* 42, pp. 1459 –1462. DOI: 10.1016/j.measurement.2009.07.017.

Pedrotti, F. L. and L. S. Pedrotti (1993). *Introduction to Optics*. 2nd ed. Englewood Cliffs: Prentice-Hall.

Pelay, U., L. Luo, Y. Fan, D. Stitou, and M. Rood (2017). "Thermal energy storage systems for concentrated solar power plants". *Renewable and Sustainable Energy Reviews* 79, pp. 82–100. DOI: 10.1016/j.rser.2017.03.139.

Pérez-Sáez, R. B., L. del Campo, and M. J. Tello (2008). "Analysis of the accuracy of methods for the direct measurement of emissivity". *International Journal of Thermophysics* 29, pp. 1141–1155. DOI: 10.1007/s10765-008-0402-4.

Petric, A. and H. Ling (2007). "Electrical conductivity and thermal expansion of spinels at elevated temperatures". *Journal of the American Ceramic Society* 90, pp. 1515–1520. DOI: 10.1111/j.1551-2916.2007.01522.x.

Pottlacher, G., T. Hüpf, B. Wilthan, and C. Cagran (2007). "Thermophysical data of liquid vanadium". *Thermochimica Acta* 461, pp. 88–95. DOI: 10.1016/j.tca.2006.12.010.

Raffray, A. R., M. Akiba, V. Chuyanov, L. Giancarli, and S. Malang (2002). "Breeding blanket concepts for fusion and materials requirements". *Journal of Nuclear Materials* 307, pp. 21–30. DOI: 10.1016/S0022-3115(02)01174-1.

Rebouta, L., P. Capela, M. Andritschky, A. Matilainen, P. Santilli, K. Pischow, and E. Alves (2012). "Characterization of TiAlSiN/TiAlSiON/SiO_2 optical stack designed by modelling calculations for solar selective applications". *Solar Energy Materials and Solar Cells* 105, pp. 202–207. DOI: 10.1016/j.solmat.2012.06.011.

Reddy, I. N., V. R. Reddy, N. Sridhara, V. S. Rao, M. Bhattacharya, P. Bandyopadhyay, S. Basavaraja, A. K. Mukhopadhyay, A. K. Sharma, and A. Dey (2014). "Pulsed rf magnetron sputtered alumina thin films". *Ceramics International* 40, pp. 9571–9582. DOI: 10.1016/j.ceramint.2014.02.032.

Redgrove, J. and M. Battuello (1995). "An intercomparison of normal spectral emissivity measurements between NPL (UK) and IMGC (Italy)". *High Temperatures-High Pressures* 27-28, pp. 135–146. DOI: 10.1068/htrt72.

Rogalski, A. (2012). "History of infrared detectors". *Opto-Electronics Review* 20, pp. 279–308. DOI: 10.2478/s11772-012-0037-7.

Roger, C. R., S. H. Yen, and K. G. Ramanathan (1979). "Temperature variation of total hemispherical emissivity of stainless steel AISI 304". *Journal of the Optical Society of America* 69, pp. 1384–1390. DOI: 10.1364/JOSA.69.001384.

Romanelli, F., P. Barabaschi, D. Borba, G. Federici, L. Horton, R. Neu, D. Stork, and H. Zohm (2012). *Fusion electricity: a roadmap to the realization of fusion energy*. Tech. rep. Fusion Electricity - EFDA. European Fusion Development Agreement. URL: https://art.torvergata.it/retrieve/handle/2108/132174/272198/JG12.356-web.pdf.

Rousseau, B., J. F. Brun, D. De Sousa Meneses, and P. Echegut (2005). "Temperature measurement: Christiansen wavelength and blackbody reference". *International Journal of Thermophysics* 26, pp. 1277–1286. DOI: 10.1007/s10765-005-6726-4.

Rousseau, B., S. Guevelou, A. Mekeze-Monthe, J. Vicente, L. del Campo, D. De Sousa Meneses, P. Echegut, C. Caliot, and G. Flamant (2016). "Tuning the spectral emittance of α-SiC open-cell foams up to 1300 K with their macro porosity". *AIP Advances* 6, p. 065226. DOI: 10.1063/1.4955142.

Rubin, E. B., Y. Chen, and R. Chen (2019). "Optical properties and thermal stability of Cu spinel oxide nanoparticle solar absorber coatings". *Solar Energy Materials and Solar Cells* 195, pp. 81–88. DOI: 10.1016/j.solmat.2019.02.032.

Rudtsch, S., H. P. Ebert, F. Hemberger, G. Barth, R. Brandt, U. Groß, W. Hohenauer, K. Jaenicke-Roessler, E. Kaschnitz, E. Pfaff, W. Pößnecker, G. Pottlacher, M. Rhode, and B. Wilthan (2005). "Intercomparison of thermophysical property measurements on an austenitic stainless steel". *International Journal of Thermophysics* 26, pp. 855–867. DOI: 10.1007/s10765-005-5582-6.

Ruset, C., D. Falie, E. Grigore, M. Gherendi, V. Zoita, K. D. Zastrow, G. Matthews, X. Courtois, J. Bucalossi, J. Likonen, and JET contributors (2017). "The emissivity of W coatings deposited on carbon materials for fusion applications". *Fusion Engineering and Design* 114, pp. 192–195. DOI: 10.1016/j.fusengdes.2016.12.015.

Sacadura, J. F. (2011). "Thermal radiative properties of complex media: theoretical prediction versus experimental identification". *Heat Transfer Engineering* 32, pp. 754–770. DOI: 10.1080/01457632.2011.525140.

Sakr, E. and P. Bermel (2017). "Thermophotovoltaics with spectral and angular selective doped-oxide thermal emitters". *Optics Express* 25, A880–A895. DOI: 10.1364/OE.25.00A880.

Sani, E., E. Landi, D. Sciti, and V. Medri (2016). "Optical properties of ZrB_2 porous architectures". *Solar Energy Materials and Solar Cells* 144, pp. 608–615. DOI: 10.1016/j.solmat.2015.09.068.

Schubert, M., T. E. Tiwald, and C. M. Herzinger (2000). "Infrared dielectric anisotropy and phonon modes of sapphire". *Physical Review B* 61, p. 8187. DOI: 10.1103/PhysRevB.61.8187.

Seban, R. A. (1965). "The emissivity of transition metals in the infrared". *Journal of Heat Transfer* 87, pp. 173–176. DOI: 10.1115/1.3689067.

Seki, Y., K. Ezato, S. Suzuki, K. Yokoyama, M. Enoeda, and S. Mori (2010). "Non-destructive examination with infrared thermography system for ITER divertor components". *Fusion Engineering and Design* 85, pp. 1451–1454. DOI: 10.1016/j.fusengdes.2010.04.010.

Selvakumar, N. and H. C. Barshilia (2012). "Review of physical vapor deposited (PVD) spectrally selective coatings for mid-and high-temperature solar thermal applications". *Solar Energy Materials and Solar Cells* 98. DOI: 10.1016/j.solmat.2011.10.028.

Setién-Fernández, I., T. Echániz, L. González-Fernández, R. B. Pérez-Sáez, E. Céspedes, J. A. Sánchez-García, L. Álvarez-Fraga, R. Escobar Galindo, J. M. Albella, C. Prieto, and M. J. Tello (2013). "First spectral emissivity study of a solar selective coating in the 150-600 °C temperature range". *Solar Energy Materials and Solar Cells* 117, pp. 390–395. DOI: 10.1016/j.solmat.2013.07.002.

Shaw, J. A. (2002). "The effect of instrument polarization sensitivity on sea surface remote sensing with infrared spectroradiometers". *Journal of Atmospheric and Oceanic Technology* 19, pp. 820–827. DOI: 10.1175/1520-0426(2002)019<0820:TEOIPS>2.0.CO;2.

Shen, Y., D. Ye, I. Celanovic, S. G. Johnson, J. D. Joannopoulos, and M. Soljačić (2014). "Optical broadband angular selectivity". *Science* 343, pp. 1499–1501. DOI: 10.1126/science.1249799.

Sibin, K., S. John, and H. C. Barshilia (2015). "Control of thermal emittance of stainless steel using sputtered tungsten thin films for solar thermal power applications". *Solar Energy Materials and Solar Cells* 133, pp. 1–7. DOI: 10.1016/j.solmat.2014.11.002.

Sievers, A. (1978). "Thermal radiation from metal surfaces". *Journal of the Optical Society of America* 68, pp. 1505–1516. DOI: 10.1364/JOSA.68.001505.

Smith, D. L., H. M. Chung, B. A. Loomis, H. Matsui, S. Votinov, and W. Van Witzenburg (1995). "Development of vanadium-base alloys for fusion first-wall - blanket applications". *Fusion Engineering and Design* 29, pp. 399–410. DOI: 10.1016/0920-3796(95)80046-Z.

SolarPACES. *Concentrating Solar Power Projects*. Accessed on March 18, 2020. URL: https://solarpaces.nrel.gov.

Soum-Glaude, A., A. Le Gal, M. Bichotte, C. Escape, and L. Dubost (2017). "Optical characterization of $TiAlN_x/TiAlN_y/Al_2O_3$ tandem solar selective absorber coatings". *Solar Energy Materials and Solar Cells* 170, pp. 254–262. DOI: 10.1016/j.solmat.2017.06.007.

Stagg, B. J. and T. T. Charalampopoulos (1991). "Surface-roughness effects on the determination of optical properties of materials by the reflection method". *Applied Optics* 30, pp. 4113–4118. DOI: 10.1364/AO.30.004113.

Stanimirović, A., G. Vuković, and K. Maglić (1999). "Thermophysical and thermal optical properties of vanadium by millisecond calorimetry between 300 and 1900 K". *International Journal of Thermophysics* 20, pp. 325–332. DOI: 10.1023/A:1021471423350.

Stroud, D. (1998). "The effective medium approximations: Some recent developments". *Superlattices and Microstructures* 23, pp. 567–573. DOI: 10.1006/spmi.1997.0524.

Suo-Anttila, J. M., J. T. Nakos, and W. Gill (2004). *Shroud boundary condition characterization experiments at the Radiant Heat Facility*. Tech. rep. SAND2004-5080. Sandia National Laboratories. URL: https://prod-ng.sandia.gov/techlib-noauth/access-control.cgi/2004/045080.pdf.

Ta, M. T., J. Y. Rolland, P. Echegut, B. Rousseau, M. Zaghrioui, F. Giovannelli, H. Gomart, P. Lenormand, and F. Ansart (2010). "Prediction of thermal radiative properties (300-1000 K) of $La_2NiO_{4+\delta}$ ceramics". *Applied Physics Letters* 97, p. 181917. DOI: 10.1063/1.3511344.

Teodorescu, G. (2007). "Radiative emissivity of metals and oxidized metals at high temperature". PhD thesis. Auburn University.

Ter Haar, D. (1967). *The old quantum theory*. Oxford: Pergamon Press.

Trasferetti, B. C., F. P. Rouxinol, R. V. Gelamo, M. A. Bica de Moraes, C. U. Davanzo, and D. L. de Faria (2004). "Berreman effect in amorphous and crystalline WO_3 thin films". *The Journal of Physical Chemistry B* 108, pp. 12333–12338. DOI: 10.1021/jp036653u.

Wang, H., V. P. Sivan, A. Mitchell, G. Rosengarten, P. Phelan, and L. Wang (2015). "Highly efficient selective metamaterial absorber for high-temperature solar thermal energy harvesting". *Solar Energy Materials and Solar Cells* 137, pp. 235–242. DOI: 10.1016/j.solmat.2015.02.019.

Weinstein, L., D. Kraemer, K. McEnaney, and G. Chen (2014). "Optical cavity for improved performance of solar receivers in solar-thermal systems". *Solar Energy* 108, pp. 69–79. DOI: 10.1016/j.solener.2014.06.023.

Weinstein, L. A., J. Loomis, B. Bhatia, D. M. Bierman, E. N. Wang, and G. Chen (2015). "Concentrating Solar Power". *Chemical Reviews* 115, pp. 12797–12838. DOI: 10.1021/acs.chemrev.5b00397.

Wen, C. D. and I. Mudawar (2006). "Modeling the effects of surface roughness on the emissivity of aluminum alloys". *International Journal of Heat and Mass Transfer* 49, pp. 4279–4289. DOI: 10.1016/j.ijheatmasstransfer.2006.04.037.

Woods, S. I., T. M. Jung, D. R. Sears, and J. Yu (2014). "Emissivity of silver and stainless steel from 80 K to 300 K: Application to ITER thermal shields". *Cryogenics* 60, pp. 44 –48. DOI: 10.1016/j.cryogenics.2014.01.002.

Wynne, B. P., M. J. Gorley, P. F. Zheng, A. J. Cackett, M. Porton, and E. Surrey (2016). "An analysis of the microstructure of spark plasma sintered and hot isostatically pressed V-4Cr-4Ti-1.8Y-0.4Ti_3SiC_2 alloy and its thermal stability". *Journal of Alloys and Compounds* 680, pp. 506–511. DOI: 10.1016/j.jallcom.2016.04.159.

Xu, K., M. Du, L. Hao, J. Mi, Q. Yu, and S. Li (2019). "A review of high-temperature selective absorbing coatings for solar thermal applications". *Journal of Materiomics* 6, pp. 167–182. DOI: 10.1016/j.jmat.2019.12.012.

Yang, Y. and R. O. Buckius (1995). "Surface length scale contributions to the directional and hemispherical emissivity and reflectivity". *Journal of Thermophysics and Heat Transfer* 9, pp. 653–659. DOI: 10.2514/3.720.

Zhang, K., K. Yu, Y. Liu, and Y. Zhao (2017). "An improved algorithm for spectral emissivity measurements at low temperatures based on the multi-temperature calibration method". *International Journal of Heat and Mass Transfer* 114, pp. 1037 –1044. DOI: 10.1016/j.ijheatmasstransfer.2017.06.133.

Zhang, K., Y. Zhao, K. Yu, and Y. Liu (2018a). "Development of experimental apparatus for precise emissivity determination based on the improved method compensating disturbances by background radiation". *Infrared*

Physics & Technology 92, pp. 350 –357. DOI: 10.1016/j.infrared.2018.06.031.

Zhang, Y., Y. Zhang, R. Lu, S. Shu, X. Lang, and L. Yang (2018b). "Investigation of the normal spectral band emissivity characteristic within 7.5 to 13 μm for Molybdenum between 100 and 500 °C". *Infrared Physics & Technology* 88, pp. 74–80. DOI: 10.1016/j.infrared.2017.11.017.

Zheng, P. F., T. Nagasaka, T. Muroga, and J. M. Chen (2014). "Microstructures and mechanical properties of mechanically alloyed V–4Cr–4Ti alloy dispersion strengthened by nano-particles". *Fusion Engineering and Design* 89, pp. 1648–1652. DOI: 10.1016/j.fusengdes.2014.03.020.

Zinkle, S. J., H. Matsui, D. L. Smith, A. F. Rowcliffe, E. Van Osch, K. Abe, and V. A. Kazakov (1998). "Research and development on vanadium alloys for fusion applications". *Journal of Nuclear Materials* 258, pp. 205–214. DOI: 10.1016/S0022-3115(98)00269-4.